How oscillations persist through chains of excitable cells and in large noise-driven excitable systems

by

Derek Orr

B.S. Mathematics, University of Pittsburgh, 2016

B.S. Physics, University of Pittsburgh, 2016

M.S. Mathematics, University of Pittsburgh, 2019

Submitted to the Graduate Faculty of

the Dietrich School of Arts and Sciences in partial fulfillment

of the requirements for the degree of

Doctor of Philosophy

University of Pittsburgh

2021

UNIVERSITY OF PITTSBURGH

DIETRICH SCHOOL OF ARTS AND SCIENCES

This dissertation was presented

by

Derek Orr

It was defended on

March 16, 2021

and approved by

Dr. Bard Ermentrout, Mathematics, University of Pittsburgh

Dr. Jonathan Rubin, Mathematics, University of Pittsburgh

Dr. David Swigon, Mathematics, University of Pittsburgh

Dr. Hanna Salman, Physics, University of Pittsburgh

How oscillations persist through chains of excitable cells and in large noise-driven excitable systems

Derek Orr, PhD

University of Pittsburgh, 2021

Our goal is to understand how excitable cells and oscillatory cells interact with each other and, ultimately, decide if excitable cells can generate macroscopic oscillations that persist in these networks. We begin by studying a one-dimensional chain model of this: oscillatory cells coupled indirectly with excitable cells in between. We have three main systems: OE, OEO, and OEEO. We show that with the right coupling strength, one can get the two oscillators on the ends to synchronize (or not synchronize) and the system exhibits m:n locking patterns.

In our second project, we remove the chain constraint and focus on just all-to-all coupled excitable cells. However, these will not create oscillations alone so we added noise to these cells so the cells can oscillate randomly in the network. We perform mean-field theory (MFT) methods on this system and chose Gaussian white noise as well as different heterogeneous noise distributions. We find that macroscopic oscillations can occur as long as one has the right set of parameters, the right noise distribution, and/or the right coupling function.

In the final project, we combine the first two projects: we take the noisy excitable cells, which we know can create oscillations, and we couple each cell to a single oscillator. When the noise level is zero, this is equivalent to one oscillator and one excitable cell coupled to each other (our OE model from the first project). Hence, we find m:n locking patterns again. This last project investigates how large the noise level can become before the m:n locking patterns become unstable. We notice that using heterogeneous noise allows for the noise threshold to be larger than when using Gaussian noise.

Table of contents

List of tables

List of figures

Preface

I did not get here alone. First, I would like to thank my PhD advisor, Dr. Bard Ermentrout, for getting me started with research early on in my career. I am fortunate to have known him since 2014 when I had him for undergraduate differential equations. I e-mailed him in my first semester of my senior year, asking if he was interested in doing any research and I completely forgot about it. Then, in January, I received an e-mail from him asking if I still wanted to do some research and I happily agreed. Since then, he and I have connected on a lot but mainly our love of dogs and specifically corgis. I would also like to thank my committee members: Dr. Jon Rubin, who I have known since 2013 at the Integration Bee (and in 2016 I'll never forget that I forgot one of the boundary terms in $\int \ln^2(x)\, dx$ and Jon kept telling me I was wrong and I couldn't figure out why), Dr. David Swigon, who has helped me countlessly through the preliminary exams and coached me through studying for my comprehensive exams, and Dr. Hanna Salman, who was my professor for the honors undergraduate physics laboratory course. I was excited when I found out he knew Bard and had even written papers with him.

I would also like to thank my fianceé and soon-to-be wife, Sarah Klos. Sarah, you have helped me through so much, I can't even begin to describe the support you've given me. From preliminary exams to comprehensive exams to applying for jobs to wedding planning, thank you for everything.

There are so many others I would like to thank for getting me through my PhD career. To the many friends, colleagues, family members and future family members who have helped me get where I am today, thank you.

1.0 Introduction

We will focus on two types of cells, excitable cells and oscillatory cells or oscillators. Cells, for our purpose, transfer voltage to other cells to which it is connected. This is referred to as *firing*. Coupled oscillators synchronizing, meaning they transfer voltage simultaneously to each other, is an important and much studied phenomenon. In many analyses of coupled oscillators, each element is a limit cycle oscillator and techniques such as weak coupling are applied to study them. However, many systems, such as neurons, have conditional oscillators; that is, they transfer voltage only when given enough drive.

For an excitable cell, imagine the strength game at your local carnival. Someone is stepping up, grabs the hammer and hits the base of the strength-o-meter. Nothing happens. This person does not give enough of an input to cause the bell at the top to ring. Someone else, perhaps a lot stronger, is up next and they whack the hammer on the base and that input causes the bell to ring. This input was large enough to cause an *output* to occur, the ringing of the bell. Of course, this analogy is not perfect; we must imagine that it takes a long time for the metal ball to return back to the bottom of the strength-o-meter. So, if someone else comes and hits the base with the hammer while the ball is still coming down, nothing will happen no matter how strong they are. This entire process is very similar to an excitable cell firing. In more mathematical terms, the excitable cell has a unique globally attracting equilibrium point (the base of the strength-o-meter), but with a sufficiently large perturbation, it can fire once (bell ringing) before returning to the stable equilibrium. If the excitable cell keeps receiving input, the cell could fire rhythmically (bell rings every few seconds). The dynamics of oscillators coupled indirectly via excitable systems remains an open problem. For example, in the early stages of aggregation of cellular slime molds, each cell is excitable, but some of the cells become oscillatory and the result is an oscillatory system that induces the organism to ultimately organize into a slug (see [1]). Within the smooth muscle of the intestine are a small number of spontaneously active cells (interstitial cells of Cajal) that are coupled and organized to form waves through the intervening non-oscillatory cells (see [2, 3]). Interactions between oscillatory and non-oscillatory glial cells

are thought to underlie synchronization for circadian rhythms (see [4]).

This problem has been studied in the context of all-to-all coupling where each element is connected to all the other elements. For example, in [5] they couple two populations of Stuart-Landau equations where one of the populations has a stable equilibrium and the other is oscillatory and analyze the ensemble dynamics as the relative numbers of active and inactive elements varies. Similarly, in [6] the authors analyze sinusoidally coupled mixtures of oscillators and excitable cells where each cell is represented as a scalar phase model. Like [7], they study the onset of collective synchrony as the ratio of oscillators changes. Others have used the so-called Ott-Antonsen reduction to study collective dynamics of mixtures of oscillatory and excitable elements (see [8, 9, 10]).

The previous work on this problem relies on the fact that all elements are globally coupled to each other. On the other hand, the biological examples we have described are much more locally coupled; this is the scenario that we focus on in the beginning of this dissertation. Synchrony between two neurons coupled via passive dendrites has been studied in [11]. Others have broadened this to include "quasi-active" dendrites, though it is still a linear theory (see [12, 13]). As an initial attempt to understand interactions between oscillators and excitable systems, we are interested in describing the dynamics between two oscillatory cells distributed in a simple chain with intervening excitable cells between them. We will use a one-dimensional model for both the excitable and the oscillatory cells and then show that similar phenomena hold in more realistic neural models.

There are two broad types of excitability [14]: Class II which occurs for a system near a sub-critical Hopf bifurcation and Class I, which occurs when there is a saddle-node infinite cycle (SNIC) bifurcation. The latter type of excitability lends itself to simple one-dimensional dynamics on a circle [15, 16], thus this will be the type of excitability we will consider in this dissertation. The simplest version of this excitability takes the form

$$\frac{dy}{dt} = 1 - b\cos(y) =: f(y) \tag{1}$$

where $b \geq 0$ is a parameter and $y \in [0, 2\pi)$ lies on the circle. When $b > 1$, then (1) has two equilibria $y^{\pm} = \pm \arccos(1/b)$, with y^- ("rest state") asymptotically stable and y^+ ("threshold") unstable. Any initial data $y(0) > y^+$ will traverse the circle before returning to

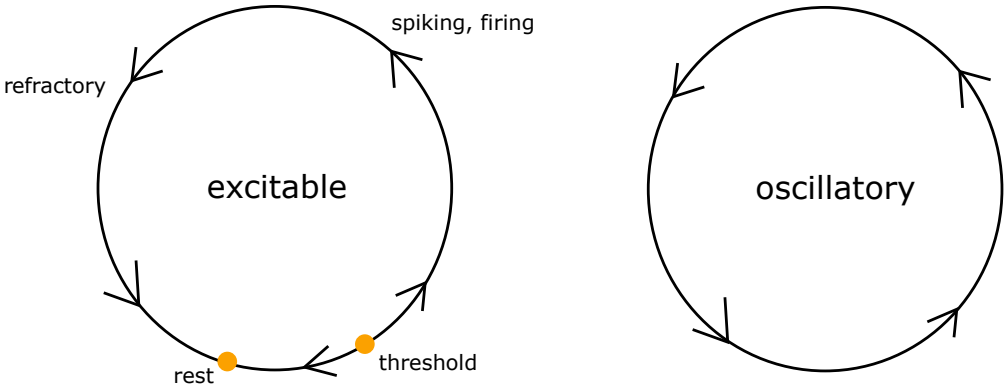

Figure 1: Schematic of an oscillator and an excitable cell. The excitable cell has a threshold value that must be crossed in order for the cell to fire, whereas the oscillatory cell does not.

rest (the cell will fire). As b decreases to $b_{SN} = 1$, the two roots merge and then for $b < 1$, $dy/dt > 0$ always and it acts like an oscillator with varying frequency. Henceforth, we will model the excitable cells by (1) with $b > 1$. Oscillators are modeled as the simple phase dynamics,

$$\frac{dx}{dt} = \omega$$

where $\omega > 0$ is a natural constant frequency. As with the excitable system, $x \in [0, 2\pi)$ and lies on the circle. See Figure 1 for a schematic diagram. These cells will have coupling strengths between them and therefore, it is important to highlight our main model in the first project, which is two excitable cells linking two oscillatory cells together. Figure 2 shows the diagram of the coupling between them. This figure will give an idea as to what c_{ee}, c_{eo}, and c_{oe} mean throughout the rest of the chapters. Our goal for the first project is to understand the dynamics of these systems and look at m:n locking regions, where the excitable cell will fire m times for every n times the oscillator fires.

We can also achieve oscillations with noise-driven excitable cells. Sakaguchi [25] was among the first to observe that noise plus coupling can induce oscillations in excitable systems where they performed a bifurcation analysis of a Fourier mode expansion of the associated Fokker-Planck equation. Neiman and collaborators have further analyzed the underlying dynamics of this behavior [26, 28, 32, 33] while separation of time scales has also been a

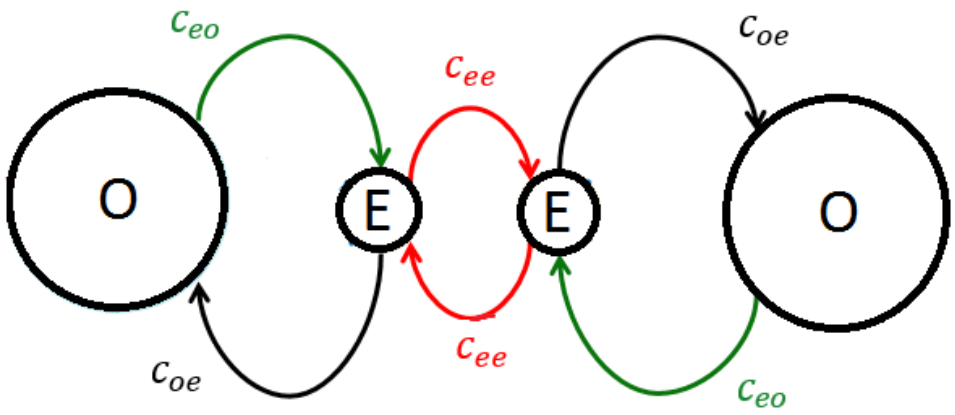

Figure 2: Schematic of our main model in the first project: the OEEO system. The parameters c_{ee}, c_{eo}, and c_{oe} represent the coupling strengths shown in the figure.

fruitful approach to this phenomena [29, 31, 34, 35]. Later, we will use a mean-field theory (MFT) approach to study the effects of heterogeneity in the excitability as well as Gaussian noise on the emergence of macroscopic oscillations. This approach analyzes the average response over a globally coupled system rather than each individual oscillator and greatly reduces the dimensionality, making it attractive for analysis. MFT has a wide variety of applications to the dynamics of large globally coupled biological and physical systems (see [25, 33, 35, 36, 37]). We use the technique developed by Ott and Antonsen [38] which further simplifies the mean-field continuity equations. Their approach has been dubbed the "Ott-Antonsen ansatz" and it is a very important tool for studying phase oscillations (see [39, 8, 40, 41]). Our last project extends this one and involves coupling one oscillator to the system of noisy excitable cells and investigating the m:n locking regimes again and how they change with the noise level of the excitable cells. We conclude this introductory chapter with an in-depth outline of this dissertation.

In this dissertation, our goal is to understand how excitable cells and oscillatory cells interact with each other and, ultimately, decide if excitable cells can generate oscillations that persist in these networks. We begin by studying a simple oscillatory cell coupled to a

simple excitable cell, as stated before, with sinusoidal coupling using a scalar phase model for each cell. We show that this excitable cell indeed oscillates when connected to the oscillatory cell and the system exhibits m:n locking patterns depending on the coupling strength. Later, we move on to two oscillators coupled to the excitable cell but not to each other and after, we have two excitable cells in between the two oscillatory cells like a chain: OEEO. The results suggest that with the right amount of coupling strength between these cells, the two oscillators can be synchronous with each other. We also look into the heterogeneity of the oscillator frequencies as well as some weak coupling analysis. At the end, we look towards an infinite chain of excitable cells with an oscillator on each end and we relate our OEEO system with a Morris-Lecar model.

In our second project, we want to find out if excitable cells can create oscillations without oscillatory cells being connected to them. Of course, this cannot happen with purely excitable cells so we consider noisy excitable cells: cells that are, on average, excitable but they can become oscillatory randomly due to the noise driving them. Instead of a chain, we give them all-to-all coupling and we have an arbitrarily large number N of excitable cells. This allows us to perform mean-field theory (MFT) on this system which will help us study this system as N tends to infinity. We begin with standard Gaussian white noise, dependent on time. Using the nonlinear Fokker-Planck equation, one can form a system of infinitely many ODEs, which we truncate to 20 modes. After analyzing this system, one can see that these noisy excitable cells can indeed generate macroscopic oscillations. Later, we take heterogeneous noise and find that if the noise distribution is the Cauchy distribution and we have purely sinusoidal coupling as before, then the excitable cells cannot form macroscopic oscillations regardless of the noise level. We also take some noise densities which decay faster than the Cauchy distribution and find that these do produce macroscopic oscillations, similar to the Gaussian white noise case. Going back to the Cauchy distribution, we can add a cosine term to the coupling and doing this creates the macroscopic oscillations that we could not find when we had pure sinusoidal coupling. Lastly in this chapter, we noticed that the bifurcation diagrams all seem to have a cusp bifurcation and a Takens-Bogdanov bifurcation approach each other as the noise level goes to 0. So we perform a rescaling analysis and prove that these two bifurcations do not meet.

In the final project, we combine the first two projects: we take the noisy excitable cells, which we know can create oscillations, and we couple each cell to a single oscillator. When the noise level is zero, this is similar to just one oscillator and one excitable cell coupled to each other, which is where we began. So, with the noise level being zero, this will give the m:n locking regimes that we found in the first project. This last project investigates how large the noise level can become before the m:n locking patterns become unstable. We found that using heterogeneous noise allows for the noise threshold to be larger than when using Gaussian noise.

2.0 Chains of excitable cells

2.1 Introduction

We begin with the general form of our excitable cell chain with oscillators on either end:

$$\begin{aligned}
\frac{dx}{dt} &= \omega + d + c_{oe}\sin(y_1 - x) \\
\frac{dy_1}{dt} &= f(y_1) + c_{eo}\sin(x - y_1) + c_{ee}\sin(y_2 - y_1) \\
\frac{dy_j}{dt} &= f(y_j) + c_{ee}[\sin(y_{j-1} - y_j) + \sin(y_{j+1} - y_j)] \\
\frac{dy_N}{dt} &= f(y_N) + c_{eo}\sin(z - y_N) + c_{ee}\sin(y_{N-1} - y_N) \\
\frac{dz}{dt} &= \omega - d + c_{oe}\sin(y_N - z)
\end{aligned} \tag{2}$$

where $j = 2, \ldots, N-1$ and $f(y)$ is given in equation (1). Here x, z are oscillators (often referred to as **O cells**) with uncoupled frequencies of $\omega \pm d$ and the variables y_j are excitable (referred to as **E cells**) with $b > 1$. The coupling strength between cells are positive, that is c_{eo}, c_{oe}, $c_{ee} > 0$. We allow for some heterogeneity in the oscillators via the parameter d, also positive. While this may seem as a somewhat restricted parameterization for a model, we note the normal form for a SNIC bifurcation is

$$\frac{dx}{dt} = 1 - \cos(x) + \big(1 + \cos(x)\big)p = (1+p)\Big(1 - \frac{1-p}{1+p}\cos(x)\Big)$$

which, after rescaling time, is identical to our model dynamics. For the biophysical simulations, we use the Morris-Lecar model, where each cell obeys

$$\begin{aligned}
V' &= I - 4m_\infty(V)(V - 120) - 8w(V + 84) - 2(V + 60) + I_{coup} \\
w' &= 0.3\big(w_\infty(V) - w\big)/\tau_w(V) \\
m_\infty(V) &= \frac{1}{2}\Big(1 + \tanh\big((V + 1.2)/18\big)\Big) \\
w_\infty(V) &= \frac{1}{2}\Big(1 + \tanh\big((V - 12)/17.4\big)\Big) \\
\tau_w(V) &= \operatorname{sech}\big((V - 12)/34.8\big)
\end{aligned} \tag{3}$$

with $I = 43$ for the oscillators and $I = 39$ for the excitable cells. Coupling currents, I_{coup} have the form $g(\hat{V} - V)$ where $\hat{V}$ is the voltage of the cell to which V is coupled. The parameter g varies and is provided in the figure captions.

2.2 Results

We first explore one OE pair to see the effects of the oscillator on an excitable unit and then look at what happens with chains of excitable cells.

2.2.1 OE pair

We start with the simple system

$$\begin{aligned} \dot{x} &= \omega + c_{oe} \sin(y - x) \\ \dot{y} &= f(y) + c_{eo} \sin(x - y) \end{aligned} \tag{4}$$

where we set $b = 1.1$, $\omega = 1$ and we vary the coupling parameters c_{oe} and c_{eo}. This is a system on a two-dimensional torus and as long as $c_{oe} < 1$, there are no fixed points. Since this is a flow on a torus and $\dot{x} > 0$, we can make a Poincare section along an arbitrary value $x = C$ which will lead to a one-dimensional map. As the dynamics are in the plane, the map is monotone and invertible, thus, there is a well defined rotation number

$$\rho = \lim_{t \to \infty} \frac{y(t)}{x(t)}$$

which is a continuous function of the parameters. When c_{eo} is sufficiently small (e.g., $c_{eo} < (b - 1)$ is sufficient), then $y(t)$ will just oscillate around y^-, the stable rest state, and the rotation number is 0.

Figure 3 shows the behavior of (4) as the coupling strengths vary. If c_{eo} is small enough, then the excitable cell will never fire, while for c_{eo} large enough, it will always fire in a 1:1 manner with the oscillator. The inset in the figure shows the rotation number as a function of c_{eo} at different values of c_{oe}. Notice as c_{oe} goes to 1, the oscillator slows its frequency to 0 and x becomes nearly constant with $\sin(y - x) \approx -1$. Thus, $\dot{y} \approx f(y) + c_{eo}$ and when c_{eo}

exceeds $b-1$, $\dot{y}$ will be positive meaning the excitable cell will fire and when $c_{eo} < b-1$, the excitable cell will not fire. This explains why all the curves in the figure converge at $c_{eo} = b-1$ when $c_{oe} = 1$. At the other extreme, when $c_{oe} = 0$, the rotation number has no open sets of parameters where there are locking regimes other than 0:1 and 1:1.

We note that if $c_{oe} \geq 1$, then it is possible to find equilibria in (4). Multiplying the $\dot{y}$ equation by c_{oe} and the $\dot{x}$ equation by c_{eo} and adding them results in

$$c_{eo}\omega + c_{oe} = c_{oe} b \cos(y).$$

Thus, fixed points $\bar{y}$ exist as long as $c_{oe} > c_{eo}\omega/(b-1)$. Furthermore, we also must have that $c_{oe} \geq \omega$ so $\dot{x}$ can be zero. Thus, there is a critical value of $c_{eo} = b-1$ where there is a saddle-node bifurcation with $c_{oe} = \omega$. In general, the saddle-node bifurcation is $c_{eo} = (b-1)c_{oe}/\omega$ for $c_{oe} > \omega$. We close this section by noting that making b larger shifts the curves in Figure 3 toward higher values of c_{eo} as it takes stronger coupling to induce the excitable cell to fire. Decreasing the uncoupled frequency of the oscillator from $\omega = 1$ is similar to increasing the coupling c_{oe} as both slow the oscillator down giving the excitable system a better chance at firing.

2.2.2 OEO chain

The simplest way that two oscillators can interact via an excitable cell is given by

$$\begin{aligned} \dot{x} &= \omega + d + c_{oe}\sin(y_1 - x) \\ \dot{y_1} &= f(y_1) + c_{eo}(\sin(x - y_1) + \sin(z - y_1)) \\ \dot{z} &= \omega - d + c_{oe}\sin(y_1 - z). \end{aligned} \tag{5}$$

We set $b = 1.1, \omega = 1, d = 0$ and varied c_{oe}, c_{eo} once again to get a big picture of the dynamics. Figure 4 shows boundaries for these phase-locked solutions. For most values of the coupling parameters, the dominant behaviors are 1:1 and 0:1 where the E cell either fires on every cycle or doesn't fire at all. Within a narrow sector of parameters, we find the 1:2 phase-locking, where the E cell fires once for every two times the oscillators fire, just like the OE system. The boundaries of the OEO system are not much different from the OE system,

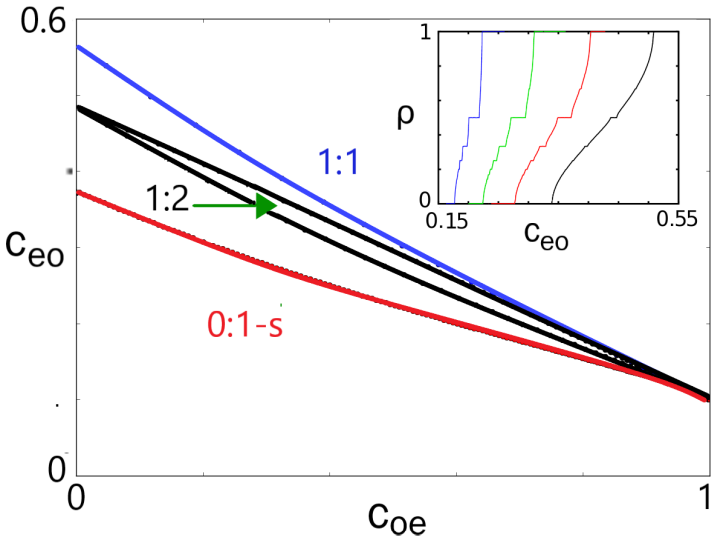

Figure 3: Dynamics of system (4) as the connectivity varies. Below the red (bottom) curve, the excitable cell does not fire and we call this 0:1-s locking. The "s" stands for "synchrony" because in later models when we have more than one oscillator, the oscillators will not always synchronize. Because there is only one oscillator in this system, it is trivially synchronized with itself. Above the blue (top) curve, the excitable cell fires in a 1:1 manner with the oscillator. In between, rational and irrational firing patterns occur; the 1:2 locking regime is illustrated in between the two black (middle) lines. In fact, all m:n lockings will occur for $m \leq n$, however the regions are very small. Inset shows the rotation number for different values of c_{oe} as a function of c_{eo}. In the picture, $c_{oe} = \{0.7, 0.5, 0.3, 0.1\}$ from left to right. We were not able to find any bistable regions.

although it takes smaller values of c_{eo} for the E cell to fire due to it receiving two oscillatory inputs.

We note that in all choices of (c_{oe}, c_{eo}) there was always synchrony between the oscillators x and z. This is because the excitable cell is receiving two oscillatory inputs, so it is as if there is only one oscillator coupled to the excitable cell that has twice the coupling strength. In other words, with $x(t) = z(t)$, equation (5) is identical to (4) with c_{eo} doubled, as one can see in the figure.

2.2.2.1 Heterogeneity in OEO system

Next, we explore how the change in oscillator frequency affects existence of our phase-locked solutions. This focuses on parameter d in system (5), which we initially kept at zero. Rather than vary c_{oe} or c_{eo}, we have chosen to co-vary them along the lines shown in Figure 5a as this guarantees that the locking pattern is constant. For each (c_{eo}, c_{oe}) parameter choice, we will increase d from zero to determine when the phase-locking becomes unstable. This allows us to explore the efficacy of the E cell in coupling the two O cells. From Figure 5b, when the E cell fires, we can see there is a wider range of d values and thus the stability of the firing phase-locked solutions is less sensitive than the 0:1-s solution. We remark that there is a "sweet" spot for coupling strength along this line that maximizes the allowable heterogeneity.

2.2.3 OEEO chain

We move on to two E cells and obtain the equations

$$\begin{aligned}
\dot{x} &= \omega + d + c_{oe}\sin(y_1 - x) \\
\dot{y}_1 &= f(y_1) + c_{ee}\sin(y_2 - y_1) + c_{eo}\sin(x - y_1) \\
\dot{y}_2 &= f(y_2) + c_{ee}\sin(y_1 - y_2) + c_{eo}\sin(z - y_2) \\
\dot{z} &= \omega - d + c_{oe}\sin(y_2 - z).
\end{aligned} \tag{6}$$

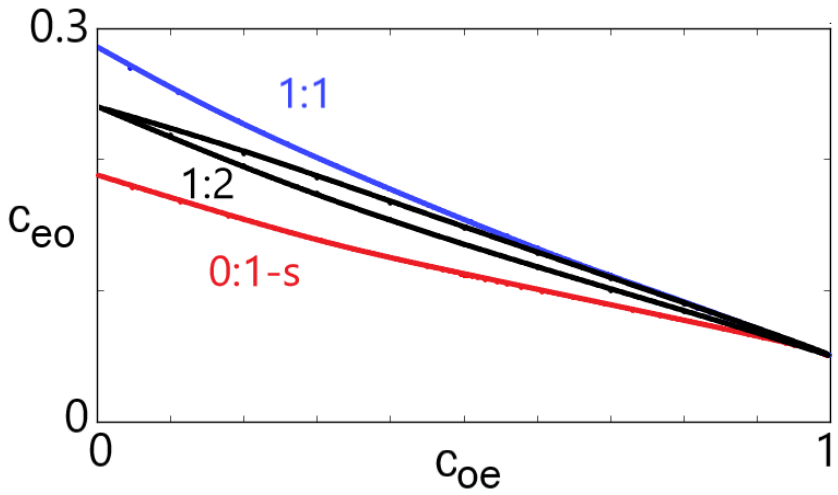

Figure 4: Dynamics of Eq. (5) as the connectivity varies. Again, below the red (bottom) curve, the excitable cell does not fire, and above the blue (top) curve, it fires in a 1:1 manner with the oscillator. In between the black (middle) lines is the 1:2 locking. Similar to the OE system, we did not find any bistable regions.

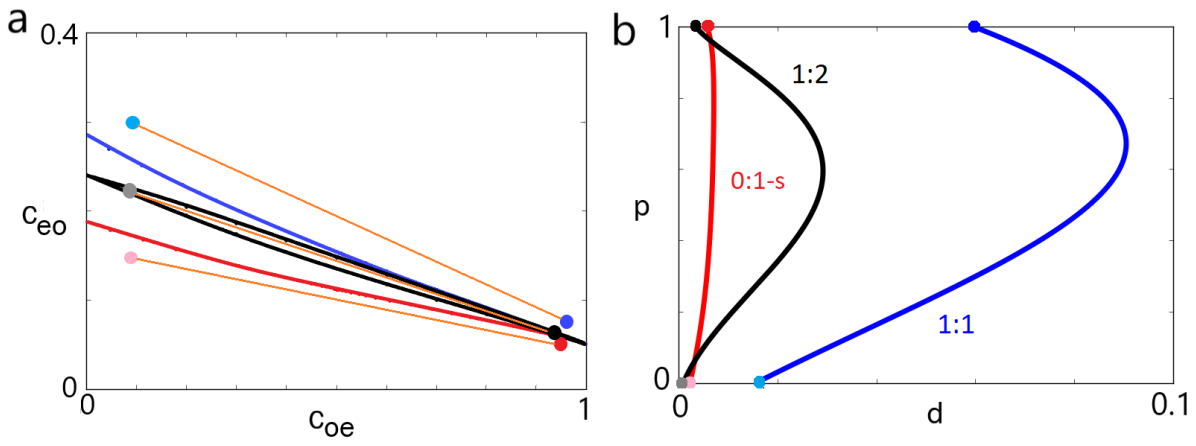

Figure 5: The left figure shows the lines chosen for the OEO chain. These have the form of $(c_{oe}, c_{eo}) = (k_1, c_1) + p(d_k, d_c)$ for $0 \leq p \leq 1$. Light colored dots on the left of each line correspond to $p = 0$ and dark colored dots on the right of each line are when $p = 1$. The 0:1-s line goes from $(c_{oe}, c_{eo}) = (0.1, 0.15)$ to $(0.95, 0.05)$. The line between the black curves goes from $(0.1, 0.22)$ to $(0.95, 0.06)$. Lastly, the line in the 1:1 region on the top goes from $(0.1, 0.3)$ to $(0.95, 0.075)$. For each curve in the right figure, the labelled region is stable on the left side of the curve and unstable on the right side of the curve. When $d = 0$, all phase-locked solutions are stable. As d increases, some points on those lines may no longer stay in the phase-locked pattern they were originally in. The curves on the right graph correspond to the boundary when , for each point (c_{oe}, c_{eo}) chosen, the original phase-locked solution switches from stable to unstable. It is clear that 1:1 remains stable for a wider range of d values whereas the stability of the 0:1-s region is the most sensitive to changes in d.

There is now one more parameter, c_{ee}, which governs the strength of connectivity between the two E cells. We will also set $\omega = 1$, $d = 0$ and restrict the other coupling parameters to lie in $(0, 1)$. The addition of another E cell makes the dynamics much more complex with multiple stable attractors.

Figure 6 shows these behaviors for $c_{ee} = 0.5$. Since $d = 0$, then $x = z$ and $y_1 = y_2$ (the synchronous solution) is invariant under the dynamics of (6) and, in this case, it reduces to the dynamics of (4). This is why the essential difference between this and Figure 3 is the boundaries of the 0:1 regions. Additionally, we plotted the 1:3 region where the two excitable cells fire synchronously once for every three times the two oscillators synchronously fire.

In addition to the synchronous behavior, we also find other stable behavior, where the E cells do not fire. There appear to be three distinct types of this behavior: synchrony (0:1-s), anti-phase (0:1-a), and "mixed-state" (0:1-m). This is quite different than the OEO system where we were unable to find any stable behavior when x and z weren't synchronized. Anti-phase exists and is stable throughout the region bounded by the red curve and the magenta curve. Synchrony between the two oscillators and the two excitable cells without the E cells firing is stable below the cyan curve. Between the cyan and the magenta curve, we find the so-called "mixed" state. Figure 7 shows the excitable cells undergoing these three behaviors. We can best understand the mixed state as follows: Say $c_{oe} = 0.78$ and c_{eo} is at a value below the cyan curve where there is stable 0:1 synchrony. Increasing c_{eo} (a vertical line in Fig. 6 at $c_{oe} = 0.78$) results in a pitchfork or symmetry-breaking bifurcation where a stable branch of non-synchronous asymmetric orbits arises with a phase-difference between synchrony and anti-phase. This is shown in Figure 7d. The magenta and cyan curves in Fig. 6 depict these pitchfork bifurcations (A zoomed in version near $c_{oe} = 1$ is shown in Figure 9).

Other regions not accounted for include the region below the 1:1 synchrony line and above anti-phase line and the top 1:2 line. This large space does not have any apparent phase-locked pattern and appears to be chaotic. We note that this region existed in our previous models as well. For example, when $c_{ee} = 0.5, c_{oe} = 0.11, c_{eo} = 0.49$, Figure 8 shows z and y_2 vs x in panel (a) and a Poincare section through $x = 1$ in panel (b). We have crudely estimated the Liapunov exponent to be about 0.04 by computing the slope of the logarithm of the absolute difference between two trajectories over time. Another observation

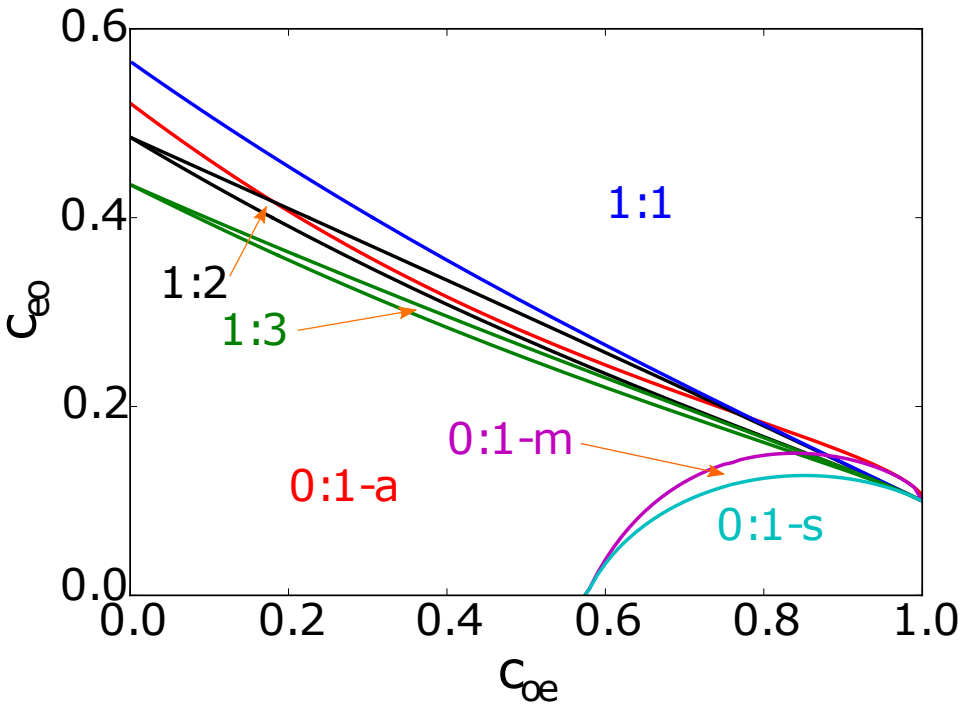

Figure 6: Regions of different phase locking for the OEEO model when $c_{ee} = 0.5$ as a function of the parameters c_{eo} and c_{oe}. Everything above the blue curve is synchrony with $y_{1,2}$ firing in 1:1 with x, z. Between the red curve and the magenta curve, x, z fire in anti-phase and $y_{1,2}$ do not fire and are not synchronized. Within the black curves, x, z are synchronous and $y_{1,2}$ fire in a 1:2 manner. Within the green curves, x, z are synchronous and $y_{1,2}$ fire in a 1:3 manner. Between the magenta and cyan curves, x, z and $y_{1,2}$ have a mixed phase-difference and $y_{1,2}$ don't fire. Finally, below the cyan curve, x, z and $y_{1,2}$ are synchronous and $y_{1,2}$ don't fire. In other regions such as $c_{oe} = 0.11, c_{eo} = 0.49$, we have found apparent chaotic behavior.

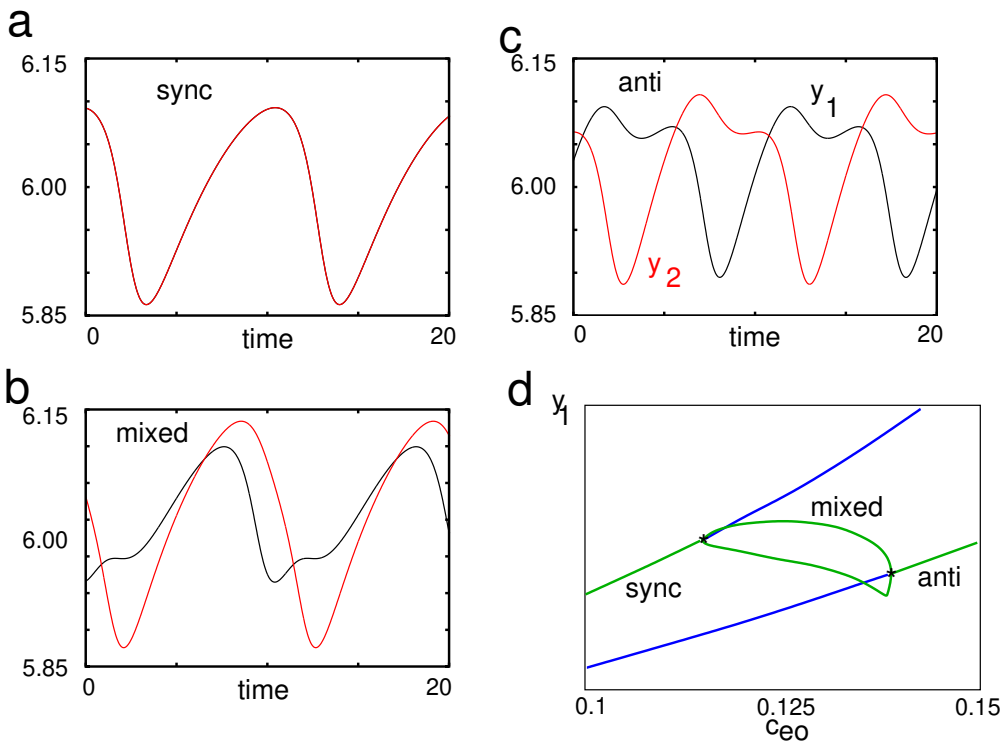

Figure 7: The three types of sub-threshold dynamics for $y_{1,2}$ with $c_{oe} = 0.78, c_{ee} = 0.5$. In (a), $c_{eo} = 0.1$, we have 0:1 synchrony. In (b), $c_{eo} = 0.13$, we have the "mixed" state which is neither synchronous nor anti-phase. In (c) with $c_{eo} = 0.15$, we have the anti-phase state. Lastly, (d) shows the pitchfork (symmetry-breaking) bifurcation diagram showing the emergence of the mixed state. Begin with the top line in the synchrony branch and as c_{eo} increases, the line changes from stable periodic orbits (green) to unstable periodic orbits (blue). While on the bottom line, the anti-phase branch changes from unstable periodic orbits to stable periodic orbits as c_{eo} increases. In between, there is a region where neither synchrony nor anti-phase is stable and this is where the mixed state is stable.

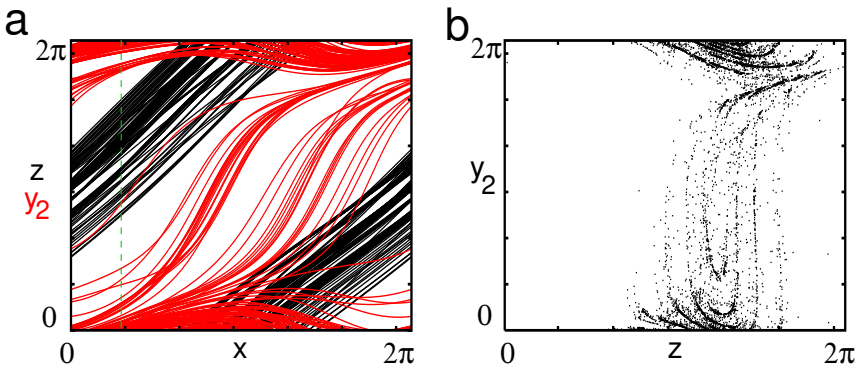

Figure 8: Putative chaos in Eq. (6) when $c_{oe} = 0.11, c_{eo} = 0.49, c_{ee} = 0.5$. Picture (a) shows phase space trajectories of z and y_2 vs x. Picture (b) is a Poincare section through $x = 1$, the thin dotted green line in panel (a), showing y_2 vs z.

we noticed was bistability; the OEEO chain is the smallest chain we have found that exhibits regions of bistability, that is, the long term dynamics depend on the initial data. Figure 9 shows a zoomed in version of Figure 6. Regions labeled by Greek letters indicate regions of bistability. Notice that region β actually extends further back all the way to $c_{oe} = 0$, see Figure 6.

2.2.3.1 Heterogeneity

We can apply similar numerical analyses to the OEEO chain as with the OEO chain and compare the existence of locked solutions as the oscillator frequencies vary from ω in (6). However, unlike the OEO chain, we can also investigate bistable regions as well; this will give us a more direct comparison between which region has a higher threshold for heterogeneity since in these regions, the parameters can remain the same. First, we look at the 4 long term dynamics separately. Figures 10a and 10b show the four lines we use for each of the four main regions: 1:1, 1:2, 1:3, and 0:1-a. Using these, Figure 10c shows the frequency behavior for each point on the four lines. It is clear that the stability of the 1:1 synchrony region remains is the least sensitive to changes in the heterogeneity parameter d. Although the 1:2 and 1:3

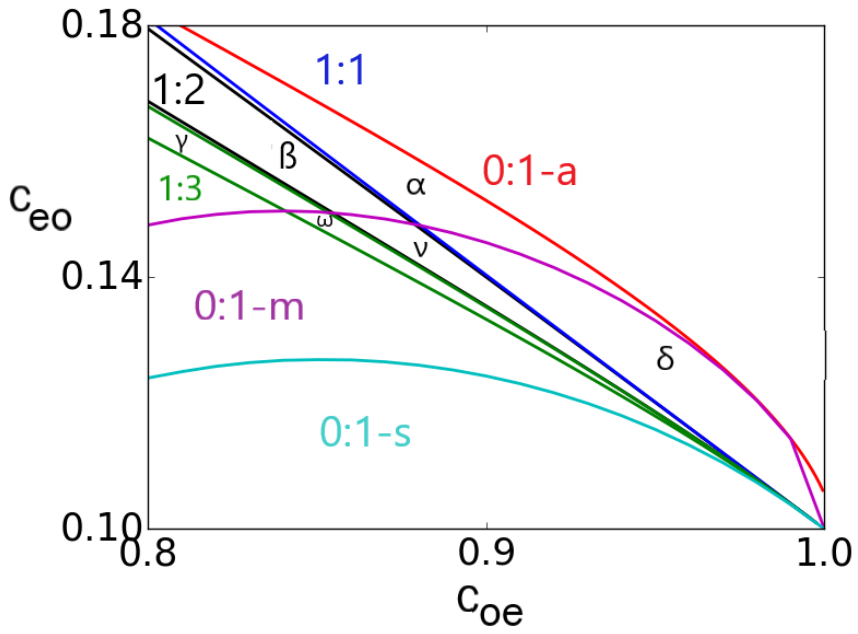

Figure 9: Zoomed in picture of Figure 6 showing different regions of bistability. In the region labeled δ, there is both 1:1 synchrony and 0:1 mixed, while in region α, 1:1 synchrony is bistable with anti-phase (0:1-a). In regions β and γ, anti-phase behavior coexists with 1:2 and 1:3 locking respectively and regions ν and ω, mixed sub-threshold behavior coexists with 1:2 and 1:3 locking respectively.

regions are much smaller than the 0:1-a region, their stabilities are less sensitive to changes in d compared to the stability of the 0:1-a region. This could suggest that the excitable cells firing plays a key role in maintaining locking as d increases and we could test this by looking at the stability of the 0:1-s region as the heterogeneity changes. This is similar to what we saw in the OEO system with Figure 5. Also similar to the OEO system, there is a "sweet" spot where the system is most tolerant of frequency differences.

We can also look at the regions of bistability. There are two regions we looked into: when 0:1-a and 1:2 were both stable and when 0:1-a and 1:1 were both stable. Besides the β region in Figure 9, one can see in Figure 6 that the 0:1-a and 1:2 bistable region does not break as c_{oe} increases. Thus, we used two lines for this region in order to capture as much range for c_{eo}. Figure 11a shows what happens as d increases from zero. As the first line moves towards the very narrow region in the middle (near c_{oe}=0.4), the 1:2 stability becomes more sensitive to changes in d and the 0:1-a region becomes less sensitive. Then, as the second line enters the β region, 1:2 locking allows a bigger range of d before becoming unstable. The other region of bistability we looked into was the α region in Figure 9. We can see initially the 1:1 synchrony is more tolerable but as we move down into what was the δ region, it is the 0:1-a dynamics that are more robust as d increases (see Figure 11b).

2.2.4 Weak coupling analysis

As shown previously, when c_{eo} is small enough, the E cells do not fire and there can be several types of dynamics including synchrony, anti-phase, and a non-synchronous locked state (the "mixed" state). Looking back at Figure 6, it appears that in the limit as $c_{eo} \to 0$, there is an abrupt transition from anti-phase to synchrony as c_{oe} crosses a critical value (around $c_{oe} = 0.57$). We will now address this point using weak coupling analysis. This method extends to arbitrary length chains but for simplicity, we just perform the analysis

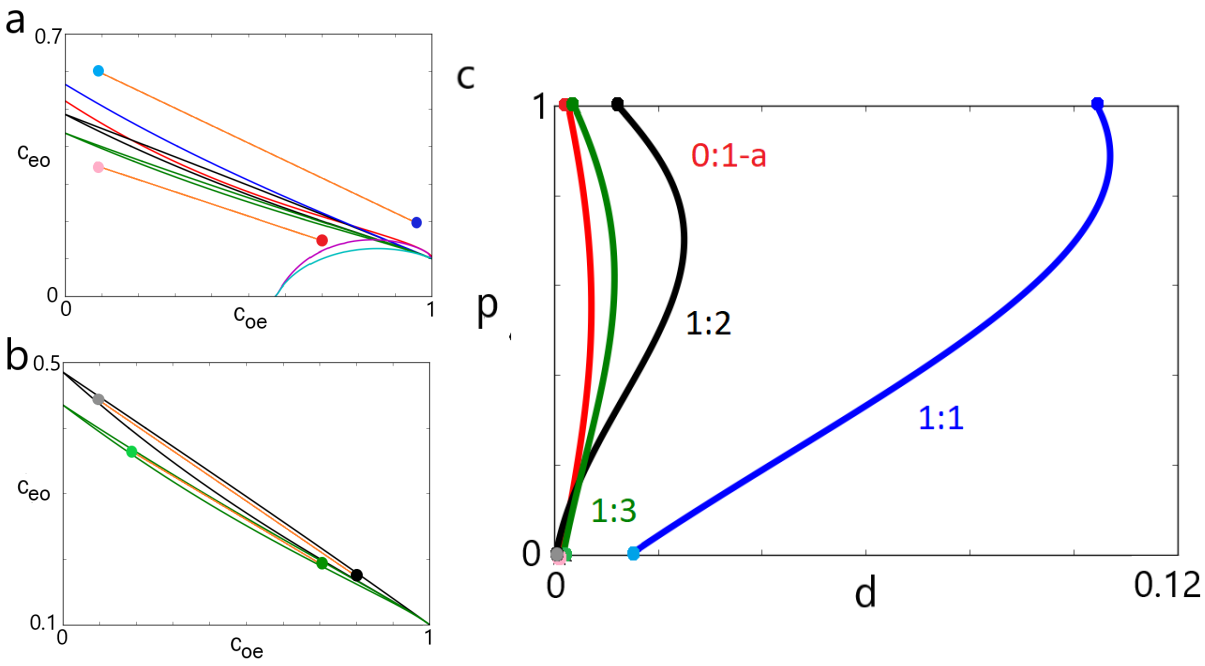

Figure 10: In the left two figures, we show the lines that we use for the non-bistable regions. For the 1:1 locking, our parameters go from $(c_{oe}, c_{eo}) = (0.1, 0.6)$ to $(0.95, 0.2)$ and for 0:1-a locking, our parameters go from $(0.1, 0.35)$ to $(0.7, 0.15)$. The second picture shows our paths for the 1:2 and 1:3 regions. For these, we have our parameters going from $(0.1, 0.44)$ to $(0.8, 0.174)$ and $(0.2, 0.36)$ to $(0.71, 0.19)$, respectively. In the right figure, we show how large the heterogeneity parameter d can become for each set of parameters on these lines before the corresponding phase-locking becomes unstable. The dots on the bottom of this figure correspond to the beginning of each path and the dots on the top of this figure correspond to the dots at the end of each path. As our parameter p increases, we increase c_{oe} and decrease c_{eo} according to the orange diagonal lines in (a) and (b). The curves are color-coded to their respective regions. We can see that the stability for the 1:1 locking is least sensitive to changes in d and 0:1-a stability is most sensitive despite it having a large stability region.

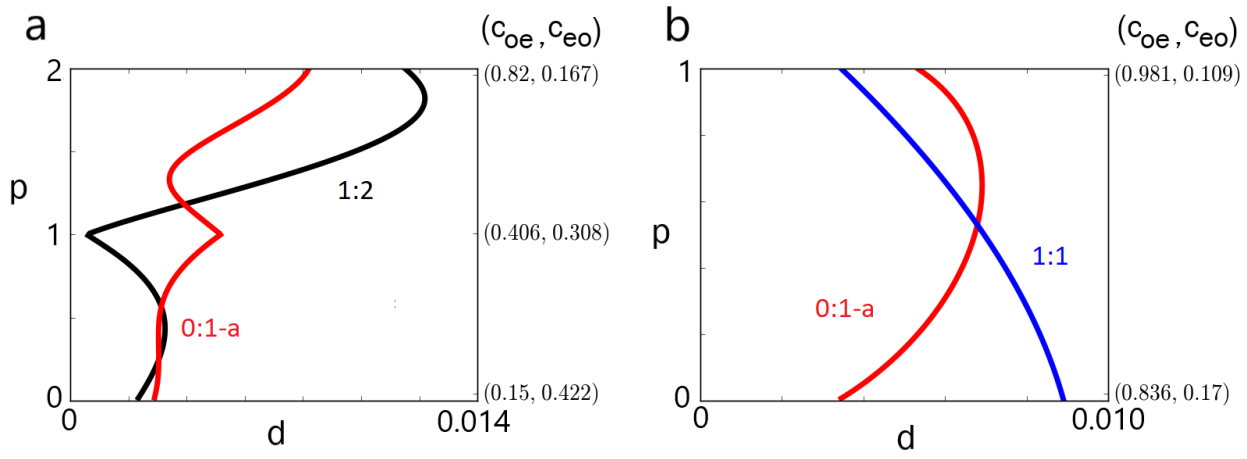

Figure 11: Effects of heterogeneity in bistable regions of the OEEO system. The right y-axis shows the path's starting and ending points for (c_{oe}, c_{eo}). In (a), the first line begins at $(0.15, 0.422)$ in between the black lines and below the red line in Figure 6 where 0:1-a and 1:2 are bistable, and goes to $(0.406, 0.308)$, where it is very narrow but still bistable. The second line starts at this point and continues into the β region (see Figure 9) where it ends at $(0.82, 0.167)$. The black 1:2 line (resp. red 0:1-a line) shows the maximum d can be before losing stability of the 1:2 (resp. 0:1-a) locking. In (b), we look at a line in the α region (see Figure 9), where 0:1-a and 1:1 are bistable. When $d \neq 0$, the 0:1-m region deflates and thus, the α and δ region become one. Our path goes from $(0.836, 0.17)$ to $(0.981, 0.109)$. The blue 1:1 line (resp. red 0:1-a line) represents the maximum d before 1:1 (resp. 0:1-a) stability is lost.

for the OEEO chain. Let $c_{eo} = \varepsilon$ where $0 < \varepsilon \ll 1$ is a small parameter and so we have

$$\begin{aligned} x' &= 1 + c_{oe}\sin(y_1 - x) \\ z' &= 1 + c_{oe}\sin(y_2 - z) \\ y_1' &= f(y_1) + \varepsilon\sin(x - y_1) + c_{ee}\sin(y_2 - y_1) \\ y_2' &= f(y_2) + \varepsilon\sin(z - y_2) + c_{ee}\sin(y_1 - y_2), \end{aligned}$$

and as a reminder, $f(y) = 1 - b\cos(y)$. When $\varepsilon = 0$, the stable solution is $y_1 = y_2$ so this implies we have $y_{1,2} \equiv k = -\arccos(1/b)$. If $0 < c_{oe} < 1$, there is a $T-$periodic solution, $U(t)$, to $U' = 1 - c_{oe}\sin(U)$ with $U(t+T) = U(t) + 2\pi$. Note that

$$T = \int_0^{2\pi} \frac{dx}{1 - c_{oe}\sin(x)}.$$

Thus for ε small, we expect that $x(t) \approx k + U(t + \theta_x)$ where θ_x is an arbitrary phase shift. To formalize this argument, we use the method of multiple scales by letting $s = t$ be the fast time, and $\tau = \varepsilon t$ be the slow time and expand $x, z, y_{1,2}$ as a power series in ε, e.g.,

$$\begin{aligned} x(t) &= x_0(s,\tau) + \varepsilon x_1(s,\tau) + \dots, \\ y_1(t) &= y_1^0(s,\tau) + \varepsilon y_1^1(s,\tau) + \dots, \end{aligned}$$

where we assert each term is $T-$periodic in s. With this ansatz, in the first order expansion we see that $x_0(s,\tau) = k + U(s + \theta_x(\tau))$, $z_0(s,\tau) = k + U(s + \theta_z(\tau))$, and $y_{1,2} = k$ where $\theta_{x,z}(\tau)$ are unknown. In the second order expansion,

$$\begin{aligned} \partial_s x_1 + U'(s+\theta_x)\partial_\tau\theta_x &= c_{oe}\cos(U(s+\theta_x))[y_1^1 - x_1] \\ \partial_s z_1 + U'(s+\theta_z)\partial_\tau\theta_z &= c_{oe}\cos(U(s+\theta_z))[y_2^1 - z_1] \\ \partial_s y_1^1 &= b\sin(k)y_1^1 + c_{ee}(y_2^1 - y_1^1) + \sin(U(s+\theta_x)) \\ \partial_s y_2^1 &= b\sin(k)y_2^1 + c_{ee}(y_1^1 - y_2^1) + \sin(U(s+\theta_z)), \end{aligned} \tag{7}$$

where $\partial_\gamma = \dfrac{\partial}{\partial \gamma}$. The last two equations can be written as

$$\frac{\partial}{\partial s}\begin{pmatrix} y_1^1 \\ \\ y_2^1 \end{pmatrix} = A\begin{pmatrix} y_1^1 \\ \\ y_2^1 \end{pmatrix} + \begin{pmatrix} \sin\big(U(s+\theta_x)\big) \\ \\ \sin\big(U(s+\theta_z)\big) \end{pmatrix} \tag{8}$$

where

$$A = \begin{pmatrix} b\sin(k) - c_{ee} & c_{ee} \\ \\ c_{ee} & b\sin(k) - c_{ee} \end{pmatrix}.$$

By definition of k, this matrix A has strictly negative eigenvalues and thus there is a unique periodic solution to (8). Let $W = (w_1, w_2)^T$ be the periodic solution to

$$\frac{\partial W}{\partial s} = AW + (\sin(U(s)), 0)^T.$$

Then $y_1^1(s,\tau) = w_1(s+\theta_x) + w_2(s+\theta_z)$ and $y_2^1(s,\tau) = w_1(s+\theta_z) + w_2(s+\theta_x)$. Now that we have solved for y_j^1, we turn to x_1, z_1. Consider the linear operator on the space of differentiable $T-$periodic functions:

$$M(s)x := \partial_s x + c_{oe}\cos(U(s))x.$$

Since $U'(s) = 1 - c_{oe}\sin(U(s))$, we see that $x = U'(s)$ is in the nullspace of M. With the standard L^2 inner product, $(f,g) = \int_0^T f(s)g(s)\,ds$, the operator $M(s)$ has an adjoint, $M^*(s)x = -\partial_s x + c_{oe}\cos(U(s))x$ with a nullspace, $1/U'(s)$. With this notation, the equation for $x_1(s,\tau)$ can be written as

$$M(s+\theta_x)x_1 + U'(s+\theta_x)\partial_\tau\theta_x = c_{oe}\cos(U(s+\theta_x))[w_1(s+\theta_x) + w_2(s+\theta_z)],$$

$$M(s+\theta_z)z_1 + U'(s+\theta_z)\partial_\tau\theta_z = c_{oe}\cos(U(s+\theta_z))[w_1(s+\theta_z) + w_2(s+\theta_x)].$$

Taking the inner product of both sides of the x_1 equation with $1/U'(s+\theta_x)$, we obtain the dynamics of θ_x:

$$T\partial_\tau \theta_x = \int_0^T \frac{c_{oe}\cos(U(s+\theta_x))}{U'(s+\theta_x)}[w_1(s+\theta_x) + w_2(s+\theta_z)]\ ds.$$

A simple change of variables gives $\partial_\tau \theta_x = H(\theta_z - \theta_x)$ where

$$H(\phi) = \frac{c_{oe}}{T}\int_0^T \frac{\cos(U(s))}{U'(s)}[w_1(s) + w_2(s+\phi)]\ ds. \tag{9}$$

Similarly, $\partial_\tau \theta_z = H(\theta_x - \theta_z)$. Finally, we let $\phi = \theta_z - \theta_x$ and use $\partial_\tau \theta_z$ and $\partial_\tau \theta_x$ to obtain the weak coupling equation:

$$\partial_s \phi = H(-\phi) - H(\phi) =: G(\phi), \tag{10}$$

where $-G(\phi)/2$ is the odd part of $H(\phi)$. In Figure 12a, we plot $G(\phi)$ for $c_{oe} = 0.5$ and $c_{oe} = 0.7$. When $G'(\phi) > 0$ at the fixed point, the fixed point is unstable and when $G'(\phi) < 0$ at the fixed point, the fixed point is stable. As can be seen from the figure, when $c_{oe} = 0.5$, synchrony ($\phi = 0$) is unstable and anti-phase ($\phi = T/2$) is stable and the reverse is true for $c_{oe} = 0.7$.

From Figure 6, it appears that the synchrony and anti-phase boundary meet at exactly the same point on the c_{oe} axis. This means synchrony and anti-phase change stability at the same point for this choice of parameters. Stability of synchrony (resp. anti-phase) is lost when $G'(0)$ (resp. $G'(T/2)$) changes from negative to positive. Denote $m(s) = \cos(U(s))/U'(s)$ so from the definition of $G(\phi)$:

$$G'(0) = -\frac{2c_{oe}}{T}\int_0^T m(s)w_2'(s)\ ds$$
$$G'(T/2) = -\frac{2c_{oe}}{T}\int_0^T m(s)w_2'(s - T/2)\ ds.$$

Changing s to $s - T/2$ in the second integral and using the observation $m(s+T/2) = -m(s)$ due to the symmetry of the function $\sin(x)$, this shows that $G'(T/2) = -G'(0)$, so that synchrony and anti-phase swap their stability at the same value of c_{oe} independent of any other parameters. In Figures 12b and 12c, we also show how the critical c_{oe} value varies as b or c_{ee} changes. If we change the coupling function between the O and the E cells to some more general odd periodic function, say $\sin(x) + a\sin(2x)$, then the symmetry of $m(s)$ is gone and the branches for synchrony and anti-phase will not meet at a point as $c_{eo} \to 0$.

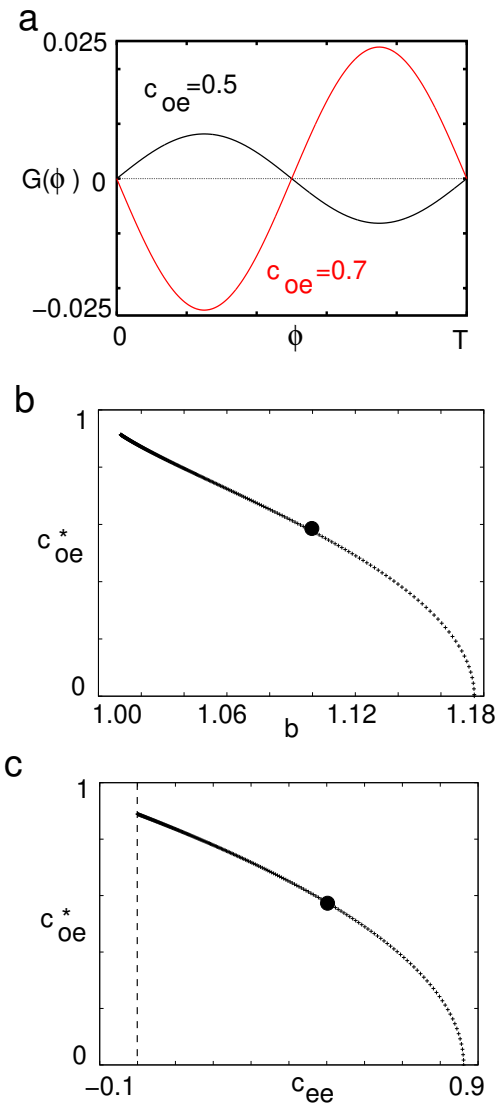

Figure 12: The top figure shows $G(\phi)$ as a function of ϕ. The different graphs describe the flipped behavior for $c_{oe} = 0.5$ and $c_{oe} = 0.7$. In figures (b) and (c), we see how the critical c_{oe} value varies with c_{ee} and b. For $c_{oe} > c^*_{oe}$ (resp. $c_{oe} < c^*_{oe}$), synchrony is stable (resp. unstable) and anti-phase is unstable (resp. stable). The black dots in the bottom two graphs signify the parameters we have used: $b = 1.1$ and $c_{ee} = 0.5$. The dashed line in figure (c) is the vertical axis.

2.2.5 OEEEO and beyond

For chains with 3 or more E cells between the O cells, it is possible to have only the E cells that are coupled to the O cells fire, while the E cells in the middle of the chain fail to fire. For example, Figure 13a shows an OEEEO system where the middle E cell fires and gives rise to 1:2 locking between the oscillators and the excitable cells, while in panel (b), with the same parameters, the middle cell y_2 does not fire and the O cells fire in 1:1 with the outermost E cells.

So far, we have seen that for small chains where all the E cells fire, the only stable solution is synchrony and it is robust to small changes in the relative frequencies of the O cells. Let us now consider a long chain of E cells terminated by two O cells acting as pacemakers. Consider the isolated E chain with no oscillators. If we suppose that the coupling between the E cells is strong enough, then one expects that initiating the first E cell in the chain to fire will result in a traveling wave that propagates down the chain. If at some time after the first E cell is excited, we initiate a wave at the other end, we expect the two waves to collide somewhere in the middle of the chain and they could annihilate completely. This means that the last E cell and first E cell are "unaware" the other E cell fired. If we put the two oscillators on the ends, it seems to imply that the oscillators will not synchronize; rather they can maintain any phase-difference. For example, consider

$$\begin{aligned}
x' &= \omega_x + c_{oe}\sin(y_1 - x) \\
y_1' &= f(y_1) + c_{eo}\sin(x - y_1) + c_{ee}\sin(y_2 - y_1) \\
y_j' &= f(y_j) + c_{ee}\sin(y_{j-1} - y_j) + c_{ee}\sin(y_{j+1} - y_j) \\
y_{100}' &= f(y_{100}) + c_{eo}\sin(z - y_{100}) + c_{ee}\sin(y_{99} - y_{100}) \\
z' &= \omega_z + c_{oe}\sin(y_{100} - z)
\end{aligned}$$

for $j = 2, \ldots, 99$. For this section, we set $c_{oe} = 0.7, c_{eo} = 2, c_{ee} = 3$ and $b = 1.1$. Figure 14a shows a simulation when $\omega_x = \omega_z = 1$ for four different initial conditions. The left panel shows us that the two oscillators lock but the phase-difference between x and z varies each time. The right panel shows why this happens: waves initiated at the end points collide in the middle and, thus, cannot alter the timing of their opposite oscillators. However, if we make

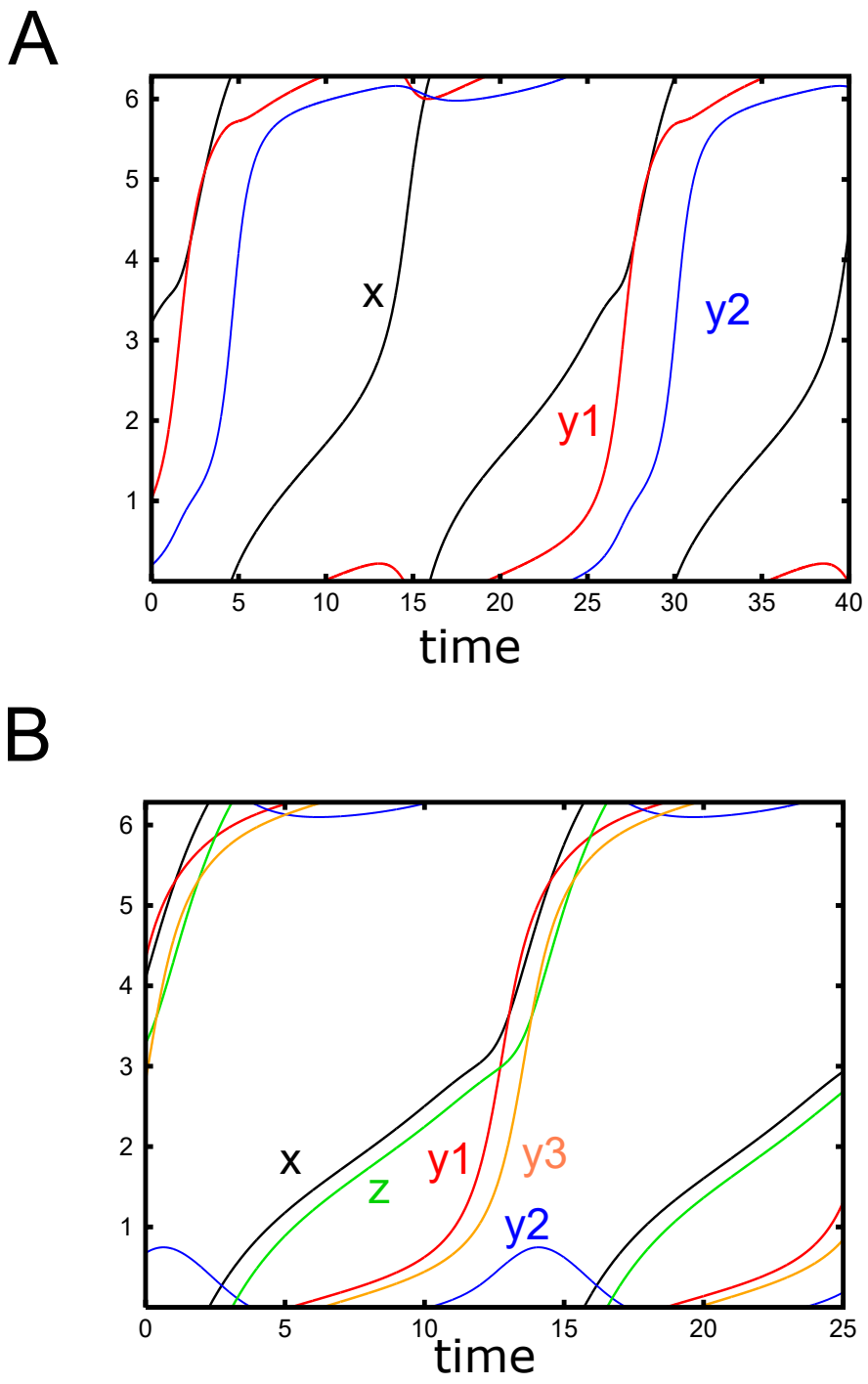

Figure 13: Example of bistability in an OEEEO chain. The parameters are $c_{oe} = 0.75, c_{eo} = 0.25$, and $c_{ee} = 0.18$. In (a), $x = z$, and $y_1 = y_3$ and y_2 (the middle excitable cell) also fires all in synchronous 1:2. In (b), the outer $y_{1,3}$ fire with the O cells in 1:1 but the middle E cell y_2 does not fire and the oscillators do not synchronize.

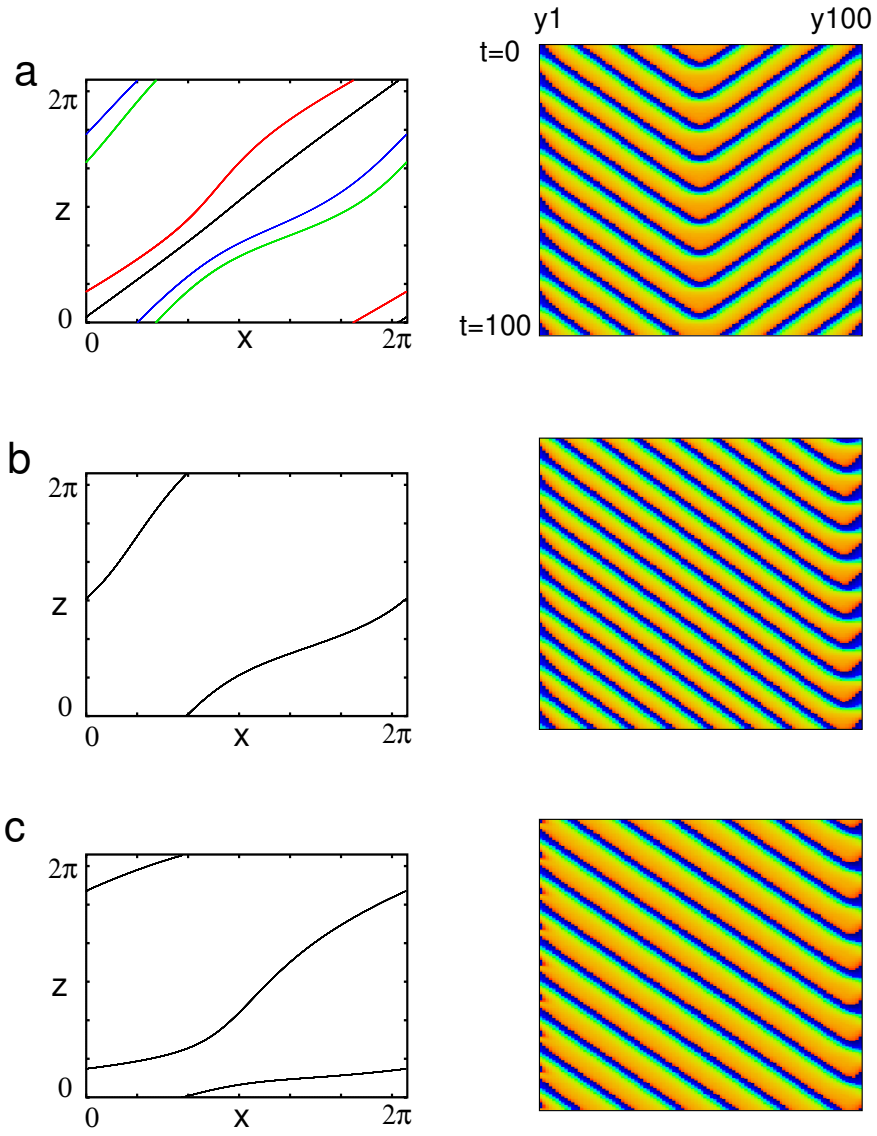

Figure 14: Chain of 2 oscillators with 100 excitable cells in between. (a) Phase plane showing the long-time behavior of the two oscillators for 4 different initial data; right is a space-time plot. The frequences are equal ($\omega_x = \omega_z$) and they are able to maintain any phase difference. (b) Same as (a) but $\omega_x = 1.1, \omega_z = 0.9$; a fixed 1:1 locking always occurs. (c) Same as (a), but $\omega_x = 1.5, \omega_z = 0.5$ and a 1:2 locking occurs.

one oscillator faster than the other, then the point of intersection of the waves moves toward the slower oscillator as the fast oscillator dictates the frequency and becomes a pacemaker. Figure 14b shows this with $\omega_x = 1.1$ and $\omega_z = 0.9$. Once there is a single phase-locked solution, there appears to be a unique attractor. Increasing the frequency difference further (Figure 14c) leads to 1:2 locking where x goes 2 cycles and the rest of the medium goes 1 cycle. Differences in the frequencies of the oscillators allow for the timing information to propagate down the chain and lock the oscillators.

2.2.6 Biophysical models

In this chapter, we have used a one-dimensional model for excitability that is equivalent to the normal form for a general system near a saddle-node infinite cycle bifurcation (SNIC). A simple and well-known neural model that has a SNIC is the Morris-Lecar (ML) model given in the beginning of this chapter. Thus, we turn our attention to this model and look at the OEEO system. Similar to equation (6), we hold $c_{ee} = 0.1$ and vary (c_{oe}, c_{eo}) to compare this ML model to the dynamics of equation (6).

Figure 15a shows the regions of stability as we vary (c_{oe}, c_{eo}) for the ML model. This figure was created by following bifurcation points using AUTO in XPP (see [17]), and then combining the two-parameter data and tracing the curves using splines. We show a number of different regions, but this is by no means exhaustive. We compare this figure to Figures 6 and 9. We first note that as in the simple phase model, the largest regions correspond to 1:1 synchronous locking and 0:1 locking in either synchrony, mixed, or anti-phase for increasing values of c_{eo}. A notable difference from the phase model is the large region of 2:3-m in the ML system. Interestingly, the O cells do not synchronize, but operate in the mixed phase mode. Another difference is that the region of 1:2-s is somewhat limited in the ML model when compared to the phase model. We have labeled three different regions, α, β, δ in which there is bistability, similar to the phase model in Figure 9. For example, in region β there is bistability between 1:2-s and 0:1-a. Both regions α, δ have bistability between 1:1-s and 0:1. However, due to the existence of the large 2:3-m region, there is actually tristability with the 2:3-m state. The 2:4-s state occurs via a period doubling bifurcation of the 1:2-s

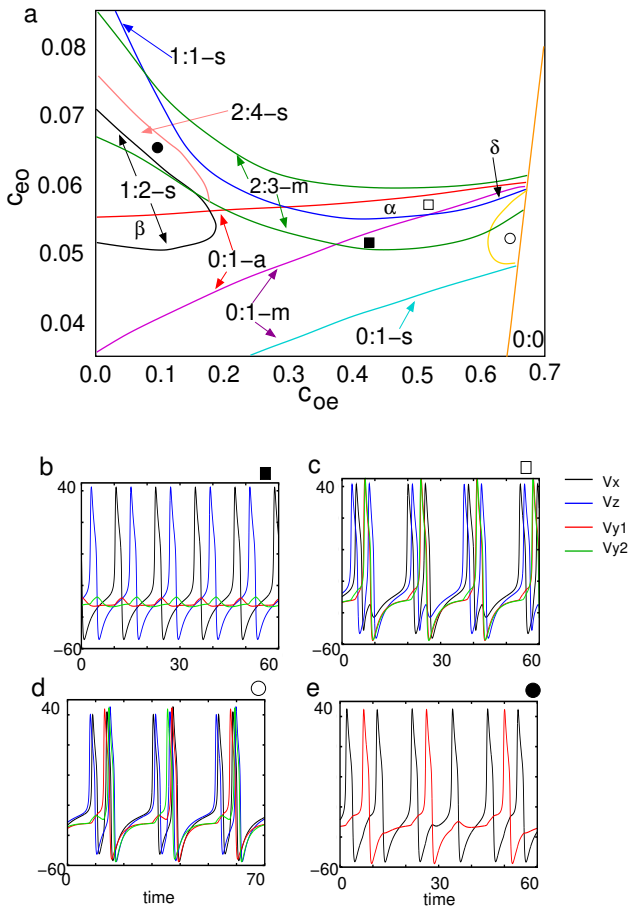

Figure 15: (a) Regions of stability for the ML model as constructed from a bifurcation analysis. Stable locking regions are delineated by colored lines with arrows pointing to the boundaries. The symbols s, m, a correspond to the oscillators being synchronous, mixed, or anti-phase. There are many regions of multistability; three are marked α, β, δ corresponding to the regions in Fig. 9. Markers correspond to parameters for the time series shown in b-e. Values of (c_{oe}, c_{eo}) correspond to the markers in (a). (b) 0:1-m, $(0.4, 0.05)$; (c) 2:3-m, $(0.5, 0.057)$; (d) 2:4-m, $(0.63, 0.05)$; (e) 2:4-s, $(0.1, 0.065)$. In (e), $V_x = V_z$ and $V_{y_1} = V_{y_2}$ so they overlap.

state (the upper curve in the 1:2-s region). The 0:1-m state also loses stability via a period-doubling bifurcation as c_{oe} increases (shown by the gold C-shaped region on the right side of the 0:1-m region). Like the phase model, all of the locked oscillatory regions terminate as a stable fixed point emerges when c_{oe} is large enough. This region is labeled 0:0. Figures 15b-e show representative voltage traces in some of the different regions indicated by the markers in panel (a).

In summary, we have seen that the simple phase model for interacting oscillatory and excitable cells is a fair predictor of the qualitative dynamics of biophysical networks of coupled oscillator and excitable cells. In particular, the latter undergo many of the same bifurcations and transitions between states as well as having similar regions of bistability.

2.3 Discussion

Throughout this project, we have studied some simple networks in which a pair of oscillators is indirectly coupled to active nonlinear elements, namely excitable systems. We showed several distinct qualitative behaviors that include in-phase, anti-phase, and mixed-phase synchronization both when the excitable cells fired and did not fire. We also found some regimes of seemingly chaotic dynamics in between phase-locked regions. With the smallest of chains, bistability between the phase-locked regions was impossible; however, if the chain increases in length, many bistable regions can appear. We found that when the excitable cells were silent, that is they operate in the subthreshold regime, the interactions between the two oscillators could be analyzed through weak coupling analysis and was amenable to averaging methods and phase reduction. Further, when the excitable cells were active, the ability to phase-lock is more robust to changes in the oscillator frequencies than when the excitable cells were silent. We also saw that for very long chains of excitable cells, a small difference in the intrinsic frequency of the oscillators is more conducive to rapid and stable phase-locking than if the oscillators were identical. While this may seem counterintuitive, one can regard it as a case when the faster oscillator becomes the "leader" and thus the excitable cells and the slower oscillator are effectively forced. The slow oscillator gets overpowered in the rhythm.

We also showed that the simple phase models that formed the bulk of the chapter shared similar qualities and structure with the Morris-Lecar model, a standard biophysical model for a neuron.

Similar work has been done in [64] where they perform a bifurcation analysis between two coupling parameters to look at the bursting behavior in a network of excitable neurons; they also perform weak coupling analysis. Additionally, [65] also investigated rhythm generation between pacemaker neurons in the pre-Bötzinger complex. However, both of these works were with synaptic coupling rather than diffusive coupling. There are many unanswered questions that remain after this chapter. Here, we looked at one-dimensional chains; however, a more biologically realistic scenario would involve a small number of oscillators embedded in a two-dimensional network of excitable cells. Indeed, this is a geometry more akin to the examples that motivated this work in the Introduction. Further, one may want to introduce all-to-all coupling between the excitable cells instead of chain-coupling. This is one of the things we do in the next chapter; we also make the excitable cells noisy, a much more realistic approach.

3.0 Oscillations through noise-driven excitable cells

3.1 Introduction

In the previous project, we considered a chain of excitable cells connecting two oscillatory cells at the ends. We found that the oscillatory cells, depending on the coupling strength, could be in snychrony or out of synchrony. Synchronization of coupled cells can lead to oscillations which are used to transfer and modulate signals throughout most living systems. Noise and heterogeneity are major characteristics of most physical and biological systems, thus, there has been a long time interest in how noise affects oscillatory dynamics ([18, 19, 20, 21]). Many biological systems (such as cardiac cells [22], neurons [23], and other cells [24]) are not intrinsically oscillatory, rather, they are *excitable*. That is, as discussed earlier, they have a globally stable rest state and a "threshold", and if the threshold is exceeded, there is an amplification of voltage, calcium, or some other quantity, before returning to rest. However, when coupled and driven with noise or heterogeneity, they can often produce synchronized oscillations and other behavior [25, 26, 27, 28, 29, 30, 31].

We will use excitable cells which are all-to-all coupled phase models with a sinusoidal interaction function of the phase-differences (Kuramoto model). We start by considering external Gaussian noise, also called *dynamic* noise, where the noise depends on time (see [37, 42, 43, 44]). We initially apply mean field theory (MFT) and study the probability density related to our N-cell system to find regions in parameter space where there are oscillations. We also investigate other ways to reduce the dimension of this model by truncating it further based on cumulants (see [45]). After this, we employ heterogeneous noise, noise that is independent of time and also labelled "quenched" noise in the physics community, which has been studied in other places in math biology (see [46, 47, 48, 49]). We show that the commonly used Cauchy distribution will never give rise to macroscopic oscillations for our coupled excitable system. For other distributions which we describe later, we do find parameters for our system that generate macroscopic oscillations. We remark on the similarities and differences between these distributions as well. In all of the cases that we

investigate, the transition to oscillations and their subsequent loss appear to occur via the same mechanism. Thus we perform a rescaling analysis, letting the heterogeneity/noise go to zero, which then simplifies the dynamics and shows the universality of these transitions. Lastly, we change the coupling of our model by adding a cosine term and doing this creates oscillations into the once non-oscillatory Cauchy distribution model.

3.2 Results

We will focus our analysis on the following simple model for a coupled excitable medium with N cells:

$$\dot{u}_j = \mu - \cos(u_j) + \frac{c_{ee}}{N}\sum_{k=1}^{N} H(u_k - u_j) + \eta_j + \xi_j(t), \quad u_j(t) \in S^1 = [0, 2\pi). \tag{11}$$

Here $c_{ee} > 0$ and $H(u)$ is the coupling function which has the form $H(u) = \sin(u)$. The additive term η_j is heterogeneous zero-mean noise and $\xi_j(t)$ is independent zero mean Gaussian noise with $\langle \xi_j(t)\xi_k(s)\rangle = 2\sigma^2\delta_{jk}\delta(t-s)$. Typically, $0 < \mu < 1$ so that in absence of coupling, there is a stable rest state with $u^- = -\arccos(\mu)$ and an unstable fixed point at $u^+ = \arccos(\mu)$. If the initial data points are slightly past u^+, then $u(t)$ grows until it reaches $2\pi + u^-$. In the coupled system, noise can cause one or more of the u_j to cross this threshold. The coupling can induce other cells to cross threshold and thus induce a chain reaction that could lead to a synchronous explosion of activity. In the case of heterogeneous noise, for some of the cells, $\mu + \eta_j > 1$, so that in absence of coupling, they will spontaneously oscillate and then the coupling could induce the others to oscillate. There is a balance in the coupling strength, noise, and excitability. If the coupling is too weak, the cells that escape from rest are unable to pull the other cells along while if it is too strong, the cells will be pinned to the mean state which is at rest. Our goal is to analyze the conditions under which the coupling and noise/heterogeneity balance out enough to generate macroscopic synchronous oscillations in the limit as $N \to \infty$.

3.2.1 Gaussian noise

We begin with Gaussian noise, $\eta_j = 0$, and use the approach of [25]:

$$\dot{u}_j = \mu - \cos(u_j) + \frac{c_{ee}}{N}\sum_{l=1}^{N}\sin(u_l - u_j) + \xi_j(t) \tag{12}$$

where $\xi_j(t)$ represents time dependent Gaussian noise with mean 0 and variance $2\sigma^2$ as explained above. By taking the limit as $N \to \infty$,

$$\lim_{N\to\infty}\frac{c_{ee}}{N}\sum_{l=1}^{N}\sin(u_l - u_j) = I(t,u) = c_{ee}\int_{-\pi}^{\pi}\sin(v-u)F(t,v)\,dv$$

where $F(t,u)$ is the probability density for the phase u at time t, and satisfies the nonlinear Fokker-Planck equation (FPE):

$$\frac{\partial}{\partial t}F(t,u) = -\frac{\partial}{\partial u}\Big(F(t,u)\Big(\mu - \cos(u) + I(t,u)\Big)\Big) + \sigma^2\frac{\partial^2}{\partial u^2}F(t,u) \tag{13}$$

as shown in [25, 43, 45]. We further add the conditions that $F(t,u)$ is 2π-periodic in u and is normalized on $[-\pi,\pi]$. Because $F(t,u)$ is periodic, we may assume

$$F(t,u) = \frac{1}{2\pi}\Big(\sum_{n=0}^{\infty}a_n(t)\cos(nu) + \sum_{n=1}^{\infty}b_n(t)\sin(nu)\Big) = \frac{1}{2\pi}\sum_{n\in\mathbb{Z}}\rho_n(t)e^{-inu}$$

with $\rho_0 = 1$ and $\rho_{-n} = \rho_n^*$. By plugging the Fourier expansion into Eq (13) and equating terms, we find

$$\frac{d\rho_n}{dt} = n\Big(i\mu\rho_n - \frac{i}{2}\big(\rho_{n-1} + \rho_{n+1}\big) - \frac{c_{ee}}{2}\big(\rho_1^*\rho_{n+1} - \rho_1\rho_{n-1}\big) - n\sigma^2\rho_n\Big).$$

Letting $\rho_n = r_n e^{i\theta_n}$, we have equations for the amplitude and phase:

$$
\begin{aligned}
\dot{r}_n &= \frac{n}{2}\Bigg(r_{n+1}\sin(\theta_{n+1}-\theta_n) + r_{n-1}\sin(\theta_{n-1}-\theta_n) + \\
&\quad c_{ee}r_1\Big(r_{n-1}\cos(\theta_{n-1}+\theta_1-\theta_n) - r_{n+1}\cos(\theta_{n+1}-\theta_1-\theta_n)\Big)\Bigg) - n^2\sigma^2 r_n \\
\dot{\theta}_n &= n\mu - \frac{n}{2r_n}\Bigg(r_{n+1}\cos(\theta_{n+1}-\theta_n) + r_{n-1}\cos(\theta_{n-1}-\theta_n) - \\
&\quad c_{ee}r_1\Big(r_{n-1}\sin(\theta_{n-1}+\theta_1-\theta_n) - r_{n+1}\sin(\theta_{n+1}-\theta_1-\theta_n)\Big)\Bigg)
\end{aligned}
\tag{14}
$$

with $r_0 = 1$ and $\theta_0 = 0$. By setting $\rho_n = 0,\ \forall\, n > 20$, we can numerically analyze the resulting truncated system to investigate if oscillations occur when $\mu < 1$.

Figure 16 summarizes the behavior when σ^2 is fixed (in this case to 0.15) while c_{ee} and μ are varied. The oscillatory behavior is organized around 2 codimension-two bifurcations. First, there is a Takens-Bogdanov (TB) bifurcation (labeled (i)) where the curve of Hopf bifurcations (HB, in blue) meets with the left-hand curve of fold bifurcations (red). Emerging from the TB is a curve of homoclinic bifurcations (in green) that terminates on the right fold (red/purple) at point labeled (ii). This is called a *non-central saddle-node homoclinic* [50] or a *saddle-node loop* [51]; we will abbreviate it DH (degenerate homoclinic) for simplicity. In the upper part of the right-hand fold, above the DH there is a transition to periodic orbits via a saddle-node infinite cycle bifurcation (SNIC) and below the DH, oscillations continue from the branch that emanates from the HB. There is a cusp (labeled (iii)), however, this plays no role in the oscillations. Oscillations are found in regions C, E and F. The number of fixed points and their stabilities are shown in the schematic Figure 17. In region A, there is a single globally stable fixed point; in B, there are two stable fixed points that are separated by a saddle-point; in C, there is bistability between a stable fixed point and a small amplitude limit cycle which arises due to the Hopf bifurcation bordering region B. In region D, there is a single stable fixed point and two unstable fixed points. Region E contains oscillations and is reached from D via a SNIC bifurcation, from C via a fold, and from A via a HB. Above region E is region F, where there are still oscillations, although these oscillations are slightly different and pertain to the winding number (see Fig. 18). If one were to look at the system

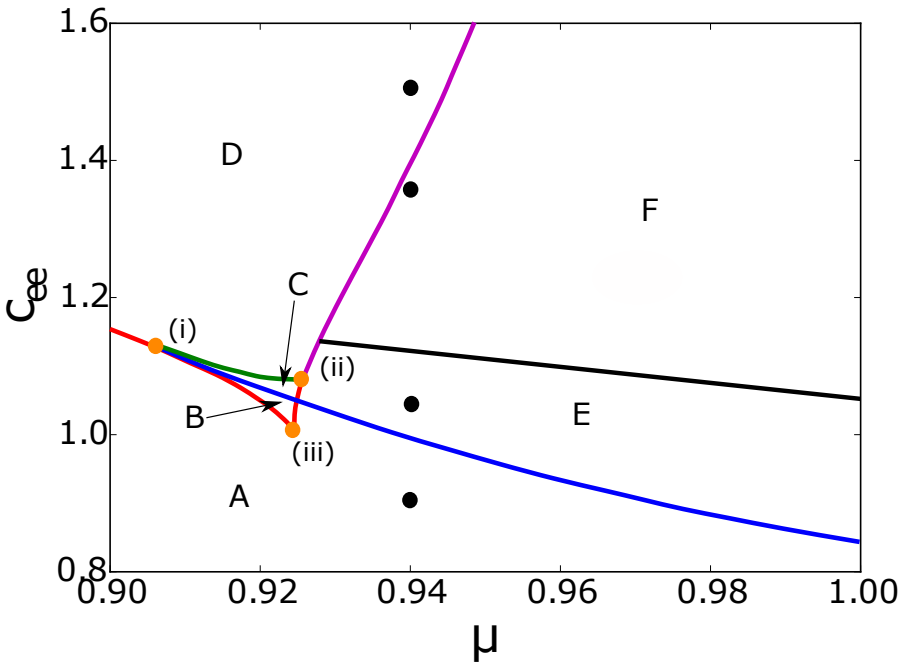

Figure 16: Two-parameter diagram for system (14) with $\sigma^2 = 0.15$. In region A, there is a single stable fixed point. As c_{ee} increases into region B, a stable and an unstable fixed point are formed. The blue line is a Hopf bifurcation and limit cycles emerge in region C. As c_{ee} continues to increase, the limit cycle undergoes a homoclinic bifurcation and vanishes in D. In E, there are also limit cycles; however, opposed to C, these are globally stable. From E to D, there is a SNIC bifurcation and region D contains three fixed points, similar to B. Lastly, region F also contains oscillations, see Fig. 18 for more information. The four black dots correspond to the points taken for Fig. 19.

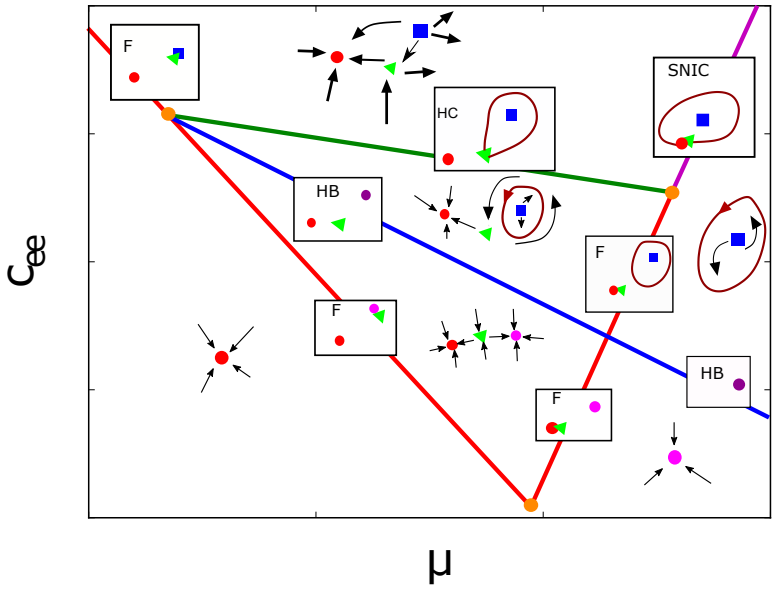

Figure 17: Schematic of the dynamics and transitions of the noisy excitable system overlayed on a zoomed-in simplified version of Figure 16, excluding region F. Filled circles (resp. triangles, squares) are fixed points with no unstable modes (resp. 1, 2). Boxes indicate bifurcations: F, fold; HC, homoclinic; HB, Hopf bifurcation; SNIC, saddle-node infinite cycle.

in Cartesian coordinates instead of polar coordinates, there would be no bifurcation between region E and region F.

Figure 19 shows the behavior of Eq. (12) for $N = 4000$ cells, $\mu = 0.94$ and $\sigma^2 = 0.15$ for different values of c_{ee}. We will denote the Kuramoto order parameter by OP, given as

$$\text{OP} = \frac{1}{N}\left|\sum_{j=1}^{N} e^{iu_j}\right|$$

which is known to be a good measure of synchronization (see [40]). In Fig. 19, we also plot OP for different values of c_{ee}, shown by the dots in Fig. 16. Taking $c_{ee} = 0.90$, we are in region A, far from the HB and the OP shows noisy deviations around a stable fixed point; $c_{ee} = 1.04$ is above the HB curve in region E and shows high frequency noisy oscillations; $c_{ee} = 1.35$ is in region F and we can see the cells are traversing all angles 0 to 2π, and this point is close to the SNIC curve and shows clear low frequency oscillations; $c_{ee} = 1.5$ is in region D and again shows nearly constant behavior (stable fixed point) where most cells are pinned near a fixed point. The raster plots show the associated behavior of all 4000 cells for each of these four values of c_{ee}. We note that the fixed point cases with the lowest and highest coupling are qualitatively different; this can be seen in the rasters. In the case of weaker coupling ($c_{ee} = 0.9$), the dynamics are dominated by the noise and each cell fires nearly independently; the result is very asynchronous behavior and a low order parameter (near 0.8). With strong coupling ($c_{ee} = 1.5$), the cells are mainly pinned to the mean phase, $\bar{\theta}$, satisfying $\bar{\theta} = 2\pi - \cos^{-1}(\bar{\mu})$. In this case, the order parameter is high (roughly 0.95) but there are no oscillations; the cells are "synchronized" at the rest state.

The OP is nothing more than the amplitude of the first Fourier component of the density, $F(t, u)$, so that oscillations in the OP imply oscillations in the density. As can be seen from the rasters, oscillations in F correspond to synchronous firing of the excitable cells (shown in the rasters as times in which the units pass through π). To better illustrate the dynamics of individual cells in the different regimes, we compute the probability that a cell is at $u = \pi$:

$$F(t, \pi) = 1 + 2\sum_{n=1}^{\infty}(-1)^n r_n,$$

and plot it in Fig. 20 for the four regimes shown in Fig. 19. This allows us to distinguish whether the macroscopic oscillations correspond to synchronous groups of cells firing (going

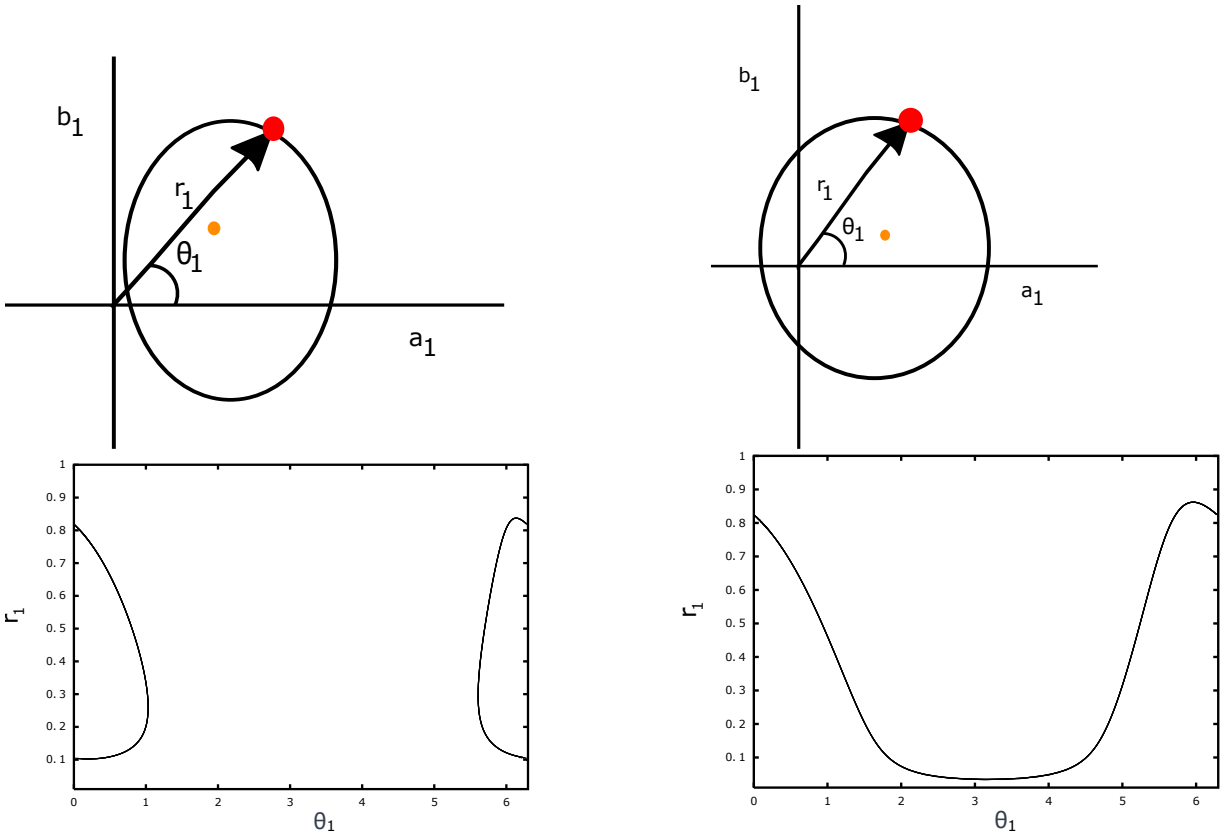

Figure 18: The top left figure is a schematic diagram with parameters in region E, shown in the complex plane. The red dot represents the value of (a_1, b_1) and this point rotates around the circle as time increases. The black arrow is the vector from the origin to this red point. As the red dot rotates around the limit cycle, the arrow moves as well, changing its magnitude and its direction. The bottom left figure shows the magnitude and direction of the arrow as the red dot rotates around the limit cycle. Fixing μ, as c_{ee} increases, we enter region F, whose schematic is shown in the top right picture. Now the limit cycle contains the origin and because of this, the black arrow rotates around the entire complex plane, as can be seen in the bottom right figure. We can see from the top figures that no bifurcation appears to occur; the limit cycle is simply getting larger as the unstable fixed point (shown in orange) changes. However, from the bottom two figures, one might say that there is a bifurcation occurring between region E and region F. In reality, there is merely a difference in the winding number. Region E has limit cycles with winding number 0 and region F has limit cycles with winding number 1.

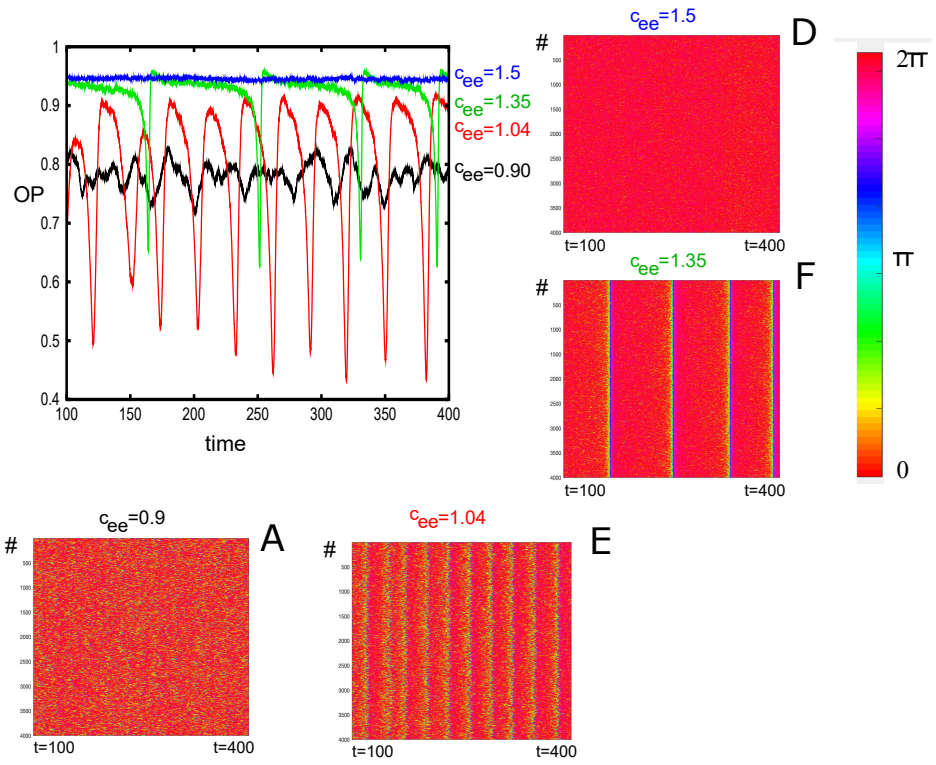

Figure 19: Dynamics of the finite system ($N = 4000$) of coupled excitable cells using Eq. (12) for $\mu = 0.94$, $\sigma^2 = 0.15$, and different values of coupling strength, c_{ee}. The Kuramoto order parameter, OP $= (1/N)\left|\sum_j \exp(iu_j)\right|$ is plotted. Raster plots for each of the 4000 cells are also plotted at the different values of c_{ee} and are labeled by the regions A, E, F, D in Figure 16. These rasters correspond to the black dots shown in that figure.

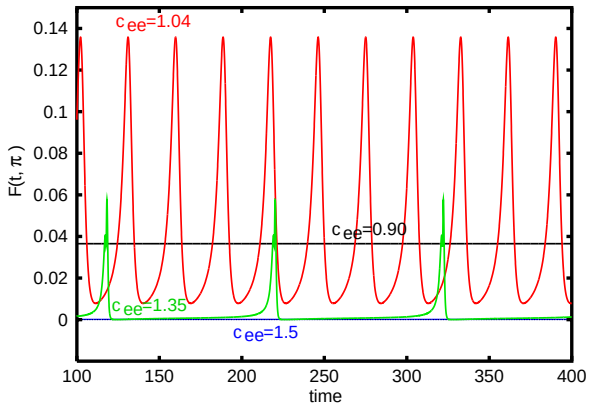

Figure 20: The probability that an oscillator is at $u = \pi$ as a function of time for the same parameters as in Fig. 19. One can see qualitatively how the fixed points differ for c_{ee} small and c_{ee} large as well as how $F(t, \pi)$ changes when there are oscillations.

through a complete cycle in phase space) rather than groups of cells making small oscillations around their fixed points. We see from the figure that at low coupling values, $c_{ee} = 0.90$, there is a nonzero probability that any given cell crosses π but these crossings are asynchronous with no macroscopic rhythm. For the two intermediate coupling strengths, $c_{ee} = 1.04, 1.35$, the probability of crossing π varies in time and is periodic with high peaks in F. We note that at the stronger coupling value, the probability of a cell being at π is close to zero for a long stretch of time with brief bouts where the cells fire. This is evident from the raster plots in Fig. 19 for $c_{ee} = 1.35$. Finally, at the large coupling strength, $c_{ee} = 1.5$, there are no synchronous firings and the cells are pinned near rest; the probability of any cell being at π is very close to zero. In the remainder of the chapter, we will use the order parameter as a surrogate for macroscopic oscillations rather than $F(t, \pi)$, mainly because it will turn out to be a key variable in the reduction of the network to a low dimensional system.

Fig. 16 remains qualitatively the same as we change the level of noise; this is shown in Fig. 21 where we vary the value of σ^2. As the noise decreases, the cusp point (intersection of the two red curves) appears to limit to $\mu = 1$.

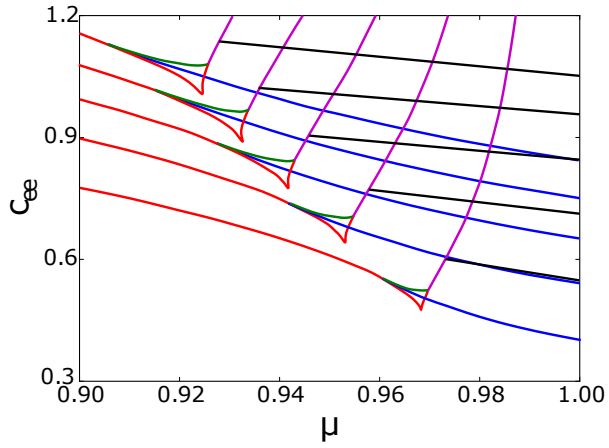

Figure 21: Two-parameter diagram for Eq. (14) with different noise levels. From top to bottom, the lines touching the c_{ee}-axis correspond to $\sigma^2 = \{0.15, 0.12, 0.09, 0.06, 0.03\}$. As the noise goes to zero, region C shrinks and the cusp appears to approach $\mu = 1$. We find this to be a common trend for the other systems later in the chapter.

3.2.1.1 FPE truncation

We have approximated the solutions to Eq. (13) by a finite number of mode equations by setting all modes to zero above $n = 20$. This is a very simple form of moment closure as one can interpret ρ_n as the expected value of e^{-inu} (the n^{th} circular moment). A few natural questions arise: (1) did we use enough modes? (2) If so, how few are enough to capture the primary dynamics (e.g. the cusp and the TB point)? (3) Are there better ways to truncate the equations?

To answer the first question, we consider a different way to approximate Eq. (13); we discretize the PDE using centered differences and compute the bifurcation equations for the resulting system of ODEs. Fig. 22A shows a comparison between the 20 mode truncation (used in this section) and the discretization of the PDE, wherein we discretized the PDE into 100 bins. The two plots overlap almost perfectly. This shows that our truncation to 20 modes is not too little at least at the level of noise used in this example ($\sigma^2 = 0.15$).

Let us consider questions 2 and 3. Sakaguchi [25] needed 4 modes to obtain the TB

bifurcation using the simple moment closure that $\rho_k = 0$ for $k > M$. This leads to 8 real ODEs. Suppose that we consider just modes 1 and 2. The equation for ρ_2 involves ρ_3 so we need to express ρ_3 in terms of ρ_1, ρ_2. The simplest truncation is to just set $\rho_3 = 0$. We have found that this approximation does not work very well and often leads to unbounded behavior, so this is not discussed further. The approximation $\rho_3 = \rho_1^3$ motivated by the so-called Ott-Antonsen ansatz (see Section 3.2.2, following) gives the cusp bifurcation and the TB but also has period doubling regimes, other fold bifurcations, other Hopf bifurcations and unbounded areas as well (computations not shown). Recently [45] have suggested that using cumulants rather than moments gives better results. Thus, we will give a brief introduction to cumulants. Define the moment generating function for ρ_n as

$$G(k,t) = \sum_{n=0}^{\infty} \rho_n(t) \frac{k^n}{n!},$$

with $\rho_0 = 1$. Then the cumulants are defined by

$$\Psi(k,t) = k\frac{\partial}{\partial k} \ln\Big(G(k,t)\Big) = \frac{k}{G}\frac{\partial G}{\partial k} = \sum_{n=1}^{\infty} \chi_n(t) k^n.$$

Using the last equality, we can say

$$\sum_{n=0}^{\infty} \rho_{n+1} \frac{k^{n+1}}{n!} = \left(\sum_{n=0}^{\infty} \rho_n \frac{k^n}{n!}\right)\left(\sum_{n=1}^{\infty} \chi_n k^n\right).$$

Thus, cumulants can be obtained recursively through

$$\chi_1 = \rho_1\,, \qquad \chi_n = \frac{\rho_n}{(n-1)!} - \sum_{m=1}^{n-1} \frac{\chi_m \rho_{n-m}}{(n-m)!}\;, \quad n > 1$$

or for an explicit formula, one may use incomplete Bell polynomials. For completeness, we list the first few cumulants:

$$\chi_1 = \rho_1 \quad \chi_2 = \rho_2 - \rho_1^2 \qquad \chi_3 = \frac{1}{2}\big(\rho_3 - 3\rho_2\rho_1 + 2\rho_1^3\big).$$

In the standard Ott-Antonsen model, shown later, $\chi_n = 0,\ \forall\, n > 1$ or equivalently, $\rho_n = \rho_1^n$. Here we will assume $\chi_n = 0,\ \forall\, n > 2$, meaning $\rho_3 = 3\rho_2\rho_1 - 2\rho_1^3$. This provides a more

accurate model on the order of $\mathcal{O}(\sigma^4)$ (see [45]). If we do this, our first two mode equations become

$$\begin{aligned}
\dot{\rho}_1 &= i\mu\rho_1 - \frac{i}{2}\big(1+\rho_2\big) - \frac{c_{ee}}{2}\big(\rho_1^*\rho_2 - \rho_1\big) - \sigma^2\rho_1 \\
\dot{\rho}_2 &= 2i\mu\rho_2 - i\rho_1\big(1+3\rho_2-2\rho_1^2\big) - c_{ee}\rho_1\big(3\rho_2\rho_1^* - 2\rho_1^2\rho_1^* - \rho_1\big) - 4\sigma^2\rho_2.
\end{aligned} \tag{15}$$

Letting $\rho_1(t) = r(t)e^{i\theta(t)}$ and $\rho_2(t) = s(t)e^{i\phi(t)}$, we find

$$\begin{aligned}
\dot{r} &= -\sigma^2 r - \frac{1}{2}\Big(\sin(\theta) - c_{ee}r\Big) + \frac{s}{2}\Big(\sin(\phi-\theta) - c_{ee}r\cos(\phi-2\theta)\Big) \\
\dot{\theta} &= \mu - \frac{1}{2r}\Big(\cos(\theta) + s\cos(\phi-\theta)\Big) - \frac{c_{ee}s}{2}\sin(\phi-2\theta) \\
\dot{s} &= -4\sigma^2 s + 3rs\Big(\sin(\theta) - c_{ee}r\Big) + r\Big(\sin(\theta-\phi) - 2r^2\sin(3\theta-\phi)\Big) + \\
&\qquad\qquad c_{ee}r^2(1+2r^2)\cos(2\theta-\phi) \\
\dot{\phi} &= 2\mu - \frac{r}{s}\Big(\cos(\theta-\phi) + 3s\cos(\theta) - 2r^2\cos(3\theta-\phi)\Big) + \frac{c_{ee}r^2}{s}(1+2r^2)\sin(2\theta-\phi).
\end{aligned} \tag{16}$$

Figure 22B shows the two-parameter bifurcation structure for the cumulant approximation along with that of the 20 mode truncation for $\sigma^2 = 0.15$. The two plots are qualitatively similar with the same cusp, TB, and homoclinic structures. The difference is seen mostly in the shape of the curves of Hopf bifurcation as the noise decreases; in the cumulant model, they tend to curve quite a bit to the left before terminating at their TB points. Figure 23 goes on to show this and it should be compared to Fig. 21; qualitatively the pictures are the same with a TB, cusp, and DH all occurring at each noise level.

One can also look at these models by fixing the excitability μ and plotting σ^2 with c_{ee}. We show this in Fig 24. With fixed excitability, one can see there is a cone-shaped region where the right values of σ^2 and c_{ee} will give rise to macroscopic oscillations. In this section, we have shown that there is a particular dynamical structure to systems of coupled excitable cells driven by Gaussian noise. In the next several sections, we show that this is a universal phenomenon and does not depend on the nature of the noise.

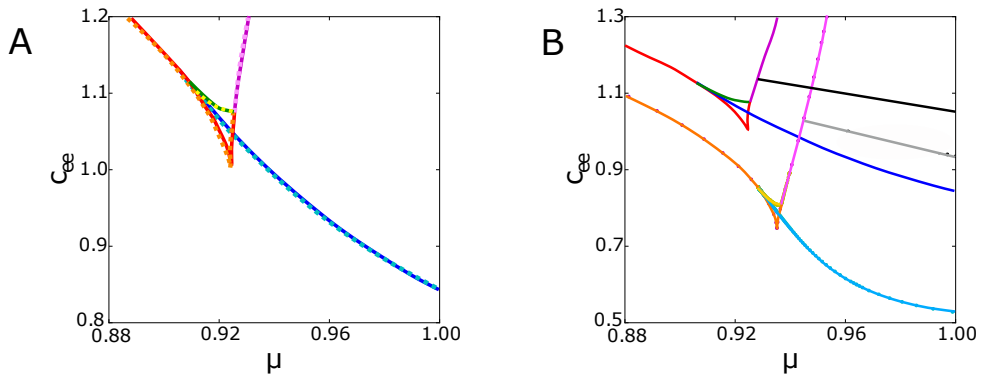

Figure 22: Two parameter diagram for two approximations of Eq. (13) with $\sigma^2 = 0.15$. (A) Comparison between the 20 mode truncation (Eq. (14)) and the discretization of the FPE (Eq. (13)) into 100 bins, which are given square markers and are lighter colored. There is no discernible difference. (B) Comparison of the 20 mode truncation and the 2 mode truncation with cumulant closure. The cumulant closure model has curves in lighter colors and the 20-mode truncation is higher on the c_{ee}-axis with darker colors.

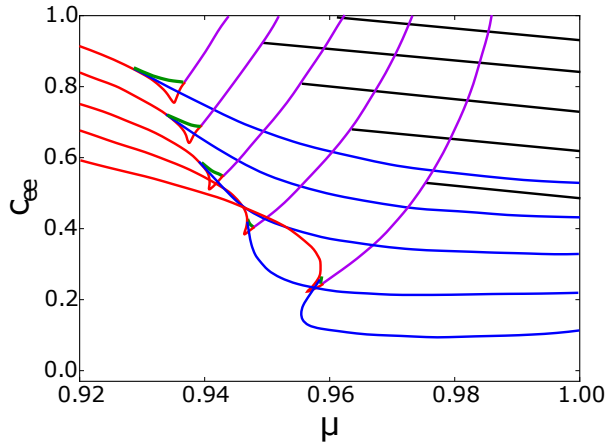

Figure 23: Two parameter diagram for the cumulant closure with different noise levels, $\sigma^2 = \{0.15, 0.12, 0.09, 0.06, 0.03\}$. Compare this to Fig. 21. One strange difference is when the noise goes to zero, the HB curve becomes more eccentric and begins at the TB by going back in μ then dipping to a minimum before leaving at $\mu = 1$.

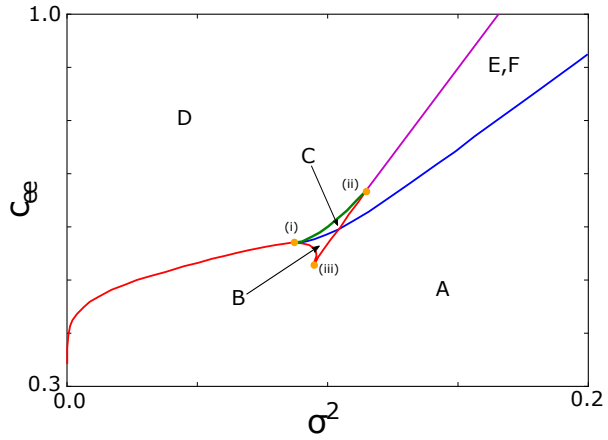

Figure 24: Two parameter diagram for the cumulant closure with fixed excitability $\mu = 0.94$. The regions are the same as in Figure 16 and regions E and F have been merged as the difference is unnecessary here. If there is a higher noise level, there must be a higher coupling strength in order for oscillations to form.

3.2.2 Ott-Antonsen ansatz

We obtained Fig. 16 by approximating the solutions to the Fokker-Planck equation (13) and then analyzing the dynamics of a finite number of Fourier modes. We also looked at a low-dimensional truncation and found qualitatively similar behavior. However, if instead of Gaussian noise, we consider frozen or heterogeneous noise (that is, the noise is taken from some distribution but is constant in time), then it is possible to write down an equation for the Fourier modes which can be low dimensional for certain choices of distributions by utilizing the *Ott-Antonsen ansatz*. We now describe this procedure.

Consider a globally coupled population of excitable cells u_j, given by

$$\dot{u_j} = \omega_j - \cos(u_j) + \frac{c_{ee}}{N} \sum_{l=1}^{N} \sin(u_l - u_j) \tag{17}$$

where ω_j is taken from a distribution with density function $g(\omega)$. Our goal is to study the behavior of these cells as $N \to \infty$. An approach is to use mean field theory (MFT) and define the complex order parameter

$$z(t) = \lim_{N\to\infty} \frac{1}{N} \sum_{j=1}^{N} e^{iu_j}.$$

With this, we can look at the asymptotic behavior of $z(t)$ to study the asymptotic behavior of our original system as they will coincide with each other (note that in section 3.2.1, OP $= |z|$). Developing a differential equation for $z(t)$ will greatly reduce the dimension of our system as well. As in Eq. (13), we can write down an equation for the probability density function, $F(u, \omega, t)$, which gives the density at time t of phase u that has fixed frequency ω:

$$\frac{\partial F}{\partial t} + \frac{\partial}{\partial u}\big(F(u, \omega, t)\dot{u}\big) = 0 \tag{18}$$

where

$$\dot{u} = \omega - \frac{1}{2}e^{iu} - \frac{1}{2}e^{-iu} + \frac{c_{ee}}{2i} z e^{-iu} - \frac{c_{ee}}{2i}\overline{z}e^{iu}$$

and

$$z(t) = \int_0^{2\pi} \int_{-\infty}^{\infty} F(u, \xi, t) e^{iu}\, d\xi\, du. \tag{19}$$

To get the $\dot{u}$ equation, we have used the fact that

$$\lim_{N\to\infty} \frac{1}{N} \sum_{j=1}^{N} \sin(u - u_j) = \int_0^{2\pi} \int_{-\infty}^{\infty} \sin(u - v) F(v, \omega, t)\; d\omega\; dv,$$

written $\sin(u)$ in terms of complex exponentials, and used Eq. (19). Since F is periodic in u and the density of the uncoupled frequencies is known, we write

$$F(u, \omega, t) = \frac{g(\omega)}{2\pi}\Big(1 + \sum_{n=1}^{\infty} \alpha_n(\omega, t) e^{-inu} + \overline{\alpha}_n(\omega, t) e^{inu}\Big). \tag{20}$$

Because $\dot{u}$ contains only terms in $e^{\pm iu}$, there is an attracting manifold [38] on which $\alpha_n(\omega, t) = \alpha_1(\omega, t)^n \equiv \alpha(\omega, t)^n$. This assumption on the Fourier coefficients is called the *Ott-Antonsen ansatz* and we will be exploiting it now through most of this chapter. One sees immediately that

$$z(t) = \int_{-\infty}^{\infty} \alpha(\omega, t) g(\omega)\, d\omega \tag{21}$$

so we only need a differential equation for $\alpha(\omega, t)$. Using Eqs (18) and (20) and grouping coefficients of e^{-iu}, we arrive at

$$\frac{\partial \alpha}{\partial t} - i\omega\alpha + \frac{i}{2} + \frac{i}{2}\alpha^2 + \frac{c_{ee}}{2}\alpha^2\overline{z} - \frac{c_{ee}}{2} z = 0. \tag{22}$$

Note that we have reduced the continuity PDE to an infinite set of ordinary differential equations for $\alpha(\omega, t)$, indexed by $\omega \in \mathbb{C}$, that are coupled via the term (21). However, if the density $g(\omega)$ has poles in the complex plane, then we can often compute the integral (21) using residue theory (this was the crucial observation of [38]). We first consider the Cauchy distribution as that results in the simplest mean-field model and then we consider several other densities which lead to richer dynamics that are similar to those in section 3.2.1. So, suppose

$$g(\omega) := g_0(\omega) = \frac{1}{\pi} \frac{\Delta}{(\omega - \mu)^2 + \Delta^2}$$

with $\Delta > 0$ measuring the spread of g_0 and μ is the center of g_0. With this, we can evaluate the integral formula for $z(t)$ using contour integrals and the residue theorem. To stay away from the origin, we must integrate around the upper half of the complex plane. Doing this gives $z(t) = \alpha(\mu + i\Delta, t)$ and plugging this into (22),

$$\dot{z} = (-\Delta + i\mu)z - \frac{i}{2}z^2 - \frac{i}{2} - \frac{c_{ee}}{2}z^2\overline{z} + \frac{c_{ee}}{2}z. \tag{23}$$

Let $z(t) = r(t)e^{i\theta(t)}$ and so

$$\begin{aligned} \dot{r} &= -r\Delta - \frac{1 - r^2}{2}\Big(\sin(\theta) - c_{ee}r\Big) \\ \dot{\theta} &= \mu - \frac{1 + r^2}{2r}\cos(\theta). \end{aligned} \tag{24}$$

Notice if we integrated around the lower half of the complex plane, then the $-r\Delta$ would be replaced by $+r\Delta$ and the magnitude of the order parameter would be larger than 1, which cannot happen by the definition of $z(t)$. Recall that we are interested in whether the combination of noise and coupling is sufficient to drive an excitable network into coherent oscillations. Thus, we are interested in whether or not Eq. (24) has any kind of periodic behavior for $0 < \mu < 1$, which is the excitable regime. For this planar system there are two ways that oscillations can *emerge*: (1) Hopf bifurcation or (2) drift oscillations via a saddle-node, meaning $\dot{\theta} > 0$ for all time. In what follows, we show that neither of these can occur and more, proving that a Cauchy density cannot produce macroscopic oscillations when the mean μ is in the excitable range.

3.2.2.1 Analysis of eq. (24)

We begin by showing there is a positively invariant region.

Lemma 3.2.1 *If $r_0 \in (0,1)$, then $r(t) \in (0,1)$ for all time.*

Proof. If $r_0 = 1$, $\dot{r} < 0$ so $r(t)$ decreases. Now let $r = \varepsilon s$. Then we have

$$\begin{aligned}\varepsilon \dot{s} &= -\varepsilon s\Delta - \frac{1-\varepsilon^2 s^2}{2}\Big(\sin(\theta) - \varepsilon c_{ee} s\Big)\\ \varepsilon \dot{\theta} &= \varepsilon\mu - \frac{1+\varepsilon^2 s^2}{2s}\cos(\theta).\end{aligned}$$

Rescale time and let $\tau = t/\varepsilon$, so we have

$$\begin{aligned}\frac{ds}{d\tau} &= -\varepsilon s\Delta - \frac{1-\varepsilon^2 s^2}{2}\Big(\sin(\theta) - \varepsilon c_{ee} s\Big)\\ \frac{d\theta}{d\tau} &= \varepsilon\mu - \frac{1+\varepsilon^2 s^2}{2s}\cos(\theta).\end{aligned} \tag{25}$$

To get an understanding of the system, let $\varepsilon = 0$. Thus,

$$\begin{aligned}\frac{ds}{d\tau} &= -\frac{1}{2}\sin(\theta)\\ \frac{d\theta}{d\tau} &= -\frac{1}{2s}\cos(\theta)\end{aligned} \tag{26}$$

and so

$$\frac{ds}{d\theta} = s\tan(\theta) \implies \int \frac{ds}{s} = \int \tan(\theta)\, d\theta \implies \log(s) = -\log(|\cos(\theta)|) + C$$

$$\implies s(\theta) = e^{-\log(|\cos(\theta)|)} e^C = K|\sec(\theta)| = s_0 \left|\frac{\cos(\theta_0)}{\cos(\theta)}\right|$$

assuming $s(\theta_0) = s_0$. This shows that when $s_0 > 0$, s stays positive as long as $\theta \neq \pi/2$ or $3\pi/2$. When $\theta = 3\pi/2$, this is an invariant set where $\dot{s} > 0$ and hence, this angle does not need further investigation. However, when $\theta = \pi/2$, this is an invariant set with $\dot{s} < 0$

and this passes through the line $s = 0$ into the negative s region. However, in the original lemma, we are asserting that $\varepsilon > 0$ strictly and what is happening above is only a limiting case. Our task is to prove that for any initial condition (s_0, θ_0) with $s_0 > 0$, $\exists\, \varepsilon > 0$ such that $s(t) > 0$ for all time. And, by taking the limit as $\varepsilon \to 0$, we have shown that for each initial condition (s_0, θ_0) with $\theta_0 \neq \pi/2$ and $s_0 > 0$, there exists an ε small enough such that s will remain positive for all time. Now we will prove this is also the case for $\theta = \pi/2$. Let $\varepsilon > 0$ and $\theta = \pi/2$:

$$\begin{aligned} \frac{ds}{d\tau} &= -\varepsilon s\Delta - \frac{1-\varepsilon^2 s^2}{2}\Big(1 - \varepsilon c_{ee} s\Big) \\ \frac{d\theta}{d\tau} &= \varepsilon\mu. \end{aligned} \tag{27}$$

Hence, θ will increase away from $\pi/2$ in some infinitesimal time. Since we are also beginning with $s_0 > 0$, s will initially decrease for sufficiently small ε but this will also happen in some infinitesimal time. So s will remain positive. Now, we have a new initial condition (s_1, θ_1) with $\theta_1 > \pi/2$ and $s_1 > 0$. So we can take ε small enough and use the same logic above to show that s will remain positive. So even when $\theta_0 = \pi/2$, we are able to show that s stays positive for all time. □

Now we will prove there are no oscillations for this system. There are three ways for oscillations to exist in this system: one could emerge via a Hopf bifurcation, there could be a drift oscillation or there could be some ambient oscillation surrounding a fixed point that never goes away, that is, it exists for any choice of parameters. The outline of the proof will be as follows: we will first prove there are no Hopf bifurcations for any choice of parameters and then show there can be no drift oscillation for $0 < \mu < 1$. The only remaining option is an ambient oscillation. So, for contradiction, we will suppose there is already an oscillation in our system that never vanishes; this oscillation must exist for any parameters we choose. We will show for one set of parameters, there is only one fixed point in $(r, \theta) \in (0, 1) \times (0, 2\pi)$ and it is stable. Thus, no oscillation exists for this set of parameters which would imply there is no ambient oscillation and so, no oscillations exist for any set of parameters.

Theorem 3.2.2 *$\forall\, c_{ee}, \Delta > 0$, and $0 < \mu < 1$, there is no Hopf bifurcation.*

Proof. Letting $\dot{r} = \dot{\theta} = 0$, we have

$$\cos(\theta) = \frac{2\mu r}{1+r^2} \qquad \sin(\theta) = c_{ee} r - \frac{2\Delta r}{1-r^2}.$$

And so,

$$\left(\frac{2\mu r}{1+r^2}\right)^2 + \left(c_{ee} r - \frac{2\Delta r}{1-r^2}\right)^2 = 1 \tag{28}$$

must be satisfied. The Jacobian matrix is given by

$$J(r,\theta) = \begin{pmatrix} -\Delta - r(c_{ee} r - \sin(\theta)) + \dfrac{c_{ee}}{2}(1-r^2) & -\dfrac{1}{2}(1-r^2)\cos(\theta) \\ \\ \dfrac{1-r^2}{2r^2}\cos(\theta) & \dfrac{1+r^2}{2r}\sin(\theta) \end{pmatrix}$$

and if we evaluate this at the fixed point,

$$J = \begin{pmatrix} -\Delta - \dfrac{2\Delta r^2}{1-r^2} + \dfrac{c_{ee}}{2}(1-r^2) & -\dfrac{\mu r(1-r^2)}{1+r^2} \\ \\ \dfrac{\mu(1-r^2)}{r(1+r^2)} & \dfrac{c_{ee}}{2}(1+r^2) - \dfrac{\Delta(1+r^2)}{1-r^2} \end{pmatrix}.$$

Define the trace of J as $T(r)$ and the determinant as $D(r)$. We see

$$T(r) = c_{ee} - \frac{2\Delta(1+r^2)}{1-r^2}$$

and

$$\begin{aligned} D(r) &= \left(\frac{c_{ee}}{2}(1-r^2) - \frac{\Delta(1+r^2)}{1-r^2}\right)\left(\frac{c_{ee}}{2}(1+r^2) - \frac{\Delta(1+r^2)}{1-r^2}\right) + \left(\frac{\mu r(1-r^2)}{1+r^2}\right)\left(\frac{\mu(1-r^2)}{r(1+r^2)}\right) \\ &= \frac{1}{4}\Big(T(r) - c_{ee} r^2\Big)\Big(T(r) + c_{ee} r^2\Big) + \frac{\mu^2(1-r^2)^2}{(1+r^2)^2}. \end{aligned}$$

We will show that if $T(r) = 0$ then $D(r) < 0$. Setting $T(r) = 0$, the determinant equation and (28) become

$$D(r) = -\frac{1}{4}c_{ee}^2 r^4 + \frac{\mu^2(1-r^2)^2}{(1+r^2)^2}, \qquad 4\mu^2 r^2 + c_{ee}^2 r^6 = (1+r^2)^2$$

respectively. Solving for $c_{ee}^2 r^4/4$ in the second equation and plugging it into the determinant equation, we have

$$D(r) = -\frac{(1+r^2)^2}{4r^2} + \mu^2 + \frac{\mu^2(1-r^2)^2}{(1+r^2)^2} = \frac{2\mu^2(1+r^4)}{(1+r^2)^2} - \frac{(1+r^2)^2}{4r^2}$$
$$= \frac{8\mu^2 r^2(1+r^4) - (1+r^2)^4}{4r^2(1+r^2)^2} = -\left(\frac{8r^2(1+r^4)(1-\mu^2) + (1-r^2)^4}{4r^2(1+r^2)^2}\right) < 0$$

since $0 < \mu < 1$. Thus, there are no Hopf bifurcations. □

Theorem 3.2.3 *$\forall\, \Delta, c_{ee} > 0$, there are no oscillations provided $0 < \mu < 1$.*

Proof. First, notice $\dot{\theta} = 0$ will always have a solution because $\theta = \arccos\left(\frac{2\mu r}{r^2+1}\right)$ is well-defined since $0 < \mu < 1$. So θ cannot travel around the circle completely without hitting a nullcline (i.e., no drift oscillations). And because there is no Hopf bifurcation, the only way for an oscillation to occur is if one has been surrounding a fixed point $\forall\, \Delta, c_{ee} > 0$ and $0 < \mu < 1$. In particular, we can choose c_{ee}, Δ, μ and if there are no oscillations for this particular choice, then there will be no oscillations for any choice. We will begin by showing this system has at least one fixed point. Motivated by Eq (28), define

$$M(r) := \frac{4\mu^2 r^2}{(1+r^2)^2} + r^2\Big(c_{ee} - \frac{2\Delta}{1-r^2}\Big)^2 - 1$$

and notice that the number of solutions to $M(r) = 0$ for $r \in (0,1)$ corresponds to the number of fixed points in this system. We can see $\lim_{r\to 1^+} M(r) = \infty$ and $M(0) = -1$. Since it is clear $M(r)$ is continuous on $(0,1)$, by the intermediate value theorem, there will always be at least one fixed point in our system. If we can find a set of parameters where this is the only fixed point in the system and we can prove this fixed point is stable, then we have found one instance where there are no oscillations in our system. Thus, this would prove there are no oscillations for any choice of parameters. We choose $\mu = 0.5$, $c_{ee} = 1$, and $\Delta = 0.5$. Then a fixed point must satisfy $M_0(r) = 0$ where

$$M_0(r) = \frac{r^2}{(1+r^2)^2} + \frac{r^6}{(1-r^2)^2} - 1.$$

Computing the derivative, one finds

$$M_0'(r) = \frac{2r\big(r^8(1-r^4) + 6r^8 + 4r^6 + 5r^4 + (1-2r^2)^2\big)}{(1-r^4)^3} > 0$$

since $r \in (0,1)$. Thus, there is only one fixed point. Now we must prove it is stable. For these parameters, the trace and determinant are

$$T_0(r) = 1 - \frac{1+r^2}{1-r^2} = \frac{-2r^2}{1-r^2}$$

and

$$D_0(r) = \frac{1}{4}\Big(T_0(r) - r^2\Big)\Big(T_0(r) + r^2\Big) + \frac{(1-r^2)^2}{4(1+r^2)^2},$$

respectively. Obviously $T_0(r) < 0$ and

$$T_0(r) + r^2 = \frac{-r^2(1+r^2)}{1-r^2} < 0$$

which means $D_0(r) > 0$, hence this fixed point is stable. So we have found one case where this system has a stable fixed point and so it cannot have oscillations. So, this concludes the entire proof and shows that there are no oscillations in this system for $c_{ee} > 0, \Delta > 0$ and $0 < \mu < 1$. □

Summary: In this section we have shown that there are no macroscopic oscillations when Eq. (17) is in the excitable regime, coupling is purely sinusoidal, and the frequencies follow the Cauchy distribution. From here, there are two ways that we might vary the model equations. First, we could consider a different class of densities, say, with a faster decay than $1/\omega^2$, since it may be that the "fat tails" in the density create too much noise for oscillations to exist. Another possibility is to change the coupling from $\sin(u)$ to $\sin(u) + b(1-\cos(u))$ which adds some even terms and does not violate the assumptions needed to make the OA

reduction. In the next two sections, we show that either of these assumptions is sufficient to enable macroscopic oscillations when $0 < \mu < 1$.

We add the remark that in the first model (14), if we truncated the model even further to $\rho_2 = \rho_1^2$, we arrive at the system (24) with $\Delta = \sigma^2$. Because of this, it is more sensible to compare Δ to σ^2 instead of σ when looking at future parameter diagrams in the chapter.

3.2.3 Changing $g(\omega)$

We consider two functionally related densities to that of the Cauchy density, both of which decay like $1/\omega^4$ and thus have thinner tails. In both cases, the dimensionality of the system is doubled and the analysis is somewhat limited. Nevertheless, we will be able to show that, with these new densities, the behavior is very similar to that of section 3.2.1. First, consider

$$g(\omega) = g_1(\omega) := \frac{\sqrt{2}}{\pi} \frac{\Delta^3}{(\omega - \mu)^4 + \Delta^4}.$$

Using the residue theorem (see Appendix A.1), we evaluate Eq. (21) as

$$z(t) = \frac{1 - i}{2} r(t) e^{i\theta(t)} + \frac{1 + i}{2} s(t) e^{i\phi(t)},$$

where

$$\begin{aligned}
\dot{r} &= -\frac{\sqrt{2}}{2} r\Delta - \frac{1 - r^2}{2}\Big(\sin(\theta) - \frac{c_{ee}}{2} r - \frac{c_{ee}}{2} s\cos(\phi - \theta) + \frac{c_{ee}}{2} s\sin(\phi - \theta)\Big) \\
\dot{\theta} &= \mu + \frac{\sqrt{2}}{2}\Delta - \frac{1 + r^2}{2r}\Big(\cos(\theta) + \frac{c_{ee}}{2} r - \frac{c_{ee}}{2} s\cos(\phi - \theta) - \frac{c_{ee}}{2} s\sin(\phi - \theta)\Big) \\
\dot{s} &= -\frac{\sqrt{2}}{2} s\Delta - \frac{1 - s^2}{2}\Big(\sin(\phi) - \frac{c_{ee}}{2} s - \frac{c_{ee}}{2} r\cos(\theta - \phi) - \frac{c_{ee}}{2} r\sin(\theta - \phi)\Big) \\
\dot{\phi} &= \mu - \frac{\sqrt{2}}{2}\Delta - \frac{1 + s^2}{2s}\Big(\cos(\phi) - \frac{c_{ee}}{2} s + \frac{c_{ee}}{2} r\cos(\theta - \phi) - \frac{c_{ee}}{2} r\sin(\theta - \phi)\Big).
\end{aligned} \tag{29}$$

Like the Gaussian case in section 3.2.1, for a given level of noise and excitability, the coupling strength has to be in a range that is neither too small (cannot overcome noise) or too large (pinned to the rest state). Fig. 25A shows the two-parameter diagram with μ along the

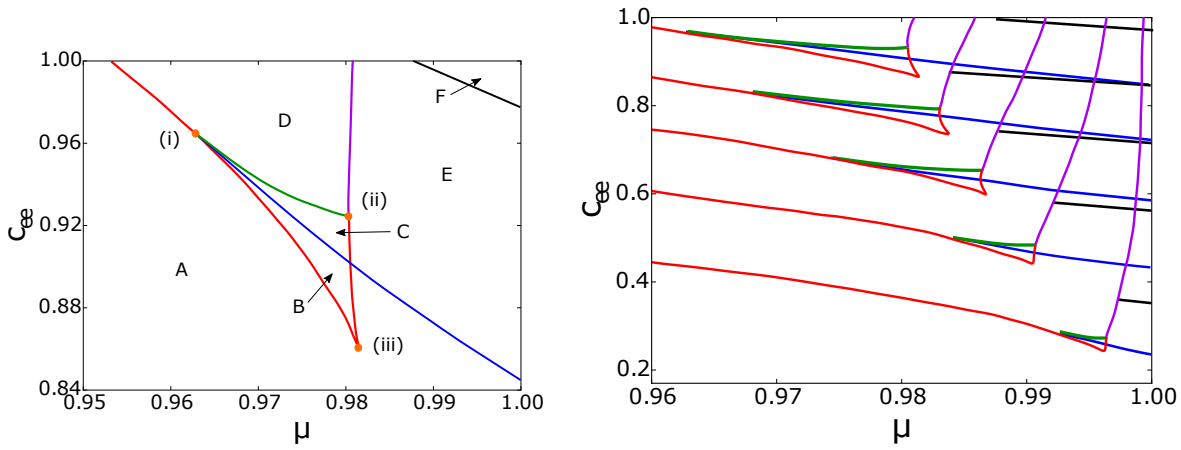

Figure 25: Behavior of Eq. (29) for different values of excitability μ and coupling c_{ee} when $\Delta = 0.27$. Regions and colors as in Fig. 16. In the second figure, from top to bottom, the lines that intersect the c_{ee}-axis correspond to $\Delta = \{0.27, 0.21, 0.15, 0.09, 0.03\}$. Again, as the noise decreases the region between the homoclinic and Hopf lines also decreases.

$x-$axis and the coupling, c_{ee} along the $y-$axis. As with Fig. 16, there are 2 codimension-two bifurcations that separate the dynamics. The behavior in each of these regions is the same as the beginning model, shown in Fig. 17.

In Figure 25B, we decrease the noise and again, as with Fig. 21, the structure of the bifurcation diagram remains. One key feature is as Δ tends to 0, the Takens-Bogdanov and cusp bifurcation appear to join and form a degenerate codimension-three bifurcation, similar to the Gaussian noise. Later, when we perform a rescaling analysis of this system, we will see that, in fact, the two points do remain separated. Similar to the white noise scenario, one can also fix the excitability of the system (see Figure 26). Here, we needed to choose a higher excitability value so we chose $\mu = 0.98$. Again, we see the cone structure comprising of regions E and F. Notice how even though we are fixed at a higher excitability level, one actually needs a higher level of noise and coupling strength to get oscillations.

Lastly, we introduce another tractable density, which appears to have characteristics of

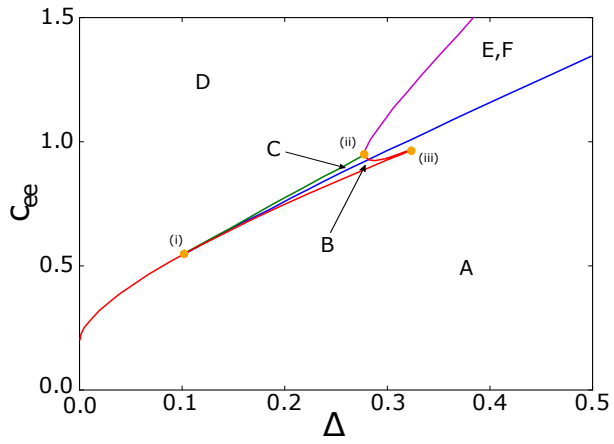

Figure 26: Two parameter diagram for the fourth power density with fixed excitability $\mu = 0.98$. The regions are the same as in Figure 16 and regions E and F have been merged as the difference is again unnecessary here. Similar to Fig 24, if there is a higher noise level, there must be a higher coupling strength in order for oscillations to form.

both our previous densities:

$$g(\omega) = g_2(\omega) := \frac{2}{\pi} \frac{\Delta^3}{\left((\omega - \mu)^2 + \Delta^2\right)^2}.$$

This function has the same decay as $g_1(\omega)$ but also has a more peaked density near $\omega = 0$ like $g_0(\omega)$. Figure 27 shows all three densities; the function $g_1(\omega)$ both decays more quickly and has a more uniform density near $\omega = 0$, thus it is not clear which property of the density allows for synchronization.

Similar to the other densities, we can evaluate equation (21) using the residue theorem albeit with a double pole this time. We obtain the following modified set of polar equations (see Appendix A.2 for details):

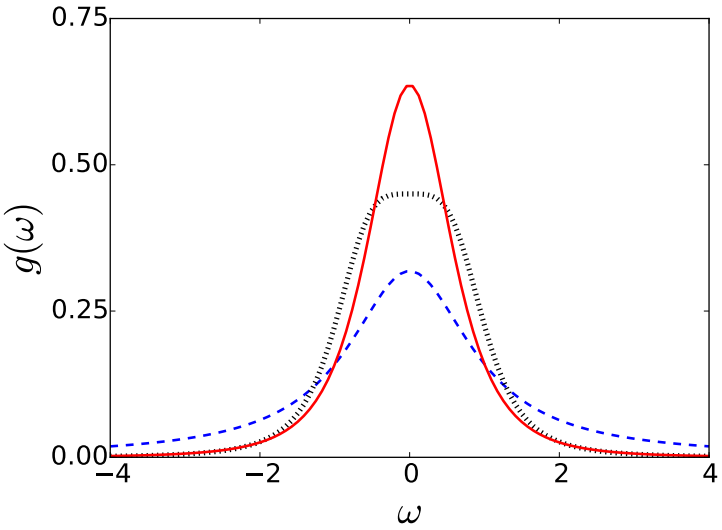

Figure 27: The three densities considered for heterogeneous noise. In these plots, $\mu = 0$ and $\Delta = 1$. The bottom dashed curve is the original Cauchy density $g_0(\omega)$. The middle dotted graph is $g_1(\omega)$, and the top solid graph is $g_2(\omega)$. As one can see, $g_1(\omega)$ is more flat at 0 but its tails have the same behavior as $g_2(\omega)$.

$$
\begin{aligned}
\dot{r} &= -r\Delta - \frac{1-r^2}{2}\Big(\sin(\theta) - c_{ee}s\cos(\phi-\theta)\Big) \\
\dot{\theta} &= \mu - \frac{1+r^2}{2r}\Big(\cos(\theta) - c_{ee}s\sin(\phi-\theta)\Big) \\
\dot{s} &= s(r\sin(\theta)-\Delta) + r(\Delta - c_{ee}s^2)\cos(\theta-\phi) - \frac{r^2}{2}\sin(2\theta-\phi) \\
&\qquad + \frac{c_{ee}}{2}s\big(1+r^2\cos(2\theta-2\phi)\big) - \frac{1}{2}\sin(\phi) \\
\dot{\phi} &= \mu + \frac{r}{s}(\Delta - c_{ee}s^2)\sin(\theta-\phi) - r\cos(\theta) + \frac{r^2}{2s}\cos(2\theta-\phi) \\
&\qquad + \frac{c_{ee}}{2}r^2\sin(2\theta-2\phi) - \frac{1}{2s}\cos(\phi).
\end{aligned}
\tag{30}
$$

We note that $r(t)$ plays a similar role here as in Eq. (24); it is magnitude of $\alpha(\omega, t)$ evaluated at the double pole. Once again, we are also able to find oscillatory solutions for $\mu < 1$ that are robust in c_{ee} and Δ. This system exhibits very similar dynamics to the previous situations. The key difference is region F begins at lower values of c_{ee} in this scenario. Similar to Figs 21 and 25, as the noise decreases, the cusp bifurcation tends towards $\mu = 1$. The main difference between Figs 25 and 28 is that, although these figures show the same noise, the cusp bifurcation occurs for larger μ in the latter.

We conclude this section with a summary of the *coupling* induced transitions of Eqs. (29) and (30) as this has been the emphasis in several papers such as [28, 29, 31]. Consider a point with μ close to 1 (slightly to the right of the cusps in Figs. 25 and 28) and c_{ee} near 0. In this case, there is a single stable fixed point that represents asynchronous behavior (such as seen in Fig. 19, $c_{ee} = 0.90$) where r is small and the oscillators behave independently. As c_{ee} increases, we cross the HB and small amplitude macroscopic oscillations emerge. As c_{ee} increases further, the right fold curves are approached and the oscillation frequency decreases but the amplitude increases. Finally, the fold is crossed (a reverse SNIC bifurcation) and there is a single stable fixed point representing the pinned state (c.f. Fig. 19, $c_{ee} = 1.5$). Thus, as with the Gaussian noise case, variation in the excitability that decays sufficiently fast leads to the ability of an on average excitable system to generate coherent oscillations when the coupling is neither too weak nor too strong.

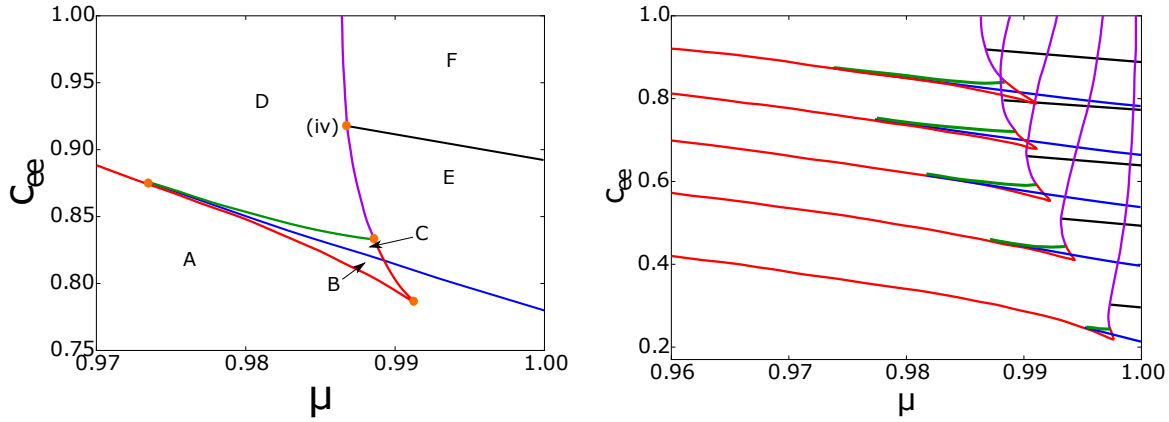

Figure 28: Two-parameter diagram for Eq. (30) at fixed values of Δ. (Left) $\Delta = 0.27$; the lines and regions are exactly comparable to Figs 16 and 25A. One can see the cusp bifurcation occurs for smaller c_{ee} and larger μ than in Fig. 25A. (Right) From top to bottom, the lines touching the c_{ee}-axis correspond to $\Delta = \{0.27, 0.21, 0.15, 0.09, 0.03\}$, the same noise values as Fig. 25B. We also remark that this plot has the same ranges for μ and c_{ee} as in Fig. 25B for easy comparison.

3.2.4 Rescaling analysis

We want to investigate what happens as Δ goes to 0, since it appears the cusp bifurcation and the Takens-Bogdanov bifurcation meet. We show that this is in fact not the case. One can see that as Δ approaches 0 in each model above, r and s approach 1 and θ and ϕ approach 0. Further, from the previous cascading diagrams, c_{ee} approaches 0 and μ approaches 1. Numerical continuation allows us to guess the proper scaling of the phases, amplitudes and parameters as $\Delta \to 0$. Thus, we take $\Delta = \varepsilon^2$ and

$$\begin{aligned} r &= 1 + \varepsilon r_1 + \mathcal{O}(\varepsilon^2) \qquad & s &= 1 + \varepsilon s_1 + \mathcal{O}(\varepsilon^2) \\ \theta &= \varepsilon\theta_1 + \mathcal{O}(\varepsilon^2) \qquad & \phi &= \varepsilon\phi_1 + \mathcal{O}(\varepsilon^2) \\ c_{ee} &= \varepsilon c_1 + \mathcal{O}(\varepsilon^2) \qquad & \mu &= 1 + \varepsilon\mu_1 + \varepsilon^2\mu_2 + \mathcal{O}(\varepsilon^3) \end{aligned}$$

as the perturbations for our other parameters. In both models, we found $\mu_1 = 0$. Plugging these into (29) and grouping orders of ε, we find

$$\begin{aligned} \dot{r_1} &= -\frac{\sqrt{2}}{2} - r_1(c_1 - \theta_1) \\ \dot{\theta_1} &= \mu_2 + \frac{\sqrt{2}}{2} + \frac{1}{2}\theta_1^2 - \frac{1}{2}c_1(r_1 + \theta_1 - s_1 - \phi_1) - \frac{1}{2}r_1^2 \\ \dot{s_1} &= -\frac{\sqrt{2}}{2} - s_1(c_1 - \phi_1) \\ \dot{\phi_1} &= \mu_2 - \frac{\sqrt{2}}{2} + \frac{1}{2}\phi_1^2 - \frac{1}{2}c_1(r_1 - \theta_1 - s_1 + \phi_1) - \frac{1}{2}s_1^2. \end{aligned} \tag{31}$$

Similarly, for (30), the rescaled equations are

$$\begin{aligned} \dot{r_1} &= -r_1(c_1 - \phi_1) - s_1(\phi_1 - \theta_1) \\ \dot{\theta_1} &= \mu_2 - \frac{1}{2}\phi_1^2 + \phi_1\theta_1 - r_1 s_1 + \frac{1}{2}s_1^2 \\ \dot{s_1} &= -1 - s_1(c_1 - \phi_1) \\ \dot{\phi_1} &= \mu_2 + \frac{1}{2}\phi_1^2 - c_1(\phi_1 - \theta_1) - \frac{1}{2}s_1^2. \end{aligned} \tag{32}$$

Figure 29 (left and right) shows the numerical analysis of the rescaled equations respectively. We can now clearly see that the cusp and the Takens-Bogdanov points remain well-separated as $\Delta \to 0$ and there is no codimension-three bifurcation. .

3.2.5 Changing the coupling

In the previous section, we considered purely sinusoidal coupling between the excitable units, that is, calling $H(\phi)$ the coupling function, we let $H(\phi) = \sin(\phi)$. The coupling function should, in general, satisfy $H(\phi + 2\pi) = H(\phi)$ as the phase space is the circle. Secondly, we assume $H(0) = 0$ since if $H(0)$ is non-zero, we can incorporate this into the parameter μ. Finally, we want $H'(0) > 0$ since we want to encourage synchronization. A single odd Fourier mode (e.g. $\sin(\phi)$) can accomplish this. However, in many other studies, the appearance of an even term in the coupling function can have strong qualitative effects on the dynamics ([52, 53, 54]). So, we add a simple even term to the coupling function such that the above constraints hold and further, one for which the OA ansatz can still apply. Hence, we now consider the case where $H(\phi) = \sin\phi + b(1 - \cos\phi)$:

$$\dot{u}_i = \omega_i - \cos(u_i) + \frac{c_{ee}}{N}\sum_{j=1}^{N}\Big(\sin(u_j - u_i) + b\big(1 - \cos(u_j - u_i)\big)\Big)$$

where b is an extra parameter. We remark that this is equivalent to taking $H(\phi) = \sin(\phi + \gamma) - \sin(\gamma)$. Letting $N \to \infty$ and applying the OA reduction with the Cauchy distribution, we arrive at

$$\begin{aligned}\dot{r} &= -r\Delta - \frac{1-r^2}{2}\Big(\sin(\theta) - c_{ee}r\Big)\\ \dot{\theta} &= \mu + \frac{c_{ee}b}{2}(1-r^2) - \frac{1+r^2}{2r}\cos(\theta).\end{aligned} \tag{33}$$

We use the Cauchy distribution because, with purely sinusoidal coupling, the Cauchy distribution model had no oscillations. However, for $b > 0$, there indeed are oscillations in this system as can be seen in Fig. 30 where we have set $b = 0.5$. The two parameter diagram

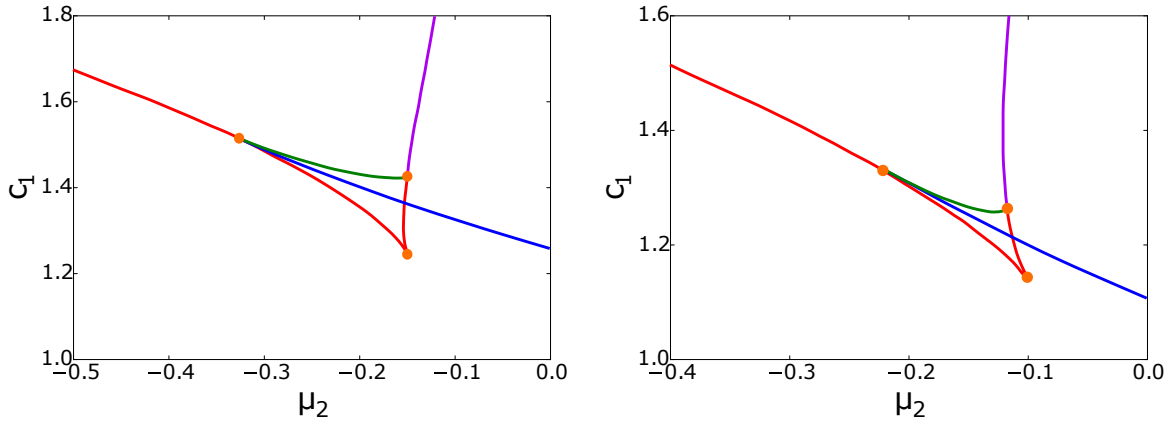

Figure 29: Two-parameter diagram with the rescaled equations, (31) on the left and (32) on the right. The lines and regions are exactly comparable to Figure 16. One can see $\mu_2 < 0$ which makes sense because μ is approaching 1 from below. In the right-hand system, the equations turn out so nicely that one can actually prove the Takens-Bogdanov point occurs at $(\mu_2, c_1) = (-2/9, 4/3)$ and at the TB, one has $(r_1, \theta_1, s_1, \phi_1) = (-1/2, 5/6, -1, 1/3)$. We show this in Appendix A.3.

is essentially identical to the ones that we have previously encountered with oscillations between the blue and green curves and to the right of the purple curve and above the blue curve.

Next, as in the previous cases, we can do a rescaling analysis in the limit as $\Delta \to 0$ for non-zero b to see if the TB point and cusp point meet. Again, we have $\Delta = \varepsilon^2$ and

$$r = 1 + \varepsilon r_1 + \mathcal{O}(\varepsilon^2) \qquad \theta = \varepsilon\theta_1 + \mathcal{O}(\varepsilon^2)$$
$$c_{ee} = \varepsilon c_1 + \mathcal{O}(\varepsilon^2) \qquad \mu = 1 + \varepsilon^2\mu_2 + \mathcal{O}(\varepsilon^3)$$

and so the rescaled equations become

$$\begin{aligned} \dot{r_1} &= -1 - r_1(c_1 - \theta_1) \\ \dot{\theta_1} &= \mu_2 + \frac{1}{2}\theta_1^2 - bc_1r_1 - \frac{1}{2}r_1^2. \end{aligned} \tag{34}$$

We now have a simple planar quadratic system whose behavior is much easier to analyze than Eq. (33). Indeed, we can find both the Takens-Bogdanov point, (μ_{TB}, c_{TB}), and the cusp point, (μ_{cusp}, c_{cusp}), for this system. For notational simplicity, we drop the subscripts in (34). The Jacobian matrix at an equilibrium point is

$$J(r,\theta) = \begin{pmatrix} \theta - c & r \\ \\ -r - bc & \theta \end{pmatrix}.$$

For a Hopf bifurcation, it is necessary that the trace vanish and the determinant be positive. The trace vanishes when $\theta = c/2$ which implies $r = -2/c$ from $\dot{r} = 0$. Setting $\dot{\theta} = 0$ and solving for μ we have

$$\mu_H = \frac{16 - c^4 - 16bc^2}{8c^2}.$$

Furthermore, the determinant,

$$D_H = \frac{16 - c^4 - 8bc^2}{4c^2}$$

must be positive. Since, we want to be in the excitable range where $\mu_H < 0$, we require that $b > 0$. One would have to compute the normal form coefficients to determine if this

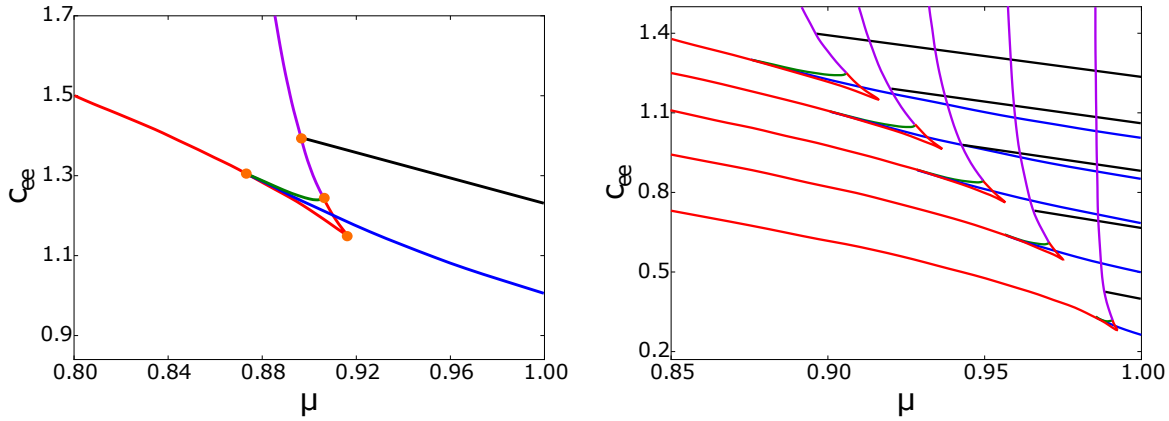

Figure 30: On the left is the bifurcation diagram for system (33) with $b = 0.5$ and $\Delta = 0.27$. We see the same regions as in Figure 25A. On the right is the cascade diagram for system (33) with $b = 0.5$. From top to bottom, the lines touching the c_{ee}-axis correspond to $\Delta = \{0.27, 0.21, 0.15, 0.09, 0.03\}$, just as the other figures. Again, as the noise decreases, the homoclinic and Hopf bifurcation line get closer to each other. One difference is for fixed Δ, c_{ee} is larger and μ is smaller than the previous cascades.

was a generic Hopf bifurcation; we will not do that calculation. Numerically, the bifurcation appears to be supercritical. To find the TB point, we set $D_H = 0$ and thus obtain

$$\mu_{TB}(b) = -b, \qquad c_{TB}(b) = 2\sqrt{-b + \sqrt{b^2+1}}$$

or

$$c_{TB}(\mu) = 2\sqrt{\mu + \sqrt{\mu^2+1}}.$$

Since $\mu_{TB}(b) = -b$, the TB point occurs in the excitable range when $b > 0$ and so, for low noise, there will always be oscillations for $b > 0$. Unfortunately, we were not able to find the fold and Hopf bifurcations for fixed b, however, with some algebra, we can find the curve of cusp bifurcations given below:

$$c_{cusp}(\mu) = \sqrt{2\left(D + \sqrt{\frac{(2\mu - D)\big((D+\mu)^2+9\big)}{D}}\right)},$$

where

$$D = D(\mu) = \operatorname{sgn}(\mu)\sqrt{\mu^2 - 3 + 3(1+\mu^2)^{2/3}}.$$

The derivation of this cusp curve as well as some algebraic facts are given in Appendix A.4. Notice c_{cusp} is in terms of μ; we weren't able to solve for μ_{cusp} and c_{cusp} in terms of b specifically. The bifurcation diagrams for different values of b are plotted in Figure 31 as well as the dotted black curves that represent the curve of cusps and TB points. We can clearly see that for any $b > 0$, the cusp and TB points are well-separated. As a final remark, we note that we derived equations similar to Eqs. (29) and (30) for the case when $b \neq 0$. We have found no qualitative differences from the $b = 0$ case and suspect oscillation regimes remain robust for any $b \in \mathbb{R}$, even for b large and negative. In conclusion, we have shown that by either changing the form of the coupling or the decay of the heterogeneity, we are able to obtain oscillatory behavior in globally coupled excitable cells when the coupling and noise lie within a certain range.

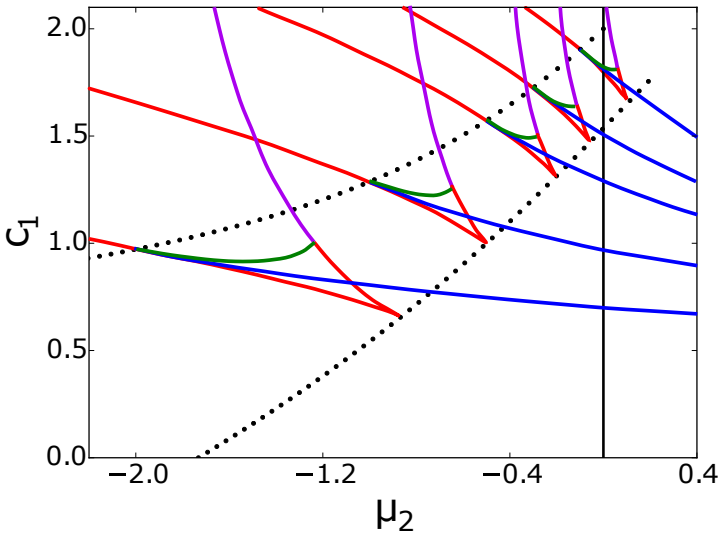

Figure 31: The figure shows the bifurcation diagram for system (34) with different values of b. From top-right to bottom-left, the clusters of graphs correspond to $b = \{0.1, 0.3, 0.5, 1.0, 2.0\}$. We also have plotted the curve of TB curves and cusp curves for $b \geq 0$. The curves clearly show that the TB point and cusp point remain well-separated as the noise tends to zero. When $b = 0$, the TB curve begins at $(\mu_2, c_1) = (0, 2)$ and the cusp curve begins in the excitable range at $(\mu_2, c_1) = \left(3^{-3/2}, 4(3^{-3/4})\right)$. As b increases, the TB and cusp points move to the left and down, with the TB point continuing off to $(-\infty, 0)$ and the cusp point getting infinitesimally close to $(-\sqrt{3}, 0)$.

3.3 Discussion

In this chapter, we described a number of paths to synchronous oscillations in a globally coupled network of excitable elements that were driven either by Gaussian noise or by heterogeneous noise. There were essentially three parameters of interest: the mean degree of excitability μ, the coupling strength c_{ee}, and the strength of the noise Δ or σ^2. When a cell is in the excitable regime, noise is required to drive it to fire and coupling is necessary to drive others to fire. If the noise and coupling are in right region, then macroscopic oscillations emerge as seen in Fig. 19. In order to better understand this phenomenon, we let the number of cells grow to infinity and described a series of mean-field models. For Gaussian noise, we derived a Fokker-Planck equation and from this arose a finite set of equations for the Fourier modes. We showed that macroscopic oscillations existed and were organized around 2 codimension-two bifurcations: the Takens-Bogdanov (TB) and the non-central saddle-node homoclinic (DH). We also considered a highly reduced version of our first model that considered only the first two Fourier modes and used a recently devised moment-closure assumption. This system also had the same dynamics and transitions as the coupling and excitability varied. We remark that this moment-closure result [45] could also have heterogeneous noise and this could be explored more but we don't expect the qualitative behavior to change.

In the case of heterogeneous noise, where parameters are taken from a distribution, there is an exact mean-field reduction and we explored the behavior, first with the Cauchy distribution (section 3.2.2), and then with some different distributions whose tails decayed faster. In the former case, we obtained a planar dynamical system with the order parameter and its phase angle and showed that there are no macroscopic oscillations possible. However, with the other two distributions, the fourth power and the double root, we were able to find oscillations and had essentially the same dynamics as in the Gaussian noise case. With the Cauchy distribution, we used a more general coupling function that was still amenable to the OA reduction and from this, we were able to recover the same bifurcation structure as in the other models. Finally, in the case of the heterogeneous noise models, we were able to perform a rescaling analysis in the limit of narrow spread of heterogeneity and this analysis

again showed the underlying organizing dynamics.

There are several ways one could extend the present work. Here we have considered a single population of cells that are on average excitable. Many biological systems contain mixtures of cells that are spontaneously active (pacemakers) so one could use similar methods to consider systems with, say, two populations of cells whose means are such that they are oscillatory on average. We could then look at various types of interactions such as m:n-locking between the oscillatory and excitable populations [55]. We could also look into one population with a mean in the oscillatory range and one with a mean in the excitable range and see if there can be macroscopic oscillations in both populations. In the simplest such scenario, we could just periodically force all the cells in Eq. (11) and explore how the heterogeneity in the excitable cells disrupts the different locking regimes; we do something similar to this in our last project. Another more ambitious extension of the present work is to assume that the network is not globally connected but rather distributed in space. Coombes and Byrne [56] as well as others [57] have described methods for extending the OA approach to spatially distributed networks. Then, we might expect to see the spontaneous generation of waves in addition to synchrony. Lastly, one could explore different noise distributions and discover necessary or sufficient conditions on the noise distributions that would guarantee a group of all-to-all sinusoidally coupled excitable cells to generate oscillations.

4.0 Coupling one oscillator to each noise-driven excitable system

4.1 Introduction

Combining our first and second projects together, we will end this dissertation with coupling the noisy excitable cells from the second project with one oscillator. Doing this creates m:n locking as in the first project. In this last chapter, we will examine the stability of each m:n locking regime as a function of the noise's variance, either σ^2 or Δ. We find sets of lines in each m:n region and analyze how noisy the excitable cells can become until the oscillator can no longer create the m:n locking.

4.2 Gaussian

We begin as we did with project 2, with the standard model using Gaussian noise. We have

$$\begin{aligned} \dot{u}_i &= \mu - \cos(u_i) + c_{eo}\sin(x - u_i) + \frac{c_{ee}}{N}\sum_{j=1}^{N}\sin(u_j - u_i) + \xi_i(t) \\ \dot{x} &= 1 + \frac{c_{oe}}{N}\sum_{j=1}^{N}\sin(u_j - x) \end{aligned} \tag{35}$$

where $\xi_i(t)$ represents Gaussian white noise with mean 0 and variance $2\sigma^2$. The continuous version of these equations are as in the previous chapter and the probability density function, denoted by $F(t,u)$, satisfies the nonlinear diffusion equation

$$\frac{\partial}{\partial t}F(t,u) = -\frac{\partial}{\partial u}\left(F(t,u)\Big(\mu - \cos(u) + c_{eo}\sin(x-u) + c_{ee}\int_{-\pi}^{\pi}\sin(v-u)F(t,v)\,dv\Big)\right) + \sigma^2\frac{\partial^2}{\partial u^2}F(t,u).$$

We may again assume

$$F(t,u) = \frac{1}{2\pi}\sum_{n\in\mathbb{Z}} \rho_n(t) e^{-inu}$$

with $\rho_0 = 1$ and $\rho_{-n} = \rho_n^*$. By plugging this in to the Fokker-Planck equation and using system (35), we find

$$\begin{aligned}
\frac{d\rho_n}{dt} &= n\bigg(i\mu\rho_n - \frac{i}{2}\big(\rho_{n-1} + \rho_{n+1}\big) - \frac{c_{ee}}{2}\big(\rho_1^*\rho_{n+1} - \rho_1\rho_{n-1}\big) \\
&\qquad\qquad - \frac{c_{eo}}{2}\big(e^{-ix}\rho_{n+1} - e^{ix}\rho_{n-1}\big) - n\sigma^2\rho_n \bigg) \\
\dot{x} &= 1 + \frac{c_{oe}}{2i}\Big(\rho_1 e^{-ix} - \rho_1^* e^{ix}\Big).
\end{aligned} \tag{36}$$

Letting $\rho_n = r_n e^{i\theta_n}$, we arrive at

$$\begin{aligned}
\dot{r}_n &= -n^2\sigma^2 r_n + \frac{n}{2}\bigg(r_{n+1}\sin(\theta_{n+1} - \theta_n) + r_{n-1}\sin(\theta_{n-1} - \theta_n) \\
&\qquad + c_{ee} r_1 \Big(r_{n-1}\cos(\theta_{n-1} + \theta_1 - \theta_n) - r_{n+1}\cos(\theta_{n+1} - \theta_1 - \theta_n)\Big) \\
&\qquad + c_{eo}\Big(r_{n-1}\cos(\theta_{n-1} + x - \theta_n) - r_{n+1}\cos(\theta_{n+1} - x - \theta_n)\Big)\bigg) \\
\dot{\theta}_n &= n\mu - \frac{n}{2r_n}\bigg(r_{n+1}\cos(\theta_{n+1} - \theta_n) + r_{n-1}\cos(\theta_{n-1} - \theta_n) \\
&\qquad - c_{ee} r_1 \Big(r_{n-1}\sin(\theta_{n-1} + \theta_1 - \theta_n) - r_{n+1}\sin(\theta_{n+1} - \theta_1 - \theta_n)\Big) \\
&\qquad - c_{eo}\Big(r_{n-1}\sin(\theta_{n-1} + x - \theta_n) - r_{n+1}\sin(\theta_{n+1} - x - \theta_n)\Big)\bigg) \\
\dot{x} &= 1 + c_{oe} r_1 \sin(\theta_1 - x)
\end{aligned} \tag{37}$$

with $r_0 = 1$ and $\theta_0 = 0$. By taking $\rho_n = 0$, $\forall\, n > 20$, we can analyze this system to investigate the stability of m:n locking. In the rest of this chapter, we choose $\mu = 0.9$ and $c_{ee} = 0.5$; our goal is to vary c_{eo} and c_{oe}, similar to our first project.

Figure 32 shows the different locking patterns that we found for $\sigma^2 = 0.01$. We could not make $\sigma^2 = 0$ since this 20-mode truncation approximation is not valid as σ^2 tends to

	Line endpoints (c_{oe}, c_{eo}) for each region
1:2 locking	$(0.02, 0.50) \longrightarrow (0.42, 0.313) \longrightarrow (0.94, 0.118)$
1:3 locking	$(0.02, 0.426) \longrightarrow (0.40, 0.282) \longrightarrow (0.94, 0.115)$
1:4 locking	$(0.06, 0.38) \rightarrow (0.3, 0.296) \rightarrow (0.56, 0.216) \rightarrow (0.88, 0.131)$

Table 1: Line starting and ending points for system (37). These ordered pairs are plotted in top graph of Fig 32.

zero. The figure is very similar those in the first project; one can see we have 1:1 locking, 1:2 locking, and 0:1 locking. However, we have also added the smaller 1:3 and 1:4 locking regions since we will study these as well. We wish to study the robustness of each m:n locking regime so we decide to take sets of lines in each of the regions and study each point (c_{oe}, c_{eo}) on these sets of lines. To ensure we are able to study the entire length of the region, including low c_{oe} values and high c_{oe} values, we were forced to choose 2 lines in the 1:2 and 1:3 locking regimes and 3 lines in the 1:4 locking regime since the regions are so narrow. Table 1 gives the endpoints for each of the 7 lines. The lower graphs of Figure 32 show the vertical distance of the respective line to the respective region's border.

Next, we parameterize each line with parameter t for $0 < t < 1$. For each point on these lines, we have started with $\sigma^2 = 0.01$ and our goal is to increase σ^2 until the respective locking becomes unstable, similar to a subsection in the first project. Figure 33 shows this; the y-axis is the variable p with $p = 0$ denoting the beginning of each group of lines and $p = 1$ denoting the end of each group of lines. The colored dots depict when one line changes to the next line in the same locking regime. One can see that the lowest sensitivity to changes in σ^2 occurs at the transition points between these lines. Looking back to the lower three graphs in Fig. 32, these transition points roughly occur when the lines are closer to the bottom border of their region than to the top border. This suggests that when the noise level increases, the region's top border deteriorates first, allowing for any (c_{oe}, c_{eo}) value close to the bottom border to remain stable in the region for a longer range of σ^2.

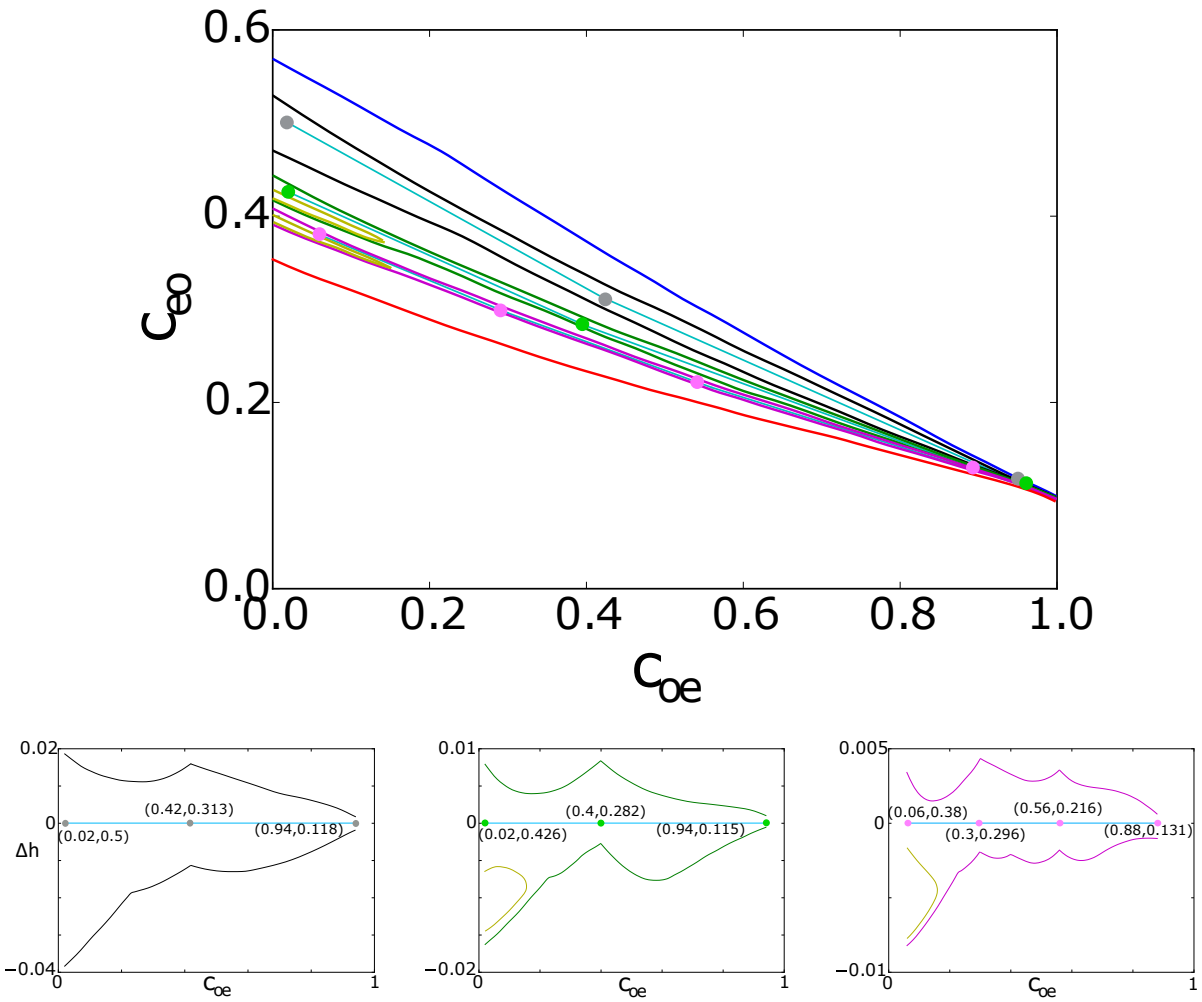

Figure 32: The top figure shows the regions of stability depending on c_{oe} and c_{eo} for $c_{ee} = 0.5$, $\mu = 0.9$ and $\sigma^2 = 0.01$. For (c_{oe}, c_{eo}) values above the blue curve, 1:1 locking is stable, between the black curves, 1:2 locking is stable, between the green curves, 1:3 locking is stable, between the purple curves, 1:4 locking is stable, and for (c_{oe}, c_{eo}) values below the red curve, 0:1-s locking is stable. There are also small yellow regions in the 1:3 and 1:4 locking regimes where we found 2:6 and 2:8 locking, respectively. The sets of lines we chose are also shown on this graph, with the dots representing the endpoints of each line; their (c_{oe}, c_{eo}) coordinates are given in the previous table and in the three graphs beneath the main figure. The lower three graphs show the projection of each region on their respective lines; this gives an idea of how far away these lines are from the edges of the region they lie in. The y-axis, Δh, represents the vertical distance from the respective line to the respective region's border.

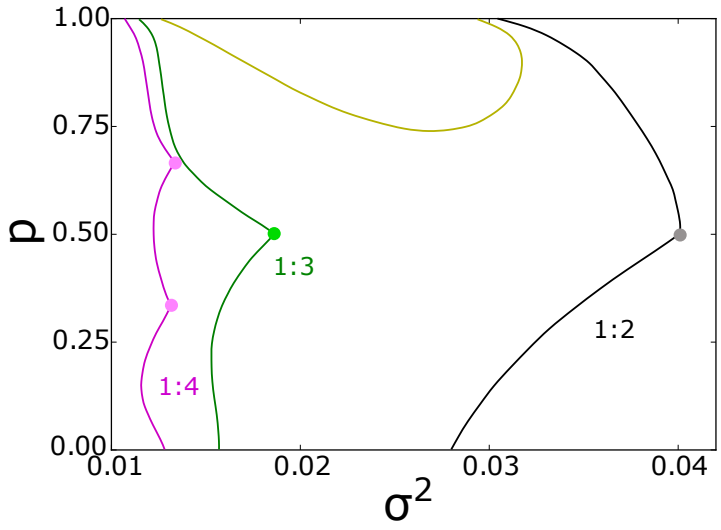

Figure 33: Threshold values for σ^2 in system (37). These curves represent the noise value where the respective locking switches from stable to unstable. It appears σ^2 has the largest threshold at the transition points between the lines. The yellow region is where the 1:2 locking becomes unstable and a period doubling bifurcation occurs, where 2:4 locking is stable. If one keeps increasing σ^2, the period doubling region vanishes and 1:2 locking is once again stable for a short while.

4.3 Cumulants

Beginning with system (36), we can make use of the cumulant closure reduction instead of the arbitrary 20 mode truncation. So, we take $\rho_3 = 3\rho_1\rho_2 - 2\rho_1^3$ and our equations become

$$\begin{aligned}
\dot{\rho}_1 &= i\mu\rho_1 - \frac{i}{2}\big(1+\rho_2\big) - \frac{c_{ee}}{2}\big(\rho_1^*\rho_2 - \rho_1\big) - \frac{c_{eo}}{2}\big(e^{-ix}\rho_2 - e^{ix}\big) - \sigma^2\rho_1 \\
\dot{\rho}_2 &= 2i\mu\rho_2 - \rho_1\big(i - c_{ee}\rho_1 - c_{eo}e^{ix}\big) - \big(i\rho_1 + c_{ee}|\rho_1|^2 + c_{eo}\rho_1 e^{-ix}\big)\big(3\rho_2 - 2\rho_1^2\big) - 4\sigma^2\rho_2 \\
\dot{x} &= 1 + \frac{c_{oe}}{2i}\Big(\rho_1 e^{-ix} - \rho_1^* e^{ix}\Big).
\end{aligned} \tag{38}$$

Letting $\rho_1(t) = r(t)e^{i\theta(t)}$ and $\rho_2(t) = s(t)e^{i\phi(t)}$, we find

$$\begin{aligned}
\dot{r} &= -\sigma^2 r - \frac{1}{2}\Big(\sin(\theta) - c_{ee}r - c_{eo}\cos(x-\theta)\Big) \\
&\qquad + \frac{s}{2}\Big(\sin(\phi-\theta) - c_{ee}r\cos(\phi-2\theta) - c_{eo}\cos(\phi-x-\theta)\Big) \\
\dot{\theta} &= \mu - \frac{1}{2r}\Big(\cos(\theta) + s\cos(\phi-\theta) - c_{eo}\sin(x-\theta)\Big) \\
&\qquad - \frac{s}{2r}\Big(c_{ee}r\sin(\phi-2\theta) + c_{eo}\sin(\phi-x-\theta)\Big) \\
\dot{s} &= -4\sigma^2 s + 3rs\Big(\sin(\theta) - c_{ee}r - c_{eo}\cos(\theta-x)\Big) + c_{ee}r^2(1+2r^2)\cos(2\theta-\phi) \\
&\quad - 2r^3\Big(\sin(3\theta-\phi) - c_{eo}\cos(3\theta-x-\phi)\Big) + r\Big(\sin(\theta-\phi) + c_{eo}\cos(\theta+x-\phi)\Big) \\
\dot{\phi} &= 2\mu - \frac{r}{s}\Big(\cos(\theta-\phi) - c_{eo}\sin(\theta+x-\phi)\Big) + \frac{c_{ee}r^2}{s}(1+2r^2)\sin(2\theta-\phi) \\
&\quad - 3r\Big(\cos(\theta) + c_{eo}\sin(\theta-x)\Big) + \frac{2r^3}{s}\Big(\cos(3\theta-\phi) + c_{eo}\sin(3\theta-x-\phi)\Big) \\
\dot{x} &= 1 + c_{oe}r\sin(\theta-x)
\end{aligned} \tag{39}$$

Using the cumulant moment reduction, we are able to begin our noise at $\sigma^2 = 0$. Doing this, we arrive at $s = r^2 = 1, \phi = 2\theta$ and

$$\begin{aligned}
\dot{\theta} &= \mu - \cos(\theta) + c_{eo}\sin(x-\theta) \\
\dot{x} &= 1 + c_{oe}\sin(\theta-x)
\end{aligned} \tag{40}$$

	Line endpoints (c_{oe}, c_{eo}) for each region in all systems where noise is zero
1:2 locking	$(0.07, 0.47) \longrightarrow (0.50, 0.29) \longrightarrow (0.96, 0.116)$
1:3 locking	$(0.12, 0.399) \longrightarrow (0.50, 0.26) \longrightarrow (0.93, 0.1255)$
1:4 locking	$(0.16, 0.361) \rightarrow (0.38, 0.285) \rightarrow (0.62, 0.212) \rightarrow (0.90, 0.1335)$

Table 2: Line starting and ending points with $\sigma^2 = 0$ in system (39). Later, we use these lines when $\Delta = 0$ for the OA systems.

which is equivalent to our first system in the beginning of the second chapter. Hence Figure 34, which plots the m:n locking regimes, will be nearly identical to Figure 3 from the beginning; the only difference is here, we use $\mu = 0.9$ which translates to $b = 10/9$ rather than $b = 11/10$ from the second chapter. Also in this new figure, we have added the 1:3 and the 1:4 locking region. Since the noise can begin at zero, we can use different sets of lines than before. These new lines are given in Table 2 and shown in Figures 34 and 35.

Again, we plan to increase σ^2 from 0 until the m:n locking becomes unstable; Figure 36 shows this. The colored dots again denote the transitions between the lines. This figure strongly resembles that of the 20-mode truncation, where the transition points between lines are when the noise threshold is at its largest. If one looks back to Figure 35, the transition points are again roughly where the line is closer to the bottom border than to the top border. We believe proximity to the borders influences maximum noise threshold, as well as many other factors.

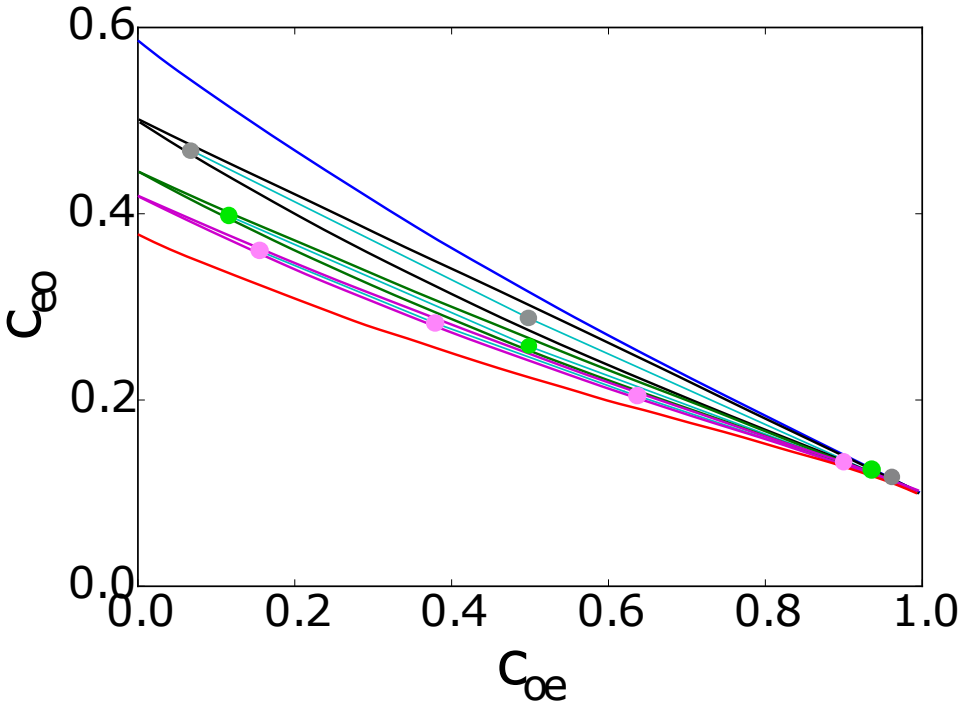

Figure 34: Regions of stability depending on c_{oe} and c_{eo}, for fixed $c_{ee} = 0.5, \mu = 0.9$ and $\sigma^2 = 0$ in system (39). Regions are the same as in Fig 32. Later, we use this same Figure for the heterogeneous noise models.

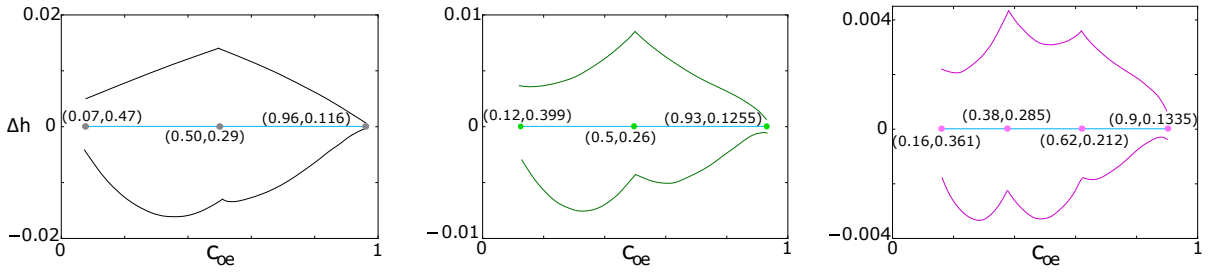

Figure 35: Each graph shows the vertical distance between the borders of each region and the respective line, as before. Notice the endpoints of the line again appear closer to the bottom border than to the top border, especially in the lines for the 1:3 and 1:4 locking. This is due to the curved shape of each of these regions. Lastly, since these figures were made with $\sigma^2 = 0$, we will have the same lines for the case of hetergeneous noise regardless which noise distribution $g(\omega)$ we choose.

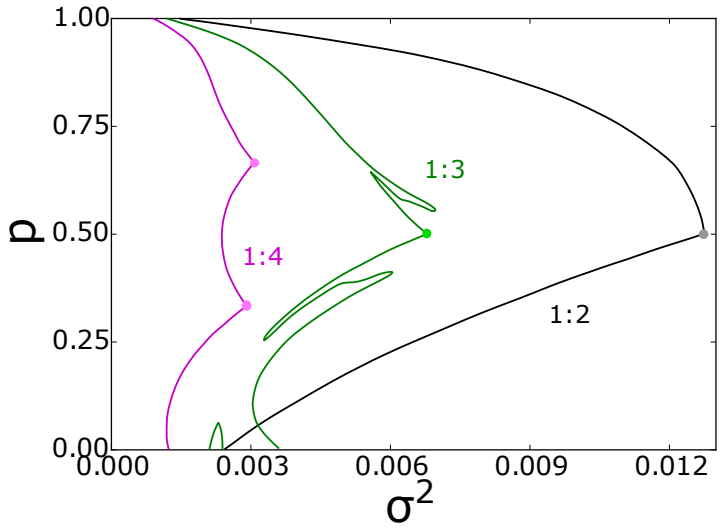

Figure 36: Threshold values of σ^2 for system (39). The dots mark the transition points between the lines. The same trend is happening here as in Fig 33: σ^2 is largest at the transition points between the lines. One difference we will see later is the magnitude of the noise threshold; when we use heterogeneous noise, the noise threshold will be much larger than the Gaussian or dynamic noise we are using here.

4.4 Ott-Antonsen ansatz

Moving on, we again consider one population of excitable cells u_i coupled with one oscillator, all given by

$$\dot{u_i} = \omega_i - \cos(u_i) + \frac{c_{ee}}{N}\sum_{j=1}^{N}\sin(u_j - u_i) + c_{eo}\sin(x - u_i)$$

$$\dot{x} = 1 + \frac{c_{oe}}{N}\sum_{j=1}^{N}\sin(u_j - x)$$

but with ω_i chosen from a density function $g(\omega)$; this is the heterogeneous noise scenario. Applying the same analysis and Ott-Antonsen ansatz as before, we arrive at a similar equation to (22):

$$\frac{\partial \alpha}{\partial t} = i\omega\alpha - \frac{i}{2}\big(1+\alpha^2\big) + \frac{c_{ee}}{2}\big(z - \alpha^2\overline{z}\big) + \frac{c_{eo}}{2}\big(e^{ix} - \alpha^2 e^{-ix}\big), \tag{41}$$

where $z(t)$ is once again

$$z(t) = \lim_{N\to\infty}\frac{1}{N}\sum_{j=1}^{N}e^{iu_j} = \int_0^{2\pi}\int_{-\infty}^{\infty}F(u,\xi,t)e^{iu}\,d\xi\,du = \int_{-\infty}^{\infty}\alpha(\omega,t)g(\omega)\,d\omega.$$

We begin with

$$g(\omega) := g_0(\omega) = \frac{1}{\pi}\frac{\Delta}{(\omega-\mu)^2 + \Delta^2}$$

with Δ measuring the spread of g_0 and μ is the center of g_0. Similar to before, $z(t) = \alpha(\mu + i\Delta, t)$. Lastly, the equation for $\dot{x}$ only requires the addition formula for $\sin(x)$ and the definition of $z(t)$. Plugging this in,

$$\begin{aligned}\dot{z} &= (-\Delta + i\mu)z - \frac{i}{2}z^2 - \frac{i}{2} + \frac{c_{ee}}{2}z\big(1 - z\overline{z}\big) + \frac{c_{eo}}{2}\big(e^{ix} - z^2e^{-ix}\big)\\ \dot{x} &= 1 + \frac{c_{oe}}{2i}\big(e^{-ix}z - e^{ix}\overline{z}\big).\end{aligned} \tag{42}$$

Let $z(t) = r(t)e^{i\theta(t)}$ and so

$$\begin{aligned}
\dot{r} &= -r\Delta - \frac{1-r^2}{2}\Big(\sin(\theta) - c_{ee}r - c_{eo}\cos(x-\theta)\Big) \\
\dot{\theta} &= \mu - \frac{1+r^2}{2r}\Big(\cos(\theta) - c_{eo}\sin(x-\theta)\Big) \\
\dot{x} &= 1 + c_{oe}r\sin(\theta - x).
\end{aligned} \tag{43}$$

When $\Delta = 0$, we arrive at system (40) so we are able to use the same sets of lines for this model. Later, this will be true for systems (43) and (45) as well. Figure 37 shows the threshold values for the standard Cauchy noise distribution. Notice with heterogeneous noise, the $x-$axis has a much greater range than when Gaussian noise was used. Also, we notice that when Δ increases and the stability for m:n locking is lost, 0:1 locking becomes stable. We give a sketch proof of this below.

Conjecture: For Δ large, system (43), has globally stable 0:1 locking for $0 < c_{eo} < 1$.

Proof (idea). As $\Delta \to \infty$, $r \to 0$ from the $\dot{r}$ equation and hence, $\dot{x} = 1$ meaning $x(t) = t$. Also for the $\dot{\theta}$ equation, we need $\cos(\theta) = c_{eo}\sin(t-\theta)$, which implies

$$\tan(\theta) = \frac{c_{eo}\sin(t) - 1}{c_{eo}\cos(t)}$$

Plotting this as an implicit function of θ shows that $\theta(t)$ is not firing for $0 < c_{eo} < 1$. □

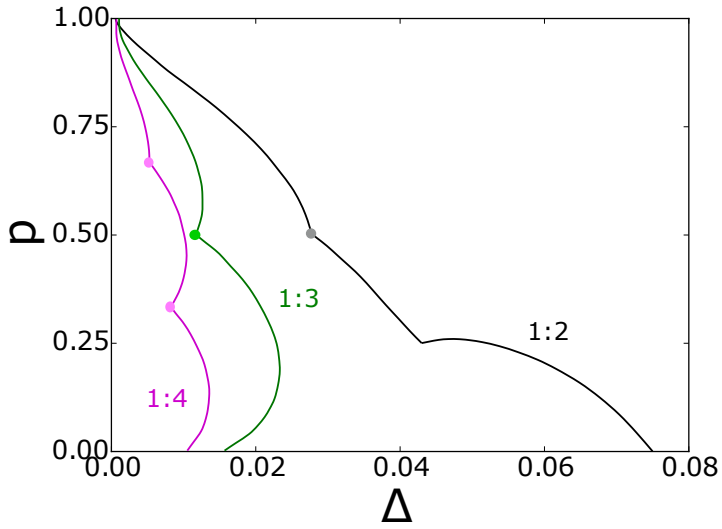

Figure 37: Threshold noise level for Δ in system (43). The dots mark the transition between each line. For each line, the stability of the lockings appear to have a higher sensitivity to changes in Δ near the endpoints, where the points are closer to the region's bottom border (see Fig 35), and appear to have low sensitivity to changes in Δ in the middle of each line, when the points are closer to the region's top border.

4.5 Changing $g(\omega)$

We also look at the same noise distributions as earlier, starting with the fourth power:

$$g(\omega) = g_1(\omega) := \frac{\sqrt{2}}{\pi}\frac{\Delta^3}{(\omega-\mu)^4+\Delta^4}.$$

As before, we arrive at

$$z(t) = \int_{-\infty}^{\infty} \alpha(\omega,t)g(\omega)\,d\omega = \gamma z_1 + \overline{\gamma} z_2$$

where $z_1 = \alpha(\mu + e^{i\pi/4}\Delta, t)$, $z_2 = \alpha(\mu - e^{-i\pi/4}\Delta, t)$ and $\gamma = \dfrac{1-i}{2}$. Plugging these into (41), we find

$$\begin{aligned}
\dot{z_1} &= i(\mu + e^{i\pi/4}\Delta)z_1 - \frac{i}{2}z_1^2 - \frac{c_{ee}}{2}z_1^2(\overline{\gamma z_1} + \gamma\overline{z_2}) - \frac{i}{2} + \frac{c_{ee}}{2}(\gamma z_1 + \overline{\gamma} z_2) + \frac{c_{eo}}{2}\big(e^{ix} - z_1^2 e^{-ix}\big)\\
\dot{z_2} &= i(\mu - e^{-i\pi/4}\Delta)z_2 - \frac{i}{2}z_2^2 - \frac{c_{ee}}{2}z_2^2(\overline{\gamma z_1} + \gamma\overline{z_2}) - \frac{i}{2} + \frac{c_{ee}}{2}(\gamma z_1 + \overline{\gamma} z_2) + \frac{c_{eo}}{2}\big(e^{ix} - z_2^2 e^{-ix}\big)\\
\dot{x} &= 1 + \frac{c_{oe}}{2i}\Big(e^{-ix}\big(\gamma z_1 + \overline{\gamma} z_2\big) - e^{ix}\big(\overline{\gamma z_1} + \gamma\overline{z_2}\big)\Big).
\end{aligned} \tag{44}$$

Writing $z_1(t) = r(t)e^{i\theta(t)}$ and $z_2(t) = s(t)e^{i\phi(t)}$, we see

$$\begin{aligned}
\dot{r} &= -\frac{\sqrt{2}}{2}r\Delta - \frac{1-r^2}{2}\Big(\sin(\theta) - c_{eo}\cos(x-\theta) - \frac{c_{ee}}{2}r - \frac{c_{ee}}{2}s\cos(\phi-\theta) + \frac{c_{ee}}{2}s\sin(\phi-\theta)\Big)\\
\dot{\theta} &= \mu + \frac{\sqrt{2}}{2}\Delta - \frac{1+r^2}{2r}\Big(\cos(\theta) - c_{eo}\sin(x-\theta) + \frac{c_{ee}}{2}r - \frac{c_{ee}}{2}s\cos(\phi-\theta) - \frac{c_{ee}}{2}s\sin(\phi-\theta)\Big)\\
\dot{s} &= -\frac{\sqrt{2}}{2}s\Delta - \frac{1-s^2}{2}\Big(\sin(\phi) - c_{eo}\cos(x-\phi) - \frac{c_{ee}}{2}s - \frac{c_{ee}}{2}r\cos(\theta-\phi) - \frac{c_{ee}}{2}r\sin(\theta-\phi)\Big)\\
\dot{\phi} &= \mu - \frac{\sqrt{2}}{2}\Delta - \frac{1+s^2}{2s}\Big(\cos(\phi) - c_{eo}\sin(x-\phi) - \frac{c_{ee}}{2}s + \frac{c_{ee}}{2}r\cos(\theta-\phi) - \frac{c_{ee}}{2}r\sin(\theta-\phi)\Big)\\
\dot{x} &= 1 + \frac{c_{oe}}{2}\Big(r\big(\sin(\theta-x) - \cos(\theta-x)\big) + s\big(\sin(\phi-x) + \cos(\phi-x)\big)\Big)
\end{aligned} \tag{45}$$

Figure 38 shows how large Δ can be for each point on each line in system (45) before the phase-locked solution is unstable. In the 1:4 graph, the threshold appears to be largest at the transition points between the lines. Similar to other remarks, these endpoints are closer to the bottom boundary of the 1:4 region than the top boundary, as is shown in Fig 35.

And lastly, we consider

$$g(\omega) = g_2(\omega) := \frac{2}{\pi}\frac{\Delta^3}{\big((\omega-\mu)^2+\Delta^2\big)^2}.$$

Using the steps shown in the Appendix and earlier, with $y(t) = \alpha(\mu + i\Delta, t)$, we have

$$\begin{aligned}
\dot{y} &= i\mu y - \Delta y - \frac{y^2}{2}\big(i + c_{ee}\overline{z} + c_{eo}e^{-ix}\big) - \frac{i}{2} + \frac{c_{ee}}{2}z + \frac{1}{2}c_{eo}e^{ix} \\
\dot{z} &= i\mu z - \Delta(z-y) - yz\big(i + c_{ee}\overline{z} + c_{eo}e^{-ix}\big) + \frac{y^2}{2}\big(i + c_{ee}\overline{z} + c_{eo}e^{-ix}\big) \\
&\qquad - \frac{i}{2} + \frac{c_{ee}}{2}z + \frac{1}{2}c_{eo}e^{ix} \\
\dot{x} &= 1 + \frac{c_{oe}}{2i}\Big(e^{-ix}z - e^{ix}\overline{z}\Big).
\end{aligned} \tag{46}$$

Letting $y(t) = r(t)e^{i\theta(t)}$ and $z(t) = s(t)e^{i\phi(t)}$, we arrive at

$$\begin{aligned}
\dot{r} &= -r\Delta - \frac{1-r^2}{2}\Big(\sin(\theta) - c_{eo}\cos(x-\theta) - c_{ee}s\cos(\phi-\theta)\Big) \\
\dot{\theta} &= \mu - \frac{1+r^2}{2r}\Big(\cos(\theta) - c_{eo}\sin(x-\theta) - c_{ee}s\sin(\phi-\theta)\Big) \\
\dot{s} &= -s\Delta + rs\big(\sin(\theta) - c_{eo}\cos(\theta-x)\big) - \frac{r^2}{2}\Big(\sin(2\theta-\phi) - c_{eo}\cos(2\theta-x-\phi)\Big) \\
&\quad + r\big(\Delta - c_{ee}s^2\big)\cos(\theta-\phi) + \frac{c_{ee}}{2}s\Big(1 + r^2\cos(2\theta-2\phi)\Big) - \frac{1}{2}\Big(\sin(\phi) - c_{eo}\cos(x-\phi)\Big) \\
\dot{\phi} &= \mu - r\big(\cos(\theta) + c_{eo}\sin(\theta-x)\big) + \frac{r^2}{2s}\Big(\cos(2\theta-\phi) + c_{eo}\sin(2\theta-x-\phi)\Big) \\
&\quad + \frac{r}{s}(\Delta - c_{ee}s^2)\sin(\theta-\phi) + \frac{c_{ee}}{2}r^2\sin(2\theta-2\phi) - \frac{1}{2s}\Big(\cos(\phi) - c_{eo}\sin(x-\phi)\Big) \\
\dot{x} &= 1 + c_{oe}s\sin(\phi-x).
\end{aligned} \tag{47}$$

We found that the maximum threshold of Δ in this section was overall similar to the threshold when we used $g(\omega) = g_1(\omega)$ and this is shown in Figure 39.

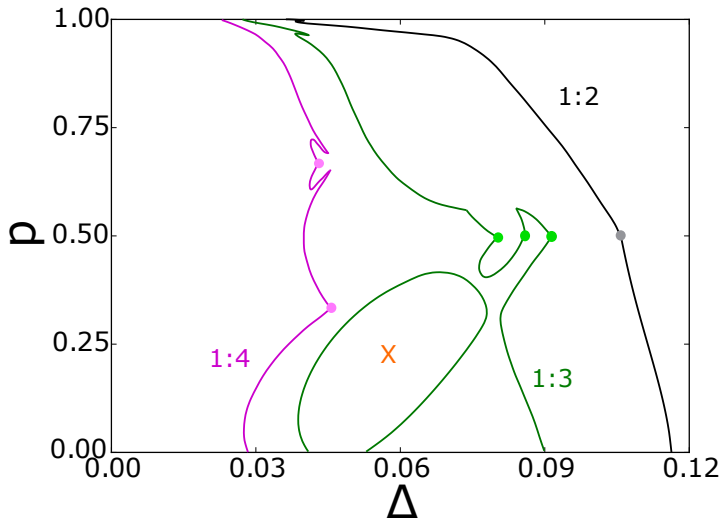

Figure 38: Noise threshold for Δ in system (45). One can see it is quite different from using the Cauchy distribution and has some strange behavior, especially in the 1:3 region. As Δ is allowed to increase, the 1:3 locking is disrupted by region X, where 0:3 locking is stable. Then, as Δ keeps increasing, 1:3 becomes stable again for a little while.

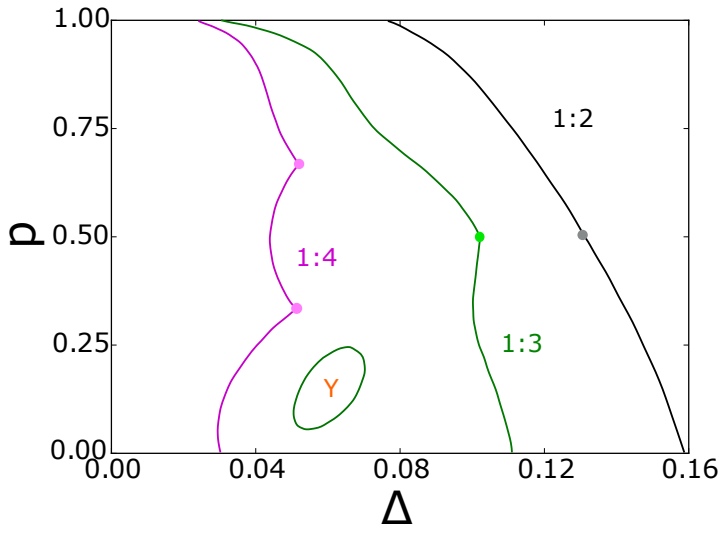

Figure 39: Threshold values for Δ in system (47). We can remark on its similarities to the previous figure. Region Y is also a region where 1:3 locking is lost and 0:3 locking becomes stable.

To reiterate, the systems that used $g_0(\omega)$, $g_1(\omega)$, and $g_2(\omega)$ had the same sets of lines. Because of this, we are able to compare the noise threshold for Δ for each density $g(\omega)$, given a specific m:n locking regime. We do this in Figs 40, 41 and 42 where, in each figure, the graph with no markers represents the Cauchy distribution, the graph with arrow markers represents the fourth power distribution, and the graph with circular markers represents the double root distribution.

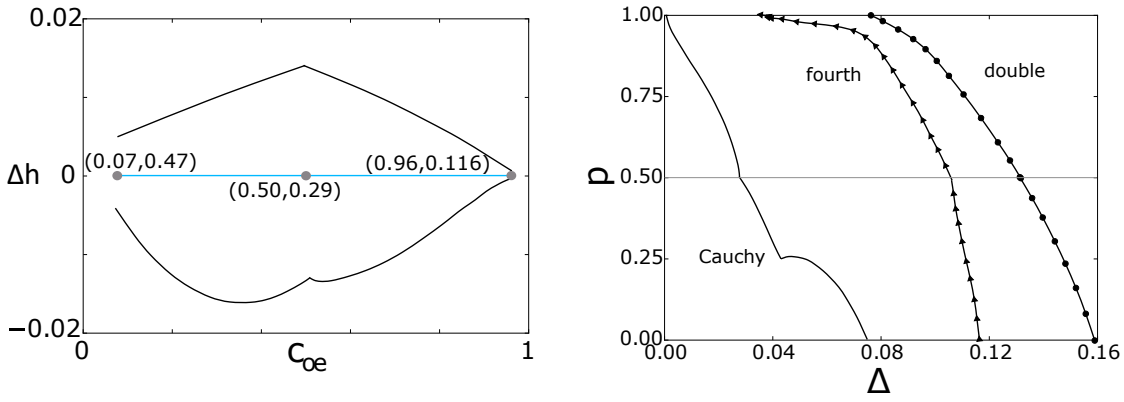

Figure 40: Comparing 1:2 locking for the heterogeneous noise systems. On the left is the vertical distance from the respective 1:2 line to each 1:2 boundary and on the right is the noise threshold for Δ for each of the three probability distributions. Notice how the noise threshold all three distributions generally decreases as we move down the 1:2 region in Fig 34. This will be slightly different when comparing the 1:3 and 1:4 locking patterns. Also, the Cauchy distribution will always have a lower noise threshold than the fourth power and double root distributions.

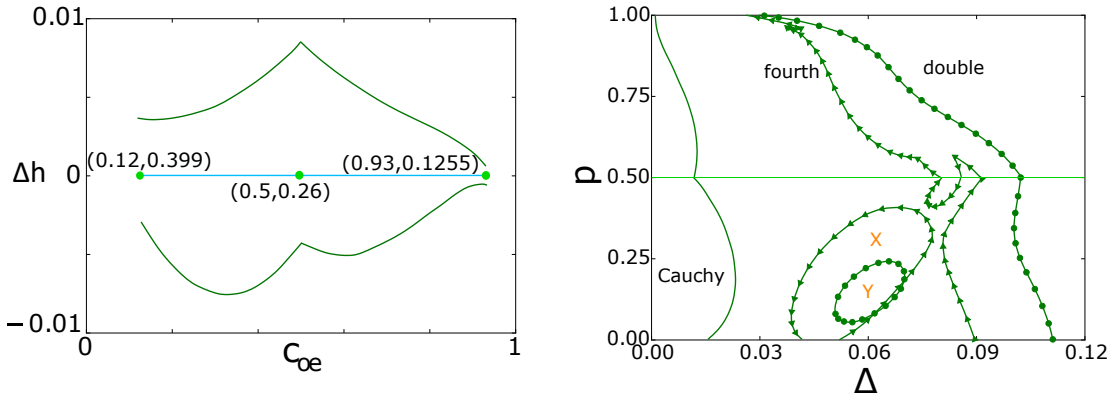

Figure 41: Comparing 1:3 locking for the heterogeneous noise systems. The fourth power and the double root distribution share many similar qualities: both have a 0:3 locking region and both are roughly constant for the first line then steadily decrease for the second line. For the Cauchy distribution, the maximum threshold appears to be in the middle of each line, unlike the other two distributions.

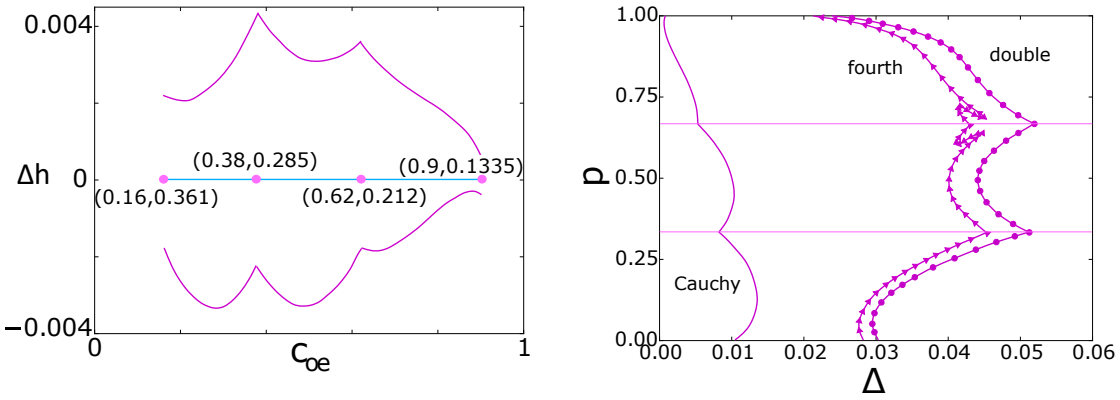

Figure 42: Comparing 1:4 locking for the heterogeneous noise systems. The fourth and double distributions are nearly identical, both peaking at the transition endpoints, whereas the Cauchy distribution looks the same as that in Figure 41, with peaks near the midpoints of each line.

4.6 Discussion

In this final section, we coupled each system of noisy excitable cells with one oscillator in order to recreate the m:n locking regimes that we had in the first project. However, unlike our first project, we had an extra parameter with these systems: the noise level of our noise distribution. We began with Gaussian white noise and truncated our system to 20 modes as before. We also started our noise at $\sigma^2 = 0.01$ since, as σ^2 tends to zero, the 20-mode truncation is no longer valid. At this noise level, we varied c_{eo} and c_{oe} and found different phase-locked solutions between the group of excitable cells and the single oscillator. To examine how large we could make σ^2, we set lines in each of the regions and for each point on the line, we increased σ^2 to see how large the noise level could become before instability occurred. Later, we performed the same analysis on the cumulant equations, where we could, in fact, take $\sigma^2 = 0$. Afterwards, we moved on to heterogeneous noise where we had three noise distributions: $g_0(\omega)$ (Cauchy), $g_1(\omega)$ (fourth), or $g_2(\omega)$ (double). We set $\Delta = 0$ in each of these models, noticed it had the same simplified bifurcation diagram as the cumulant model; thus, we used those lines for the analysis here. Comparing phase-locked solutions to each other, Δ had the potential to be largest when dealing with the 1:2 locking and the smallest when dealing with the 1:4 locking. Comparing noise distributions, the range for Δ was largest with the faster decaying distributions and smallest when using the Cauchy distribution. We suspect this is because the Cauchy distribution does not decay fast enough and thus, it is easier for the m:n locking to become unstable.

Studying populations of coupled oscillatory and excitable cells is a common topic, as we pointed out earlier (see [5, 6, 7, 8]); however, few networks, such as those involving circadian rhythm, will just use one oscillatory cell (also see [58]). As one can see, this is a clear extension of our second project but there could be many other extensions. One is to periodically force the excitable cells, rather than couple them with the oscillator (see [59, 60, 31, 61, 62, 63]). Another extension that was mentioned previously was to have two populations of cells. This can be done by letting $g(\omega)$ be a bimodal distribution, where one peak is in the excitable range and the other peak is in the oscillatory range. And notice that when the variance of the oscillatory population tends to infinity, it simplifies to our second

project and when the variance of the oscillatory population tends to 0, we return to our third project, with a few minor differences. These bimodal distributions could have different density functions for the different populations as well and the Ott-Antonsen ansatz can still be used.

5.0 Conclusions

In this dissertation, our goal was to understand how excitable cells and oscillatory cells interact with each other and, ultimately, decide if excitable cells could generate oscillations. In our first project, we began with a 1-dimensional chain model of one oscillator connected to one excitable cell and later extended this by adding another oscillator at the other end of the excitable cell and then adding another excitable cell in the middle of the chain. We found that this system exhibits m:n locking, where the excitable cells fire m times for every n times the oscillators fire. We also varied the oscillator frequencies and studied how this affected the stability of these m:n locking regions. Lastly with our OEEO model, we performed weak coupling analysis and the method of multiple time scales to prove the 0:1 anti-phase locking and the 0:1 synchrony locking meet as the parameter $c_{eo} \to 0$. With two excitable cells in the middle, both had the same steady state behavior (both fired or both did not fire), however, extending this beyond two inner excitable cells does not guarantee this, as we saw in the OEEEO model, even if you have the same parameters but different initial conditions. We also studied an OEO chain with an arbitrary number of E cells and connected this with traveling waves. Lastly, we looked into the Morris-Lecar model and used these dynamics in our OEEO system to retrieve our familiar m:n locking regions.

In our second project, we wanted to implement noise in our excitable cells, as this is a more realistic approach. Without oscillators to help, the excitable cells will not fire; however, if they have noise added, some excitable cells will begin to fire randomly. We must make sure that the noise has mean 0 so our excitable cells will be, on average, excitable. We studied both dynamic and heterogeneous noise and found that both types of noise could produce macroscopic oscillations. Using all-to-all coupling rather than chain-coupling, we took advantage of the Fokker-Plank equation and mean field theory methods to develop a finite number of differential equations for our model. Beginning with dynamic noise, noise that depends on time, we used Gaussian white noise and a moment closure, and we found there are regions of parameters where the excitable cells are, on average, excitable and the system exhibits oscillatory behavior. We also looked towards cumulant closure

rather than moment closure and found that we can achieve the same dynamics with a much smaller sized system. Next, we studied heterogeneous noise, which does not depend on time. Because this was all-to-all coupled, we again used the Fokker-Plank equation as well as the Ott-Antonsen ansatz, which assumes the Fourier coefficients of $F(t, u)$ are powers of n. By doing this, we arrive at a much simpler system of equations. However, we had to choose the density distribution from which the noise originated and as a consequence, we needed the densities to be easily integrated, preferably using the residue theorem. So we chose the Cauchy distribution and two fourth-power decaying distributions, which we have been calling "fourth power" and "double root" distributions. With the Cauchy distribution, under purely sinusoidal coupling, we were able to prove there were no oscillations for this noisy excitable system, for any parameters we choose. However, both the fourth power and the double root distributions had oscillatory behavior and had structure very similar to the moment closure and cumulant closure models when we used Gaussian noise. This structure comprised of two curves of fold bifurcations which met at a cusp point, a Hopf bifurcation which met one of the fold curves at a Takens-Bogdanov (TB) point, and a curve of homoclinic bifurcations which began at the TB point and continued to the other fold curve, where it met at a degenerate homoclinic (DH) point. As we decreased the noise in each model, we noticed that all three points, but specifically the TB point and cusp point, approached each other as well as the coupling went to 0 and the average excitability parameter μ approached 1. So, we performed a rescaling analysis to analyze if these points remain well-separated in the limit as $\Delta \to 0$ and found that they indeed remained separated. Afterwards, we modified our coupling function to include a cosine term. Once we did this, the Cauchy distribution exhibited macroscopic oscillations, similar to the other two densities. Lastly, we performed a rescaling analysis on this model and found that the three bifurcation points still remained well-separated.

In our third and final project, we extended our models to include the coupling of one oscillator and, in doing so, we can once again get m:n locking dependent on the parameters c_{eo} and c_{oe}, similar to the OE model from the first project. Now we have an extra parameter we did not have before: the noise level, σ^2 or Δ, depending on the type of noise. Hence, we began with zero or small noise to make our system resemble an OE system as much as

possible, then in each of the m:n locking regions, we studied sets of lines and for each point on these lines, we increased the noise threshold and studied how it affected the stability of the m:n locking region. This is similar to a subsection in our first project, where we varied the oscillator frequencies along similar lines. One thing to notice is the fourth power and double root density distributions have a larger tolerance for noise than the Cauchy distribution. Also, the heterogeneous noise models have a larger noise tolerance than the dynamic noise models.

In all, oscillators coupled with excitable cells have the ability to produce macroscopic oscillations and phase-locking patterns. And, from the second project, as long as the excitable cells are driven by some noise, oscillations can also persist. The third project, which introduced one oscillatory cell, can give insight to networks focused on the cardiac system, however there, cells are more locally coupled rather than globally coupled. Still, if we relax our assumptions in this project, we can find more promising and realistic results. These theoretical approaches are paramount to understanding how neurons interact with each other in the real world.

Appendix

A.1 Residue theory for $g_1(\omega)$

To arrive at Eq (29), we use the residue theorem and take the contour around the upper half of the complex plane to get

$$z(t) = \int_{-\infty}^{\infty} \alpha(\omega,t)g(\omega)\,d\omega = 2\pi i\frac{\Delta^3\sqrt{2}}{\pi}\Bigg(\lim_{\omega\to\mu+e^{i\pi/4}\Delta}\frac{(\omega-\mu-e^{i\pi/4}\Delta)\alpha(\omega,t)}{(\omega-\mu)^4+\Delta^4} + \lim_{\omega\to\mu-e^{-i\pi/4}\Delta}\frac{(\omega-\mu+e^{-i\pi/4}\Delta)\alpha(\omega,t)}{(\omega-\mu)^4+\Delta^4}\Bigg)$$

$$= 2\pi i\frac{\Delta^3\sqrt{2}}{\pi}\Bigg(\alpha(\mu+e^{i\pi/4}\Delta,t)\lim_{\omega\to\mu+e^{i\pi/4}\Delta}\frac{1}{4(\omega-\mu)^3} + \alpha(\mu-e^{-i\pi/4}\Delta,t)\lim_{\omega\to\mu-e^{-i\pi/4}\Delta}\frac{1}{4(\omega-\mu)^3}\Bigg)$$

$$= i\frac{\sqrt{2}}{2}\Big(e^{-3i\pi/4}\alpha(\mu+e^{i\pi/4}\Delta,t) - e^{3i\pi/4}\alpha(\mu-e^{-i\pi/4}\Delta,t)\Big).$$

And so we find $z(t) = \gamma z_1 + \overline{\gamma} z_2$ where $z_1 = \alpha(\mu+e^{i\pi/4}\Delta,t)$, $z_2 = \alpha(\mu-e^{-i\pi/4}\Delta,t)$ and $\gamma = i\frac{\sqrt{2}}{2}e^{-3i\pi/4} = \frac{1-i}{2}$. Plugging these into (22), we see

$$\begin{aligned}\dot{z_1} &= i(\mu+e^{i\pi/4}\Delta)z_1 - \frac{i}{2}z_1^2 - \frac{c_{ee}}{2}z_1^2(\overline{\gamma z_1}+\gamma\overline{z_2}) - \frac{i}{2} + \frac{c_{ee}}{2}(\gamma z_1+\overline{\gamma}z_2)\\ \dot{z_2} &= i(\mu-e^{-i\pi/4}\Delta)z_2 - \frac{i}{2}z_2^2 - \frac{c_{ee}}{2}z_2^2(\overline{\gamma z_1}+\gamma\overline{z_2}) - \frac{i}{2} + \frac{c_{ee}}{2}(\gamma z_1+\overline{\gamma}z_2).\end{aligned} \tag{48}$$

Writing $z_1(t) = r(t)e^{i\theta(t)}$ and $z_2(t) = s(t)e^{i\phi(t)}$, we separate real and complex parts and arrive at (29).

A.2 Residue theory for $g_2(\omega)$

The main difference in deriving (30) is that there is a pole of order 2 instead of order 1. Again taking the contour around the upper half of the complex plane, we see

$$z(t) = \int_{-\infty}^{\infty} \alpha(\omega,t)g(\omega)\,d\omega = 2\pi i\frac{2\Delta^3}{\pi}\left(\lim_{\omega\to\mu+i\Delta}\frac{\partial}{\partial\omega}\left[\frac{(\omega-\mu-i\Delta)^2\alpha(\omega,t)}{\left((\omega-\mu)^2+\Delta^2\right)^2}\right]\right)$$

$$= 4\Delta^3 i\lim_{\omega\to\mu+i\Delta}\frac{\partial}{\partial\omega}\left[\frac{\alpha(\omega,t)}{(\omega-\mu+i\Delta)^2}\right] = \lim_{\omega\to\mu+i\Delta}\left(\frac{4\Delta^3 i}{(\omega-\mu+i\Delta)^2}\frac{\partial\alpha}{\partial\omega}(\omega,t) - \frac{8\Delta^3 i\,\alpha(\omega,t)}{(\omega-\mu+i\Delta)^3}\right)$$

and so

$$z(t) = -i\Delta\frac{\partial\alpha}{\partial\omega}(\mu+i\Delta,t) + \alpha(\mu+i\Delta,t) \tag{49}$$

where $\dfrac{\partial\alpha}{\partial\omega}(\mu+i\Delta,t) = \dfrac{\partial\alpha}{\partial\omega}(\omega,t)\Big|_{\omega=\mu+i\Delta}$. Taking the derivative with respect to time on both sides and then using (22), we get

$$\dot{z}(t) = -i\Delta\frac{\partial}{\partial\omega}\left(\frac{\partial\alpha}{\partial t}(\omega,t)\right)\Big|_{\omega=\mu+i\Delta} + \frac{\partial\alpha}{\partial t}(\mu+i\Delta,t)$$

$$= -i\Delta\frac{\partial}{\partial\omega}\left(i\,\alpha(\omega,t)\omega - \frac{i}{2} - \frac{i}{2}\alpha^2(\omega,t) - \frac{c_{ee}}{2}\alpha^2(\omega,t)\overline{z} + \frac{c_{ee}}{2}z\right)\Big|_{\omega=\mu+i\Delta}$$
$$+ i(\mu+i\Delta)\,\alpha(\mu+i\Delta,t) - \frac{i}{2} - \frac{i}{2}\alpha^2(\mu+i\Delta,t) - \frac{c_{ee}}{2}\alpha^2(\mu+i\Delta,t)\overline{z} + \frac{c_{ee}}{2}z.$$

Let $y = y(t) = \alpha(\mu+i\Delta,t)$. Then we have

$$\dot{z} = -i\Delta\Big(i(\mu+i\Delta)\frac{\partial\alpha}{\partial\omega}(\mu+i\Delta,t) + iy - iy\frac{\partial\alpha}{\partial\omega}(\mu+i\Delta,t) - c_{ee}y\overline{z}\frac{\partial\alpha}{\partial\omega}(\mu+i\Delta,t)\Big)$$
$$+ (i\mu-\Delta)y - \frac{i}{2} - \frac{i}{2}y^2 - \frac{c_{ee}}{2}y^2\overline{z} + \frac{c_{ee}}{2}z$$

$$= -i\Delta\frac{\partial\alpha}{\partial\omega}(\mu + i\Delta, t)\left(i\mu - \Delta - iy - c_{ee}y\overline{z}\right) + i\mu y - \frac{i}{2} - \frac{i}{2}y^2 - \frac{c_{ee}}{2}y^2\overline{z} + \frac{c_{ee}}{2}z$$

$$= (z - y)(i\mu - \Delta - iy - c_{ee}y\overline{z}) + i\mu y - \frac{i}{2} - \frac{i}{2}y^2 - \frac{c_{ee}}{2}y^2\overline{z} + \frac{c_{ee}}{2}z$$

where we used (49). The equation for $\dot{y}$ uses equation (22) and so, putting them together,

$$\begin{aligned}
\dot{y} &= i\mu y - \Delta y - \frac{i}{2}y^2 - \frac{i}{2} - \frac{c_{ee}}{2}y^2\overline{z} + \frac{c_{ee}}{2}z \\
\dot{z} &= i\mu z - \Delta z + \Delta y - iyz + \frac{i}{2}y^2 - c_{ee}yz\overline{z} + \frac{c_{ee}}{2}y^2\overline{z} - \frac{i}{2} + \frac{c_{ee}}{2}z.
\end{aligned} \tag{50}$$

As before, letting $y(t) = r(t)e^{i\theta(t)}$ and $z(t) = s(t)e^{i\phi(t)}$, we arrive at (30).

A.3 Takens-Bogdanov point for the rescaling analysis with $g_2(\omega)$

We will show the TB point for the rescaling analysis with the double root distribution occurs at $(\mu_2, c_1) = (\mu, c) = (-2/9, 4/3)$. With this information, we can also find the fixed point values $(r_1, \theta_1, s_1, \phi_1) = (r, \theta, s, \phi) = (-1/2, 5/6, -1, 1/3)$. We begin by rewriting the rescaling equations for the double root distribution with the subscripts omitted:

$$\begin{aligned}
\dot{r} &= -r(c - \phi) - s(\phi - \theta) \\
\dot{\theta} &= \mu - \frac{1}{2}\phi^2 + \phi\theta - rs + \frac{1}{2}s^2 \\
\dot{s} &= -1 - s(c - \phi) \\
\dot{\phi} &= \mu + \frac{1}{2}\phi^2 - c(\phi - \theta) - \frac{1}{2}s^2.
\end{aligned} \tag{51}$$

We also know that $r < 0$, $s < 0$, and $c > 0$. Denote J as the Jacobian of this system and let $f(\lambda) := \det(J - \lambda I)$ where I is the identity matrix. By the definition of the Takens-Bogdanov point, we require $f(0) = f'(0) = 0$. To get started, we write the Jacobian matrix below:

$$J := \begin{pmatrix} \phi - c & s & \theta - \phi & r - s \\ -s & \phi & s - r & \theta - \phi \\ 0 & 0 & \phi - c & s \\ 0 & c & -s & \phi - c \end{pmatrix}.$$

Now, $f(\lambda)$ will be as follows:

$$f(\lambda) = \det \begin{pmatrix} \phi - c - \lambda & s & \theta - \phi & r - s \\ -s & \phi - \lambda & s - r & \theta - \phi \\ 0 & 0 & \phi - c - \lambda & s \\ 0 & c & -s & \phi - c - \lambda \end{pmatrix}$$

$$= (\phi - c - \lambda)\Big((\phi - c)\Big((\phi - c - \lambda)^2 + s^2\Big) + c\Big(s(s - r) - (\theta - \phi)(\phi - c - \lambda)\Big)\Big) + s\Big(s\Big((\phi - c - \lambda)^2 + s^2\Big) + c\Big(s(\theta - \phi) - (r - s)(\phi - c - \lambda)\Big)\Big)$$

$$= \Big(s^2 + (\phi - c - \lambda)^2\Big)\Big(s^2 + (\phi - c - \lambda)^2 + c(\phi - c - \lambda)\Big) - c(\theta - \phi)\Big((\phi - c - \lambda)^2 - s^2\Big) + 2sc(s - r)(\phi - c - \lambda).$$

Further, we also need to be at a fixed point so $\dot{r} = \dot{\theta} = \dot{s} = \dot{\phi} = 0$. From the $\dot{s}$ equation, we know $\phi - c = 1/s$ and by subtracting the $\dot{\phi}$ equation from the $\dot{\theta}$ equation, we can rearrange and find $\theta - \phi = s^2(r - s)$. Plugging these into $f(\lambda)$ yields

$$f(\lambda) = \Big(s^2 + (1/s - \lambda)^2\Big)\Big(s^2 + (1/s - \lambda)^2 + c(1/s - \lambda)\Big) - cs^2(r - s)\Big((1/s - \lambda)^2 - s^2 + 2/s^2 - 2\lambda/s\Big).$$

Setting $f(0) = 0$ and $f'(0) = 0$, we arrive at

$$\Big(s^2 + 1/s^2\Big)\Big(s^2 + 1/s^2 + c/s\Big) - cs^2(r - s)\Big(3/s^2 - s^2\Big) = 0 \tag{52}$$

and

$$(-4/s)\Big(s^2+1/s^2\Big)-c\Big(s^2+3/s^2\Big)+4cs(r-s)=0, \tag{53}$$

respectively. In (53), we can solve and find

$$cs^2(r-s)=s^2+1/s^2+\frac{cs}{4}\Big(s^2+3/s^2\Big).$$

With this, the left hand side of (52) becomes

$$\Big(s^2+1/s^2\Big)\Big(s^2+1/s^2+c/s\Big)-\Big(s^2+1/s^2+\frac{cs}{4}\Big(s^2+3/s^2\Big)\Big)\Big(3/s^2-s^2\Big)$$

$$=\Big(s^2+1/s^2\Big)\Big(s^2+1/s^2-3/s^2+s^2\Big)-\frac{cs}{4}\Big(9/s^4-s^4-4-4/s^4\Big)$$

$$=\Big(2+2/s^4\Big)(s^4-1)+\frac{c}{4s^3}\Big(s^8+4s^4-5\Big)=(s^4-1)\Big(2+2/s^4+\frac{c}{4s^3}(s^4+5)\Big).$$

Hence, we have

$$(s^4-1)(cs^5+8s^4+5cs+8)=0 \tag{54}$$

as our new equation. Now we will modify equation (53). We know $\theta-\phi=s^2(r-s)$ and using $\dot{r}=0$, we get $r=s^2(\phi-\theta)$. Combining these, we find that $r=\dfrac{s^5}{s^4+1}$. So (53) can be modified to

$$(-4/s)\Big(s^2+1/s^2\Big)-c\Big(s^2+3/s^2\Big)-\frac{4cs^2}{s^4+1}=0.$$

Solving for c will yield

$$c=-\frac{4(s^4+1)^2}{s(s^8+8s^4+3)}. \tag{55}$$

Supposing $s^4\neq 1$ in (54), then we must have $c=-\dfrac{8(s^4+1)}{s(s^4+5)}$. However, this equation and equation (55) never intersect. Thus, $s^4=1$, and since $s<0$, we have $s=-1$. This implies $c=4/3$ from (55) and from earlier formulas, $r=-1/2$, $\phi=c+1/s=1/3$ and $\theta=5/6$. Finally, using the $\dot{\phi}$ or $\dot{\theta}$ equation, one finds $\mu=-2/9$.

A.4 Cusp curve for the rescaling analysis with the Cauchy distribution

We begin the proof of $c_{cusp}(\mu)$ by eliminating the subscripts in (34) as before. Since the cusp occurs at a fixed point, $\dot{r} = \dot{\theta} = 0$ and so $\theta = c + 1/r$. Thus, $\dot{\theta} = -\dot{r}/r^2$. Solving for $\dot{r}$ and using (34), we have

$$\dot{r} = -r^2\Big(\frac{1}{2}(c+1/r)^2 - \frac{1}{2}r^2 - bcr + \mu\Big) = \frac{1}{2}\Big(r^4 + 2bcr^3 - (c^2+2\mu)r^2 - 2cr - 1\Big) =: \frac{1}{2}f(r).$$

Now that θ has been eliminated from the system of equations, we can work with $f(r)$ alone. At the cusp bifurcation specifically, we know that $f(r) = f'(r) = f''(r) = 0$. So we have three equations:

$$r^4 + 2bcr^3 - (c^2+2\mu)r^2 - 2cr - 1 = 0 \tag{56}$$

$$2r^3 + 3bcr^2 - (c^2+2\mu)r - c = 0 \tag{57}$$

$$6r^2 + 6bcr - (c^2+2\mu) = 0. \tag{58}$$

Our task is to eliminate r and b. Begin by multiplying (57) by $2r$ and subtracting it from (56). Also, multiply (57) by r and subtract off (56). Respectively, we arrive at

$$-3r^4 - 4bcr^3 + (c^2+2\mu)r^2 - 1 = 0 \tag{59}$$

$$r^4 + bcr^3 + cr + 1 = 0. \tag{60}$$

Next, multiply (58) by $2r^2$ and add it to three times (59) and multiply (58) by r^2 and subtract it from six times (60). This results in our two main equations with b removed:

$$3r^4 + (c^2+2\mu)r^2 - 3 = 0 \tag{61}$$

$$(c^2+2\mu)r^2 + 6cr + 6 = 0. \tag{62}$$

Now we solve for r^2 in (61) and we set it equal to the square of the solution for r in (62). Keeping in mind that r is negative, we find

$$\frac{-(c^2+2\mu)+\sqrt{(c^2+2\mu)^2+36}}{6} = \left(\frac{-3c+\sqrt{3c^2-12\mu}}{c^2+2\mu}\right)^2.$$

Distributing the right hand side and putting the radicals on one side, one has

$$(c^2+2\mu)^2\sqrt{(c^2+2\mu)^2+36}+36c\sqrt{3c^2-12\mu} = 72(c^2-\mu)+(c^2+2\mu)^3.$$

Squaring both sides and simplifying yet again by putting the radicals on one side, we see

$$2c\sqrt{(c^2+2\mu)^2+36}\sqrt{3c^2-12\mu} = 3c^4+12(3-\mu^2).$$

We square both sides one last time and notice this is a fourth order polynomial in c^2, and we can use the quartic formula to obtain $c_{cusp}(\mu)$, given in the chapter. It is important to note the coefficient of c^6 is zero once you square both sides, which will greatly simplify the curve equation. Lastly, even though we cannot find μ_{cusp} and c_{cusp} in terms of a general b, we list some properties for $\big(\mu_{cusp}(b), c_{cusp}(b)\big)$:

1. $\big(\mu_{cusp}(1), c_{cusp}(1)\big) = (-1/2, 1)$
2. $\big(\mu_{cusp}(0), c_{cusp}(0)\big) = \Big(3^{-3/2}, 4(3^{-3/4})\Big) \approx (0.19245, 1.75477)$
3. $\mu_{cusp}(b^*) = 0$ when $b^* = \frac{1}{3}\sqrt{2\sqrt{3}-3} \approx 0.227083$ and $c_{cusp}(b^*) = \sqrt[4]{12(2\sqrt{3}-3)} \approx 1.5362$
4. $\lim\limits_{b\to\infty}(\mu_{cusp}(b), c_{cusp}(b)) = (-\sqrt{3}, 0)$
5. $c_{cusp} \sim 1/b$ and $\mu_{cusp}+\sqrt{3} \sim 1/b$ for b large.

Bibliography

[1] A. J. Durston, *Pacemaker activity during aggregation in Dictyostelium discoideum*, Dev. Biol., 37 (1974), pp. 225–235.

[2] K. M. Sanders, *A case for interstitial cells of Cajal as pacemakers and mediators of neurotransmission in the gastrointestinal tract*, Gastroenterology, 111 (1996), pp. 492–515.

[3] K. M. Sanders, S. M. Ward, *Interstitial cells of Cajal: a new perspective on smooth muscle function*, J. Physiol., 576 (2006), pp. 721–726.

[4] L. M. Prolo, J. S. Takahashi, E. D. Herzog, *Circadian rhythm generation and entrainment in astrocytes*, J. Neurosci., 25 (2005), pp. 404–408.

[5] H. Daido, K. Nakanishi, *Aging transition and universal scaling in oscillator networks*, Phys. Rev. Lett., 93 (2004), 104101.

[6] D. Pazó, E. Montbrió, *Universal behavior in populations composed of excitable and self-oscillatory elements*, Phys. Rev. E, 73 (2006), 055202.

[7] H. Daido, A. Kasama, K. Nishio, *Onset of dynamic activity in globally coupled excitable and oscillatory units*, Phys. Rev. E, 88 (2013), 052907.

[8] K. P. O'Keeffe, S. H. Strogatz, *Dynamics of a population of oscillatory and excitable elements*, Phys. Rev. E, 93 (2016), 062203.

[9] T. B. Luke, E. Barreto, P. So, *Macroscopic complexity from an autonomous network of networks of theta neurons*, Front. Comput. Neurosci., 8 (2014), 145.

[10] T. B. Luke, E. Barreto, P. So, *Complete classification of the macroscopic behavior of a heterogeneous network of theta neurons*, Neural Comput., 25 (2013), pp. 3207–3234.

[11] S. M. Crook, G. B. Ermentrout, J. M. Bower, *Dendritic and synaptic effects in systems of coupled cortical oscillators*, J. Computat. Neurosci., 5 (1998), pp. 315–329.

[12] J. A. Goldberg, C. A. Deister, C. J. Wilson, *Response properties and synchronization of rhythmically firing dendritic neurons*, J. Neurophys., 97 (2007), pp. 208–219.

[13] C. M. Svensson, S. Coombes, *Mode locking in a spatially extended neuron model: active soma and compartmental tree*, IBJC, 19 (2009), pp. 2597–2607.

[14] J. Rinzel, G. B. Ermentrout, *Analysis of neural excitability and oscillations*, Meth. Neuron. Model., (1989), pp. 135–169.

[15] S. Shinomoto, Y. Kuramoto, *Phase transitions in active rotator systems*, Prog. Theor. Phys., 75 (1986), pp. 1105–1110.

[16] G. B. Ermentrout, J. Rinzel, *Waves in a simple, excitable or oscillatory, reaction-diffusion model*, J. Math. Biol., 11 (1981), pp. 269–294.

[17] G. B. Ermentrout, *Simulating, analyzing, and animating dynamical systems: a guide to XPPAUT for researchers and students*, SIAM, 14 (2002).

[18] R. L. Stratonovich, *Topics in the Theory of Random Noise Vol. 2*, Gordon and Breach, New York, 1967.

[19] C. Kurrer, K. Schulten, *Noise-Induced Synchronous Neuronal Oscillations*, Phys. Rev. E, 51 (1995), 6213.

[20] Y. M. Lai, M. A. Porter, *Noise-Induced Synchronization, Desynchronization, and Clustering in Globally Coupled Nonidentical Oscillators*, Phys. Rev. E, 88 (2013), 012905.

[21] M. Scheutzow, *Noise Can Create Periodic Behavior and Stabilize Nonlinear Diffusions*, Stoch. Proc. Appl., 20 (1985), pp. 323–331.

[22] L. Glass, P. Hunter, A. McCulloch, eds., *Theory of heart: Biomechanics, biophysics, and nonlinear dynamics of cardiac function.* Springer Science & Business Media, New York, 2012.

[23] J. Rinzel, G. B. Ermentrout, *Analysis of neural excitability and oscillations*, Meth. Neuron. Model., 2 (1998), pp. 251–292.

[24] A. P. LeBeau, et al., *Modeling of membrane excitability in gonadotropin-releasing hormone-secreting hypothalamic neurons regulated by Ca2+-mobilizing and adenylyl cyclase-coupled receptors*, J. Neurosci., 20 (2000), pp. 9290–9297.

[25] H. Sakaguchi, S. Shinomoto, Y. Kuramoto, *Phase Transitions and Their Bifurcation Analysis in a Large Population of Active Rotators with Mean-Field Coupling*, Prog. Theor. Exp. Phys., 79 (1988), pp. 600–607.

[26] A. Neiman, L. Schimansky-Geier, A. Cornell-Bell, F. Moss, *Noise-Enhanced Phase Synchronization in Excitable Media*, Phys. Rev. Lett., 83 (1999), pp. 4896–4899.

[27] B. Lindner, J. García-Ojalvo, A. Neiman, L. Schimansky-Geier, *Effects of noise in excitable systems*, Phys. Rep., 392 (2004), pp. 321–424.

[28] M. Zaks, X. Sailer, L. Schimansky-Geier, A. Neiman, *Noise Induced Complexity: From Subthreshold Oscillations to Spiking in Coupled Excitable Systems*, Chaos, 15 (2005), 026117.

[29] E. Luçon, C. Poquet, *Emergence of Oscillatory Behaviors for Excitable Systems with Noise and Mean-Field Interaction, A Slow-Fast Dynamics Approach*, Commun. Math. Phys., 373 (2020), pp. 907–969.

[30] A. Faisal, L. Selen, D. Wolpert, *Noise in the Nervous System*, Nat. Rev. Neurosci., 9 (2008), pp. 292–303.

[31] J. D. Touboul, C. Piette, L. Venance, G. B. Ermentrout, *Noise-Induced Synchronization and Antiresonance in Interacting Excitable Systems: Applications to Deep Brain Stimulation in Parkinson's Disease*, Phys. Rev. X, 10 (2020), 011073.

[32] A. Neiman, X. Pei, D. Russell, W. Wojtenek, L. Wilkens, F. Moss, H. Braun, M. Huber, K. Voigt, *Synchronization of the noisy electrosensitive cells in the paddlefish*, Phys. Rev. Lett., 82 (1999), pp. 660–663.

[33] L. M. Alonso, G. B. Mindlin, *Average dynamics of a driven set of globally coupled excitable units*, Chaos, 21 (2011), 023102.

[34] R. E. Lee DeVille, E. Vanden-Eijnden, C. B. Muratov, *Two distinct mechanisms of coherence in randomly perturbed dynamical systems*, Phys. Rev. E, 72 (2005), 031105.

[35] J. Touboul, G. Hermann, O. Faugeras, *Noise-Induced Behaviors in Neural Mean Field Dynamics*, SIAM J. Appl. Dyn. Syst., 11 (2012), pp. 49–81.

[36] K. Dierkes, F. Jülicher, B. Lindner, *A Mean-Field Approach to Elastically Coupled Hair Bundles*, Eur. Phys. J. E., 35 (2012), pp. 37–51.

[37] B. Sonnenschein, M. Zaks, A. Neiman, L. Schimansky-Geier, *Excitable elements controlled by noise and network structure*, EPJ ST, 222 (2013), pp. 2517–2529.

[38] E. Ott, T. M. Antonsen, *Low dimensional behavior of large systems of globally coupled oscillators*, Chaos, 18 (2008), 037113.

[39] J. G. Restrepo, E. Ott, *Mean-field theory of assortative networks of phase oscillators*, EPL, 107 (2014), 60006.

[40] L. F. Lafuerza, P. Colet, R. Toral, *Nonuniversal Results Induced by Diversity Distribution in Coupled Excitable Systems*, Phys. Rev. Lett., 105 (2010), 084101.

[41] N. G. Stocks, *Suprathreshold Stochastic Resonance in Multilevel Threshold Systems*, Phys. Rev. Lett., 84 (2000), pp. 2310–2313.

[42] H. Sakaguchi, T. Okita, *Cooperative dynamics in coupled systems of fast and slow phase oscillators*, Phys. Rev. E, 93 (2016), 022212.

[43] Y. Kawamura, H. Nakao, Y. Kuramoto, *Collective phase description of globally coupled excitable elements*, Phys. Rev. E, 84 (2011), 046211.

[44] A. K. Alijani, M. J. E. Richardson, *Rate response to neurons subject to fast or frozen noise: From stochastic and homogeneous to dynamic and heterogeneous populations*, Phys. Rev. E, 84 (2011), 011919.

[45] I. V. Tyulkina, D. S. Goldobin, L. S. Klimenko, A. Pikovsky, *Dynamics of Noisy Oscillator Populations beyond the Ott-Antonsen ansatz*, Phys. Rev. Lett., 120 (2018), 264101.

[46] J. Buceta, J. M. Parrondo, C. Van den Broeck, F. J. de la Rubia, *Negative resistance and anomalous hysteresis in a collective molecular motor*, Phys. Rev. E, 61 (2000), 6287.

[47] J. A. Bonachela, C. D. Nadell, J. B. Xavier, et al., *Universality in Bacterial Colonies*, J. Stat. Phys., 144 (2011), pp. 303–315.

[48] M. Beiran, A. Kruscha, J. Benda, B. Lindner, *Coding of time-dependent stimuli and homogeneous and heterogeneous neural populations*, J. Comp. Neurosci., 44 (2018), pp. 189–202.

[49] E. Montbrió, D. Pazó, A. Roxin, *Macroscopic description for networks of spiking neurons*, Phys. Rev. X, 5 (2015), 021028.

[50] Y. A. Kuznetsov, *Elements of Applied Bifurcation Theory*, Springer-Verlag, Berlin, Heidelberg, 1998.

[51] J. Guckenheimer, I. S. Labouriau, *Bifurcation of the Hodgkin and Huxley equations: A new twist*, Bull. Math. Biol., 55 (1993), pp. 937–952.

[52] N. Kopell, G. B. Ermentrout, *Symmetry and phaselocking in chains of weakly coupled oscillators*, Commun. Pure Appl. Math., 39 (1986), pp. 623–660.

[53] G. B. Ermentrout, *A heuristic description of spiral wave instability in discrete media*, Physica D: Nonlinear Phenomena, 82 (1995), pp. 154–164.

[54] Y. Kuramoto, D. Battogtokh, *Coexistence of coherence and incoherence in nonlocally coupled phase oscillators*, preprint arXiv:cond-mat/0210694.

[55] D. Orr, G. B. Ermentrout, *Synchronization of oscillators via active media*, Phys. Rev. E., 99 (2019), 052218.

[56] S. Coombes, Á. Byrne, *Next generation neural mass models*, Nonlinear Dyn. Comp. Neurosci., Springer, Cham, 2019, pp. 1–16.

[57] C. Bick, M. Goodfellow, C. R. Laing, E. A. Martens, *Understanding the dynamics of biological and neural oscillator networks through exact mean-field reductions: a review*, J. Math. Neurosci., 10 (2020), pp. 1–43.

[58] D. Taylor, P. Holmes, *Simple models for excitable and oscillatory neural networks*, J. Math Biol., 37 (1998), pp. 419–446.

[59] C. Zhou, J. Kurths, B. Hu, *Frequency and phase locking of noise-sustained oscillations in coupled excitable systems: Array-enhanced resonances*, Phys. Rev. E, 67 (2003), 030101.

[60] S. Tanabe, T. Shimokawa, S. Sato, K. Pakdaman, *Response of coupled noisy excitable systems to weak stimulation*, Phys. Rev. E, 60 (1999), 2182.

[61] J. A. Reinoso, M. C. Torrent, C. Masoller, *Emergence of spike correlations in periodically forced excitable systems*, Phys. Rev. E, 94 (2016), 032218.

[62] Y. Wang, Z. D. Wang, W. Wang, *Dynamical Behaviors of Periodically Forced Hindmarsh-Rose Neural Model: The Role of Excitability and 'Intrinsic' Stochastic Resonance*, J. Phys. Soc. Japan, 69 (2000), pp. 276–283.

[63] C. Zhou, J. Kurths, *Noise-sustained and controlled synchronization of stirred excitable media by external forcing*, New J. Phys., 7 (2005), 18.

[64] J. Best, A. Borisyuk, J. Rubin, D. Terman, M. Wechselberger, *The Dynamic Range of Bursting in a Model Respiratory Pacemaker Network*, SIAM J. Appl. Dyn. Syst., 4 (2005), pp. 1107–1139.

[65] R. Butera, J. Rinzel, J. Smith, *Models of respiratory rhythm generation in the pre-Botzinger complex. I. Bursting pacemaker neurons*, J. Neurophys., 82 (1999), pp. 382–397.